UNIVERSITÀ DI PARMA

UNIVERSITÀ DEGLI STUDI DI PARMA

DOTTORATO DI RICERCA IN FISICA

CICLO XXXVII

General Relativistic Resistive Magnetohydrodynamics in Neutron Stars: Development and Application of the MIR Code

Coordinatore:
Chiar.ma Prof. Raffaella Burioni

Tutore:
Chiar.mo Prof. Roberto De Pietri

Dottorando:
Kevin Franceschetti

Anni Accademici 2021/2022 - 2023/2024

Contents

List of publications

In collaboration with Florence's research group

- ❖ General Relativistic Magnetohydrodynamics Mean-Field Dynamos; Del Zanna, L., Tomei N., Franceschetti K., Bugli M., and Bucciantini N.; *Fluids* 2022, 7(2), 87
- ❖ Numerical Equilibrium Configurations and Quadrupole Moments of Post-Merger Differentially Rotating Relativistic Stars; Franceschetti K., Del Zanna L., Soldateschi J., and Bucciantini N.; *Universe* 2022, 8(3), 172

As a member of the LIGO-VIRGO-KAGRA Collaboration

- ❖ Observation of Gravitational Waves from the Coalescence of a $2.5-4.5\,M_\odot$ Compact Object and a Neutron Star; Abac, A.G., et al.; **ApJL** 2024, 970, L34
- ❖ Ultralight vector dark matter search using data from the KAGRA O3GK run; Abac, A.G., et al.; *Phys. Rev. D* 2024, 110, 042001
- ❖ Search for Eccentric Black Hole Coalescences during the Third Observing Run of LIGO and Virgo; Abac, A.G., et al.; **ApJ** 2024, 973 132

Manuscripts currently in preparation

- ❖ MIR: a general-relativistic resistive-magneto-hydrodynamic code to study the effect of resistivity in Neutron Star dynamics; Franceschetti K., De Pietri R.; in preparation

Introduction

On August 14, 2017, the Advanced Virgo detector and the two Advanced LIGO detectors coherently observed a transient gravitational-wave signal (GW170814) produced by the coalescence of two stellar mass black holes (Abbott et al. 2017a). A few days later, on August 17, 2017, a new gravitational wave (GW) signal (GW170817) was detected (Abbott et al. 2017b). GW170817 was produced by two neutron stars (NSs) spiraling closer to each other and finally merging, and it's the first GW observation confirmed by non-gravitational means. In fact, a short gamma-ray burst (GRB), designated GRB 170817A, was detected by the Fermi and INTEGRAL spacecraft beginning 1.7 seconds after the GW merger signal (Abbott et al. 2017c). This observation has set a real milestone in the history of multi-messenger astronomy. The GW spectrum, extending from attohertz to kilohertz frequencies, provides a fertile ground for exploring many fundamental questions in physics and astronomy (Bailes et al. 2021). The amplitude and frequency of the wave depend on the amount of mass that remains after the merger as well as how compact the remnant object is. For this reason, the detection of a post-merger signal could provide insight into the properties of the original system that would be difficult to explore in other ways, such as the nuclear equation of state. In fact, NSs are the smallest and densest stars in the Universe, with a radius of the order of 10 km and a mass between about 1.4 and 2.17 solar masses. Under these conditions, matter reaches densities very close to those of an atomic nucleus.

The post-merger GW emission also depends on the magnetic field strength of the remnant. Indeed, intense magnetic fields can deform the star, making it more or less oblate (Dall'Osso et al. 2009, Mastrano et al. 2013), and give observable signals of GWs. The star deformation (and thus the post-merger emission) also depends on the multipole order of the magnetic field (Mastrano et al. 2015). However, the processes that give rise to the strong magnetic fields of NSs (between 10^8 and 10^{15} times stronger than Earth's one) are a matter of controversy and many evolutionary scenarios have been proposed so far.

To study the post-merger phase of a Binary Neutron Stars (BNS) system, several

numerical codes have been developed to date, such as `GRHydro` (Mösta et al. 2013), `IllinoisGRMHD` (Etienne et al. 2015), and `Spritz` (Cipolletta et al. 2020). All of these codes work in the so-called Ideal Magnetohydrodynamical (IMHD) condition, which assumes that the fluid has so little resistivity that it can be treated as a perfect conductor. However, the combination of fast rotations and intense magnetic fields can generate anisotropies in the distribution of currents, thus dropping the IMHD regime's validity conditions. This can lead to the development of instabilities that can increase the effective resistivity of the plasma. The enhanced resistivity is usually the result of the formation of small-scale structures like current sheets or fine-scale magnetic turbulence. However, General-Relativistic-Resistive-Magneto-Hydrodynamics (GRRMHD) requires numerical methods different from those used to study the Ideal MHD regime. An optimal choice is to use the IMEX (IMplicit EXplicit) scheme, which can guarantee stability in reasonable computation times (Pareschi and Russo 2005, Palenzuela et al. 2009). To further reduce computation times, numerical simulations must be performed using parallel systems, which subdivide the numeric domain in a predetermined number of equal subdomains, each entrusted to a different processor. To evaluate the non-viscous flows, shock-capturing methods are required. These methods are a class of techniques for calculating non-viscous shock wave flows. In these methods the equations governing the evolution of flows are expressed in a conservative form and the shock waves and discontinuities are calculated as part of the solution. Modern shock capture schemes use *upwind* schemes to solve hyperbolic partial differential equations, which discretize the differential equations in the direction determined by the sign of the characteristic velocities (Londrillo and Del Zanna 2000, Del Zanna and Bucciantini 2002, Del Zanna et al. 2003).

In many numerical simulations, the spatial resolution - constrained by available computational resources - is insufficient to capture fine details or high-frequency features of the phenomenon being studied. To resolve all relevant scales, extremely fine grids would be required, leading to prohibitive computational costs. Moreover, the MHD equations are hyperbolic in nature and tend to develop discontinuities, such as shocks and tangential discontinuities. If not addressed with proper numerical methods, these features can introduce spurious oscillations, due to the Gibbs phenomenon, and numerical instabilities, thereby compromising the accuracy of the results. The absence of physical dissipation in the Ideal MHD equations allows magnetic structures to collapse into increasingly smaller scales, beyond the resolution of the numerical grid. This leads to an accumulation of kinetic and magnetic energy, a process known as the "*energy cascade towards small scales*", which inevitably causes the numerical solution to diverge. Furthermore, numerical discontinuities or shock waves can become excessively steep, resulting in unstable behavior such as spurious oscillations or non-physical solutions. To address these numerical challenges and ensure the stability of the simulations, artificial viscosity, such as the fifth-order Kreiss-Oliger dissipation (Kreiss and Oliger 1973), is added to IMHD simulations. This artificial term, which does not exist in nature,

serves the purpose of dissipating energy on the smallest scales. However, choosing the appropriate value for the artificial viscosity coefficient requires a delicate balance: an excessively high value overly smooths out physical structures, while a value that is too low fails to ensure numerical stability. Incorporating physical dissipation mechanisms, such as physical viscosity or electrical resistivity, helps to dampen small-scale discontinuities or instabilities, thereby eliminating the need for artificial dissipation. Furthermore, in nature, there are always some dissipative mechanisms (albeit very small) acting on the smallest scales. Therefore, the inclusion of physical dissipation not only aids numerically but also adds physical realism to the simulation.

Up to now, IMEX schemes have been implemented in two-dimensional codes and applied to investigate the effects of electrical resistivity in relativistic jets (Mattia et al. 2023), accretion disks (Tomei et al. 2019, Del Zanna et al. 2022), and isolated neutron stars (Franceschetti and Del Zanna 2020, Del Zanna et al. 2022) in axial symmetry, the latter specifically in the presence of the dynamo mechanism, a process through which a rotating, convecting, and electrically conducting fluid can generate a magnetic field by self-inductive action converting kinetic energy into magnetic energy (e.g., Moffatt 1983, Biskamp 1997, Brandenburg and Subramanian 2005). Notable are the works of Dionysopoulou et al. 2015 and Shibata et al. 2021, which carried out resistive simulations of neutron star mergers, the latter incorporating the dynamo term used in the previously cited two-dimensional studies. However, the codes used in those works are not publicly available; therefore, we have been unable to analyze, test, or employ them to meet our specific research objectives.

In this Ph.D. thesis, we present a new code, `MIR` (an acronym for "MagnetoIdrodinamica Resistiva", i.e., resistive magnetohydrodynamics in Italian; Franceschetti and De Pietri 2024a). Developed from scratch, `MIR` is capable of solving the equations of general relativistic resistive magnetohydrodynamics in a three-dimensional dynamical spacetime. The code can, therefore, be used to perform numerical simulations in three different regimes (Hydrodynamics, Ideal MHD, and Resistive MHD) to study the temporal evolution of astrophysical systems that require a general relativistic framework, such as accretion disks, neutron stars, and binary systems of compact objects. `MIR` will provide the community with the first publicly available code capable of performing resistive magnetohydrodynamic simulations within the EinsteinToolkit framework (Löffler et al. 2012).

This thesis is organized as follows. In the first chapter, we briefly present the astrophysical sources and their associated emissions where electrical resistivity is expected to play an important role. In the second chapter, we provide an overview of the main mechanisms proposed to explain the origin and evolution of the magnetic fields of these sources, particularly those of neutron stars, both isolated and in binary systems. In the third chapter, we review the equations of resistive magnetohydrodynamics in both the covariant approach and the 3+1 formalism, which is the most commonly used in numerical relativity. In the fourth chapter, we introduce the MIR code, describing the

numerical methods employed and their implementation. Finally, in the fifth chapter, we present the results of several numerical tests and a first study of a bar-mode instability in the resistive regime, which is useful for understanding the effects of electrical resistivity in a post-merger-like configuration and the evolution of the magnetic field during strongly dynamic evolution of the matter component.

Units and conversion factors

In this work we make use of geometrized units ($G = c = M_\odot = 1$) combined with the Lorentz–Heaviside units ($\varepsilon_0 = \mu_0 = 1$) for the electromagnetic quantities. The assumed signature for the spacetime metric tensor is $(-,+,+,+)$. Greek indices run from 0 to 3, while latin spatial indices run from 1 to 3. In addition, the Einstein summation notation is used.

The table below shows the values of the conversion parameter κ from geometrized to physical (cgs) units (i.e. $f_{cgs} = \kappa f_{geom}$ for any quantity f, where the subscript $_{cgs}$ denotes the cgs system of units while the subscript $_{geom}$ denotes the geometrized units). Recall that pressure has the dimensions of an energy density, while an electric field has the dimensions of the product of a magnetic field and velocity.

Quantity	**Physical dimensions**	$\boldsymbol{\kappa}$
Length	L	$\mathrm{G}\,\mathrm{M}_\odot\,\mathrm{c}^{-2}$
Time	T	$\mathrm{G}\,\mathrm{M}_\odot\,\mathrm{c}^{-3}$
Mass	M	$\mathrm{M}_\odot$
Velocity	$\mathrm{L}\,\mathrm{T}^{-1}$	c
Angular velocity	T^{-1}	$\mathrm{G}^{-1}\,\mathrm{M}_\odot^{-1}\,\mathrm{c}^{3}$
Energy	$\mathrm{M}\,\mathrm{L}^{2}\,\mathrm{T}^{-2}$	$\mathrm{M}_\odot\,\mathrm{c}^{2}$
Energy density	$\mathrm{M}\,\mathrm{L}^{-1}\,\mathrm{T}^{-2}$	$\mathrm{G}^{-3}\,\mathrm{M}_\odot^{-2}\,\mathrm{c}^{8}$
Density	$\mathrm{M}\,\mathrm{L}^{-3}$	$\mathrm{G}^{-3}\,\mathrm{M}_\odot^{-2}\,\mathrm{c}^{6}$
Magnetic field	$\mathrm{M}\,\mathrm{T}^{-2}\,\mathrm{I}^{-1}$	$\sqrt{4\pi}\,\mathrm{G}^{-3/2}\,\mathrm{M}_\odot^{-1}\,\mathrm{c}^{4}$

Here physical constants G, c and $M_\odot$ are in cgs units. Moreover, it results to be convenient to convert the electric field in statV/cm. This because an electric field of $1\,\mathrm{statV/cm}$ has, in a vacuum, the same electromagnetic energy density of a magnetic field of $1\,\mathrm{G}$. In this case, the conversion factor κ for the electric field is, from a numerical point of view, the same of the magnetic field.

Chapter 1

Astrophysical sources and their emissions

Modern astrophysics devotes a significant portion of its research to the analysis of phenomena associated with compact objects, such as neutron stars, black holes, and white dwarfs, which offer a unique perspective for understanding the extreme physical processes of the universe. These objects, in addition to serving as natural laboratories for studying the laws of physics under extreme conditions of density and gravity, are often linked to violent processes and highly intense energetic emissions. In particular, the presence of accretion disks and the emission of relativistic jets, as seen in the case of gamma-ray bursts, represent some of the most spectacular examples of such phenomena.

This chapter aims to explore the variety of compact astrophysical sources and their emissions, analyzing the physical processes underlying the formation and evolution of their magnetic fields, as well as the role of gravitational waves. Understanding these emissions is crucial not only for their influence on the surrounding environment, but also for the valuable insights they provide into the fundamental processes that govern the universe.

1.1 Compact objects

(Main references: Shapiro and Teukolsky 1983, Lipunov 1992, Glendenning 1997, Camenzind 2007, Ghosh 2007)

Compact objects represent a category of celestial bodies characterized by extremely high density and intense gravitational attraction concentrated within a relatively small volume. These objects are characterized by their intense gravitational force. When the degeneracy pressure of electrons or neutrons is able to balance gravity, a *degenerate star* (white dwarf or neutron star) is formed. However, if the gravitational force exceeds even these degeneracy pressures, the object collapses into a black hole.

To be considered compact, objects must posses a density greater than approximately $10^3\,\mathrm{g/cm^3}$, where electron can be treat as free particle, with the important distinction

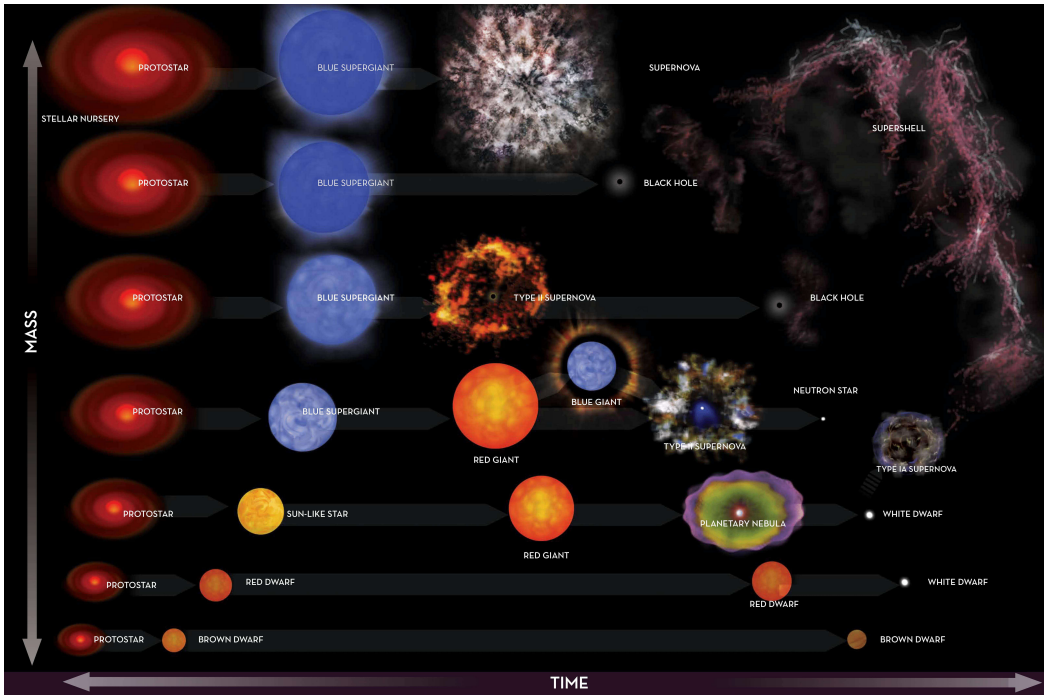

Figure 1.1: An illustration depicting potential evolutionary pathways for stars based on their initial masses (Adapted from NASA 2019).

that when the density is greater than approximately $10^6\,\mathrm{g/cm^3}$, where their energy is greater than their rest mass and indeed there is a reason of relativistic degeneracy. Above this critical density threshold, matter begins to behave in radically different ways compared to more common celestial bodies.

The formation of compact objects occurs through complex evolutionary processes, typically at the end of the life cycle of massive stars. When a star exhausts its nuclear fuel, its core can collapse under the influence of gravity, leading to the emergence of dense structures such as white dwarfs, neutron stars, or black holes. Mass and density play crucial roles in determining a star's ultimate fate; sufficiently massive objects can reach states of such high density that collapse into extremely dense forms is possible (Figure 1.1).

The investigation of these celestial bodies not only deepens our understanding of stellar evolution but also contributes to a broader understanding of the fundamental forces governing the cosmos. Compact objects, with their extreme physical conditions, provide unique opportunities to explore and test the laws of physics, pushing the boundaries of our understanding of the universe.

1.1.1 White Dwarfs

When stars with masses between approximately 0.08 and 8 solar masses exhaust their nuclear fuel and are no longer able to sustain nuclear reactions in their cores, they collapse under their own gravity, forming extremely dense objects with sizes comparable to that of Earth but with masses similar to that of the Sun, known as *white dwarfs*. Under these conditions, the electrons are compressed into a very small volume, exerting a pressure (known as *electron degeneracy pressure*) that counteracts gravity and prevents further collapse. A fundamental aspect of white dwarfs is the *Chandrasekhar limit* (Chandrasekhar 1931), which defines the maximum mass a white dwarf can possess. This limit, approximately 1.4 solar masses, indicates that if a white dwarf exceeds this mass, it will no longer be able to maintain the balance between the gravitational force and the electron degeneracy pressure. As a result, the star would undergo further collapse.

White dwarfs are characterized by a composition predominantly of carbon and oxygen, which are remnants of the nuclear fusion that occurred in the progenitor star's core. However, a thinner outer layer composed of hydrogen or helium may be present. The internal structure of a white dwarf is stratified, with a dense core of carbon and oxygen surrounded by shells of lighter elements.

Their luminosity (i.e. the total energy radiated by the star per unit time), although faint, is a result of residual heat, gradually released into the surrounding space. The luminosity of a white dwarf is described by the *Stefan-Boltzmann law*:

$$L = \sigma A T^4 \tag{1.1}$$

where L represents the luminosity of the white dwarf, expressed in erg/s, σ is the Stefan-Boltzmann constant, A indicates the surface area of the white dwarf, expressed in cm^2, T represents the effective temperature of the white dwarf, expressed in Kelvin, and corresponds to the temperature of the stellar surface. This formula implies that a small increase in temperature results in a significant increase in luminosity. Therefore, hotter white dwarfs are also more luminous. The luminosity-temperature relationship has made white dwarfs indispensable tools for determining cosmic distances. By measuring the temperature of a white dwarf and knowing its surface area (which can be estimated based on its mass), it is possible to calculate its intrinsic luminosity. By comparing this luminosity with the apparent luminosity, i.e. that measured from Earth, one can determine the distance at which the white dwarf is located.

However, it is important to emphasize that the Stefan-Boltzmann law represents a simplification. However, it is important to emphasize that the Stefan-Boltzmann law represents a simplification. The luminosity of a white dwarf also depends on other factors, such as the chemical composition of its atmosphere, the presence of magnetic fields, and its age. More sophisticated astrophysical models are required to accurately describe the thermal evolution and luminosity of these objects. Despite these complexities, the study of the luminosity-temperature relationship of white dwarfs remains an

active field of research, with significant implications for understanding stellar evolution and the structure of the universe. In fact, white dwarfs are true "stellar fossils", allowing us to study the properties of intermediate-mass stars and obtain information about the history of the universe.

Over time, white dwarfs gradually cool down as they no longer produce energy through nuclear fusion. During this cooling process, the outer layers of the white dwarf can undergo gravitational settling. In this process, lighter elements such as hydrogen and helium tend to rise to the surface, while heavier elements like carbon and oxygen remain confined in the core. Despite the gradual cooling, the core maintains its structural stability due to electron degeneracy pressure. However, cooling leads to a progressive crystallization of the core, a process in which the material inside the white dwarf transitions from an ionized plasma state to a solid phase, similar to the formation of a giant carbon-oxygen crystal (Tremblay et al. 2019). This crystallization phenomenon further slows down the cooling process. Over time, the white dwarf becomes less luminous as it emits its last reserves of thermal energy in the form of radiation. Over an extremely long timescale, the white dwarf could theoretically become a *black dwarf*, a completely cold and dark celestial body. However, since the age of the universe is not yet sufficient, no white dwarf has had enough time to reach this final stage.

White dwarfs can also possess significant magnetic fields, generated during the formation process. Some examples of white dwarfs exhibit magnetic fields that can range from a few kilogauss to millions of gauss. These magnetic fields can influence their evolution and interact with the surrounding environment, particularly when white dwarfs are part of binary systems. The interaction between a white dwarf and a companion star can generate complex magnetic phenomena and even contribute to supernova explosions.[1]

[1] A *supernova* is a catastrophic event that marks the death of a star, characterized by a sudden and violent explosion that can outshine an entire galaxy for a brief period. Supernovae are fundamental in astrophysics, as they not only signify the end of a star's life, but also contribute to the creation and dispersal of heavy elements in the universe, thereby influencing the formation of new stars and planets.

There are primarily two types of supernovae, classified according to their light curves and the absorption lines of different chemical elements that appear in their spectra. If the spectrum contains lines of hydrogen, the supernova is classified *Type II*; otherwise it is *Type I*. In particular, *Type Ia supernovae* occur in binary star systems, where a white dwarf accretes material from a companion star. When the mass of the white dwarf exceeds the Chandrasekhar limit, the electron degeneracy pressure is no longer sufficient to counteract gravitational forces. This leads to a rapid collapse, followed by a thermonuclear explosion that completely destroys the white dwarf. *Type Ia supernovae* are particularly important as cosmic indicators, since their peak brightness is fairly uniform, allowing astronomers to calculate cosmic distances. On the other hand, *Type Ib/c* and *Type II supernovae* occur when massive stars (with masses greater than about eight solar masses) exhaust their nuclear fuel. In this case, the star's core collapses under its own gravity, causing a sudden explosion. *Type II supernovae* are characterized by the

A significant fraction of white dwarfs is indeed found in binary or multiple systems (e.g., Holberg 2009, Toonen et al. 2017). In these cases, interactions with companion stars can have important effects on their evolution. When a white dwarf is in a binary system, it may accrete material from the companion star, which can lead to dramatic events such as novae or, in extreme cases, Type Ia supernovae, when the white dwarf exceeds the Chandrasekhar limit.

1.1.2 Neutron stars

When a massive star, with an initial mass between 8 and 25 solar masses, exhausts its nuclear fuel, the core collapses under its own gravity. This contraction generates extreme temperatures and pressures, triggering a series of nuclear reactions that lead to a supernova explosion, expelling the outer layers of the star and leaving behind a compact core. During the collapse, the electrons (e^-) and protons (p) present in the star's atoms combine, converting protons into neutrons (n) and simultaneously resulting in the emission of an electron neutrino (ν_e) through electron capture:

$$p + e^- \rightarrow n + \nu_e \tag{1.2}$$

For this reason, this object is known as a *neutron star*.

The hallmark of a neutron star is its extreme density: a neutron star can have a mass equal to that of the Sun but compressed into a diameter of only 20-30 kilometers. This means that a single teaspoon of neutron star material would weigh billions of tons on Earth. Another remarkable characteristic of neutron stars is their intense gravitational field, which is about 2 billion times stronger than that of Earth. This means that, if one were to stand on a neutron star, any object would fall to the surface in a fraction of a second at speeds approaching the speed of light. The gravitational field is so powerful that it distorts spacetime around the star, causing gravitational lensing effects.

As with white dwarfs, it is possible to determine the Chandrasekhar limit for neutron stars, which is approximately four times that of white dwarfs. However, this limit was originally derived using the Lane-Emden theory, which describes the hydrostatic equilibrium of a self-gravitating polytropic fluid with spherical symmetry and no rotation, without accounting for general relativity. Incorporating general relativity, one arrives at the *Tolman-Oppenheimer-Volkoff* (TOV) *limit* for a cold, non-rotating star, which is approximately 0.7 solar masses. Considering the strong nuclear repulsive forces between neutrons, modern works yield significantly higher estimates, ranging from 1.5 to 3 solar masses. Observations of GW170817 (Abbott et al. 2017b), the first gravitational wave event detected from the merger of two neutron stars, suggest that this limit is close to 2.17 solar masses (Margalit and Metzger 2017).

presence of hydrogen in their spectra, indicating that the star had an outer layer of hydrogen prior to the explosion. During this event, enormous amounts of energy are released, and the expelled materials enrich the universe with heavy elements.

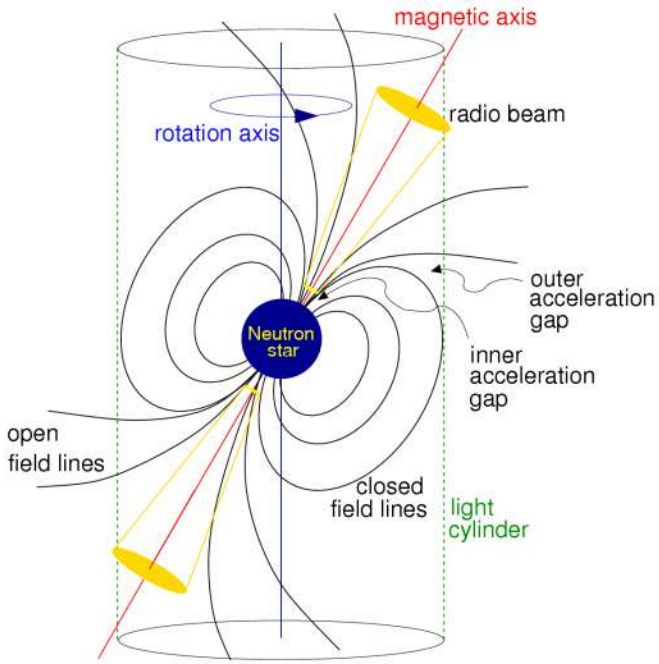

Figure 1.2: Toy model for the rotating neutron star and its magnetosphere (not drown in scale). The *light cylinder* is an imaginary surface centered on the star and aligned with the rotation axis at whose radius the co-rotating speed of the magnetic field lines equals the speed of light. The *closed field lines* are the magnetic field lines closed inside the light cylinder, while the *open field lines*, which are centered on the magnetic axis, are those which would close outside the light cylinder but cannot since plasma would exceed the speed of light. *Acceleration gaps* are the two main regions from which the pulsar high-energy radiation should come. The *inner* (or *polar*) *gap* region is located in the open field line region above the magnetic polar cup, while the *outer gap* is located between the outer and the inner field lines close to the light cylinder. (Lorimer and Kramer 2005).

The theoretical existence of neutron stars was proposed by Baade and Zwicky 1934, which came shortly after Sir James Chadwick's discovery of the neutron, just under two years prior (Chadwick 1932). In their research on supernovae, Baade and Zwicky hypothesized that neutron stars are formed from the explosive remnants of massive stars with masses exceeding 6 to 8 times that of the Sun.

The first neutron star was identified in 1967 by Jocelyn Bell Burnell and Antony Hewish, who detected regular radio pulses of 1.337 seconds from the pulsar known as PSR B1919+21.

1.1.2.1 Pulsars and magnetars

A pulsar (from "**puls**ating st**ar**", Figure 1.2) is a particular class of neutron star that emits narrow, regular beams of electromagnetic radiation from its magnetic poles. These beams are observable only if they are directed toward Earth, and as the star rotates, the beams appear to switch on and off, resembling the behavior of a lighthouse. This periodic emission generates regular radio signals, which is the origin of the pulsar's name.

One of the most distinctive features of pulsars is the remarkable regularity of their pulses. Some are so precise that they are considered among the most reliable natural clocks in the universe. This precision has led to pulsars being used in various scientific contexts, including the study of gravitational waves and the measurement of subtle variations in spacetime. Some pulsars, known as *millisecond pulsars*, rotate at extraordinarily high speeds, completing hundreds of rotations per second. Their rapid rotation is often enhanced by the transfer of matter from a companion star in a binary system.

Canonical pulsars have periods ranging from $P \sim 0.003\,\mathrm{s}$ to a few seconds and exhibit dipole magnetic fields of $\approx 10^{10} - 10^{14}\,\mathrm{G}$. Millisecond pulsars, on the other hand, are characterized by very short periods $P \lesssim 10\,\mathrm{ms}$, and weak dipole magnetic fields $B \lesssim 10^{10}\,\mathrm{G}$. Such rapid rotations deform the star, leading to the emission of gravitational waves and deviations from the mass-radius relationship predicted for non-rotating stars. In particular, rotation increases the maximum mass of the star by $10 - 20\%$, expands the equatorial radius by $15 - 20\%$, and reduces the central density by approximately 20%.

Pulsars occasionally experience *glitches*, during which the star abruptly accelerates its rotation due to internal adjustments. The star then gradually returns to its original spin rate over a period of days to weeks. Glitches can excite oscillations within the star, which in turn may produce burst-like emissions of gravitational waves.

Pulsars can also experience *pulse nulling*, a sudden cessation of their regular radio emissions that can last for up to $\sim 10^4\,\mathrm{s}$. An extreme form of nulling is observed in *Rotating Radio Transients* (RRATs), a distinct class of pulsars where no pulsed emission is detected between individual, sporadic radio bursts.

If a neutron star possesses a magnetic field on the order of $10^{14} - 10^{15}\,\mathrm{G}$ - among the strongest known in the universe - it is classified as a *magnetar* (from "**magnet**ic st**ar**"). Magnetars typically rotate more slowly than regular pulsars, with rotation periods in the range $\sim 2 - 12\,\mathrm{s}$, and their characteristic spin-down ages are on the order of $10^{14}\,\mathrm{yr}$.

Magnetars are known for their extreme instability. Due to their tremendously powerful magnetic field - which completely governs the star's behavior, influencing not only radiation emission but also its internal structure and long-term evolution, and whose origin is still a matter of controversy (see Chapter 2) - the star's crust can undergo violent "starquakes" and other instabilities that release vast amounts of energy over short periods. These events lead to magnetic flares, explosive outbursts that can release, in

just a few seconds, as much energy as the Sun emits over tens of thousands of years.

The magnetar class encompasses two distinct types of neutron stars, characterized by persistent X-ray emissions with luminosities in the range of $L_X \sim 10^{33} - 10^{36}\,\mathrm{erg/s}$: *Soft Gamma Repeaters* (SGRs) and *Anomalous X-ray Pulsars* (AXPs). SGRs are known for their violent outbursts, called giant flares, during which they release an immense amount of energy, approximately $10^{44} - 10^{46}\,\mathrm{erg}$, in less than one second. AXPs, on the other hand, exhibit modulation in their X-ray emissions, with a significant pulsed fraction.

If an event such as a starquake or a rotational instability were to cause an asymmetric deformation in the shape of a magnetar, it could potentially release gravitational waves. Although direct detection of gravitational waves from magnetars has not yet occurred, these extreme stars are considered promising sources for future gravitational wave detectors like LIGO (Aasi et al. 2015) and Virgo (Acernese et al. 2015).

1.1.2.2 Internal structure

The internal structure of neutron stars is characterized by extreme physical conditions and extraordinarily high densities, reaching up to approximately $4 \times 10^{14}\,\mathrm{kg/m^3}$. Today, neutron stars come in various flavors depending on the composition of the *core*, where all atomic nuclei have been dissolved into their fundamental constituents: neutrons and protons. Migdal, in 1959, pointed out that the neutron liquid within a neutron star must necessarily be in a superfluid state (Migdal 1959). This state of matter exhibits a division into bound pairs, analogous to Cooper pairs in a superconductor. Ginzburg and Kirzhnits, in 1964, observed that vortices must exist in the superfluid components of a rotating neutron star (Ginzburg and Kirzhnits 1964).

Within the core of a neutron star, the density is so high that it allows for the emergence of heavier particles, such as hyperons and baryon resonances (Σ, Λ, Ξ, Ω). Under these conditions, the core may also contain a gas of free quarks, including up, down, and strange quarks, potentially in a state of color superconductivity. In this context, we distinguish traditional neutron stars, or *hadronic stars*, where the core is predominantly composed of neutrons, protons, and electrons, from *hyperon stars*, in which, at high densities, heavier baryons are excited. Figure 1.3 illustrates the theoretical predictions regarding the compositions of neutron stars. The notations 2SC and CFL refer to color-superconducting quark condensates, which represent specific states of matter within these stars at extremely high densities.

Given that the density within a neutron star reaches nuclear densities, it is natural to compare such matter with nuclear matter. Although both forms of matter are composed of baryons, the similarities and differences between nuclear matter and that of neutron stars are significant and profoundly influence the properties of these cosmic objects.

The similarities primarily lie in the fact that both forms of matter are composed of nucleons, namely protons and neutrons, and their densities are comparable. However, differences arise from two fundamental aspects. Firstly, both atomic nuclei and neutron

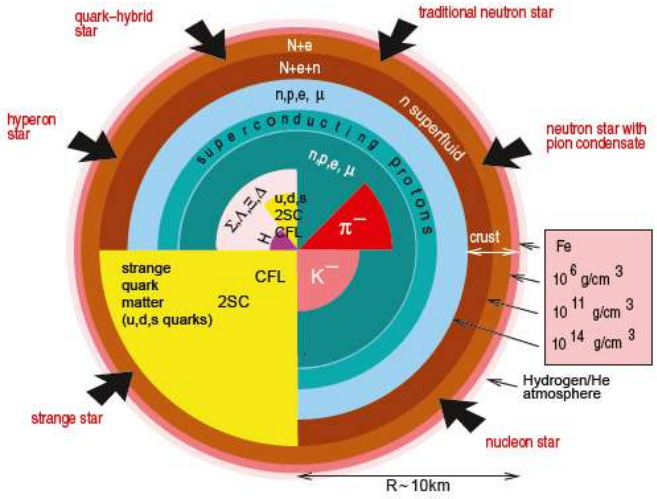

Figure 1.3: Neutron star compositions predicted by theory. (Weber et al. 2009).

stars are bound systems, but they are held together by different forces. Atomic nuclei are bound by the strong nuclear force, whereas neutron stars are stabilized by gravitational forces. In nuclear matter, the number of neutrons (N) tends to be similar to the number of protons (Z); however, in a neutron star, the net charge is essentially zero, since the repulsive Coulomb force is significantly stronger than the gravitational force. Notably, in a neutron star, the net charge satisfies the relationship

$$Z_{net} < 10^{-36} A \tag{1.3}$$

where Z_{net} is the net charge of the star and A is the atomic mass number.

The second profound difference concerns the strangeness of the particles. Matter in atomic nuclei has a zero net strangeness, whereas neutron stars can contain hyperons, resulting in a non-zero net strangeness. Due to the high density of matter within neutron stars and the Pauli exclusion principle governing the behavior of baryons, it becomes energetically favorable for nucleons at the top of the Fermi sea to convert into other baryons, including strange ones, such as hyperons, in order to lower the Fermi energy.

When we refer to "neutron star matter", we mean a cold nuclear matter that is electrically neutral, in its lowest energy state, and generally in beta equilibrium, defined as *cold-catalyzed matter*.

Further information can be found in Glendenning 1997 and Weber et al. 2009.

1.1.3 Black Holes

A star with an initial mass exceeding 25 solar masses undergoes gravitational collapse at the end of its life cycle. The resulting compact object, known as a *black hole*,

possesses a gravitational field so intense that its escape velocity exceeds the speed of light.

A black hole is commonly defined by its event horizon, the boundary beyond which nothing can escape. This horizon is not a physical surface, but rather a threshold marking the point of no return. Objects approaching this limit are irresistibly drawn in and, as they near the horizon, may emit radiation, particularly X-rays, due to the compression and heating of the surrounding material.

The geometry of spacetime surrounding a black hole undergoes a dramatic transformation as an object is drawn toward it. This results in remarkable phenomena such as gravitational time dilation. Distant observers perceive time as passing more slowly for an object approaching a black hole, an effect with profound implications for our understanding of the very nature of time.

Black holes can be classified primarily by their mass. *Stellar black holes*, with masses ranging from 3 to several tens of solar masses, are the most common. *Supermassive black holes*, which can have masses equivalent to millions or even billions of solar masses, are found at the centers of most galaxies, including the Milky Way. Their formation and role in galactic evolution are subjects of intense research. Finally, there are *intermediate-mass black holes*, which fall within a mass range between stellar and supermassive black holes, but their existence and formation remain poorly understood.

Black holes are not merely isolated objects; they play a crucial role in the dynamics of galaxies and the evolution of the universe. Supermassive black holes are thought to influence star formation and the distribution of matter within galaxies. Their presence can also shape the evolution of galaxies themselves, making their understanding essential to cosmology.

Black holes have been the subject of numerous theoretical and observational experiments. In 2019, the Event Horizon Telescope collaboration obtained the first image of a supermassive black hole located at the center of the galaxy M87, providing visual evidence of their existence and corroborating the predictions of general relativity (Akiyama et al. 2019). This image has opened new avenues for the study of black holes and for understanding the dynamics of astrophysical systems. Additionally, projects such as the Laser Interferometer Gravitational-Wave Observatory (LIGO) have opened a new window on the universe, allowing scientists to detect gravitational waves generated by the merger of black holes. These waves provide valuable information about the mass and spin of interacting black hole pairs, thereby contributing to our understanding of their formation and evolution.

Black holes have stimulated philosophical and theoretical discussions, particularly regarding the nature of information. The black hole information paradox, for example, raises questions about what happens to the information that enters a black hole. According to quantum theory, information cannot be destroyed, but it seems that a black hole destroys it. This apparent contradiction has led to new theories, such as Maldacena's conjecture, which seeks to reconcile general relativity and quantum mechanics

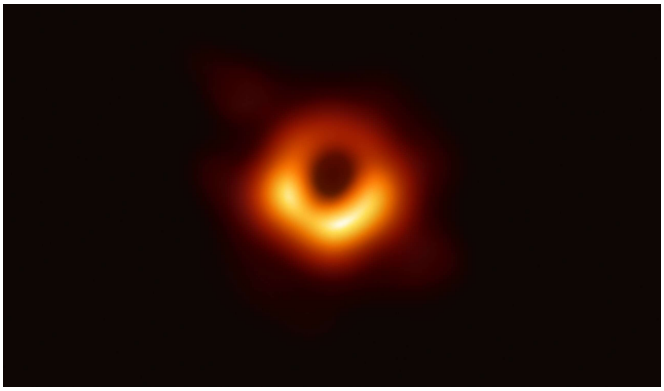

Figure 1.4: Event horizon of the supermassive black hole at the center of Messier 87. (Wikipedia (https://en.wikipedia.org/wiki/Black_hole) and Akiyama et al. 2019).

(Maldacena 1998).

1.1.3.1 Classification of Black Holes

Black holes can be categorized into three primary classes based on their physical characteristics and solutions to the Einstein field equations. These classes are: Schwarzschild black holes, Kerr black holes, and Reissner-Nordström black holes.

Schwarzschild black holes are non-rotating, uncharged black holes. Their solution represents the simplest case of a black hole, where the mass is concentrated at a point, and the event horizon is spherical. Schwarzschild black holes are described by the Schwarzschild metric and are characterized by a single event horizon located at

$$r_S = \frac{2GM}{c^2} \tag{1.4}$$

where G is the gravitational constant, c is the speed of light, and M is the mass of the black hole.

Kerr black holes, endowed with angular momentum, exhibit a more intricate spacetime geometry compared to their non-rotating counterparts. The Kerr metric, which accounts for rotation, reveals two important surfaces: an outer horizon at

$$r_H = \frac{r_S + \sqrt{r_S^2 - 4\alpha^2}}{2} \tag{1.5}$$

and an inner horizon at

$$r_E = \frac{r_S + \sqrt{r_S^2 - 4\alpha^2 \cos^2\theta}}{2} \tag{1.6}$$

where J denotes the black hole's angular momentum, θ the polar angle, and

$$\alpha = \frac{J}{Mc} \tag{1.7}$$

The region enclosed by the two radii is known as the *ergosphere*. Within this region, particles are compelled to co-rotate with the inner mass. These black holes are considered to be more realistic models of the black holes observed in the universe.

Reissner-Nordström black holes are electrically charged and can be regarded as a generalization of the Schwarzschild solution to include an electric charge. Reissner-Nordström black holes also possess an event horizon, but their structure additionally includes an inner horizon.

In addition to these three main classes, there are also other more complex solutions, such as Kerr-Newman black holes, which combine rotation and electric charge.

Electrically charged black holes were introduced to explore the theoretical implications of general relativity in the presence of electric fields. However, to date, astronomical observations and gravitational wave measurements have led to the conclusion that black holes are predominantly considered uncharged.

1.2 Accretion disks

(Main references: Frank et al. 2002, Carroll and Ostlie 2017)

Accretion disks are lenticular structures that form around a source of gravitational field. They arise when material, such as gas, dust, and plasma, is attracted toward this central object due to its gravitational pull. However, because of the angular momentum of the material, it does not fall directly onto the object but instead begins to spiral around it, forming a flattened disk.

These disks are crucial for understanding the process of "accretion", the phenomenon through which material gradually falls towards the central object. As this occurs, the gas and dust within the disk progressively lose energy and angular momentum, leading to a gradual inward movement. As the material approaches the central object, collisions between particles cause the disk to heat up. The temperature of the disk rises as it nears the central object, converting gravitational energy into thermal energy, which is then radiated and can be observed across various wavelengths, such as X-rays or ultraviolet radiation.

An extreme example of an accretion disk is found around black holes. Here, material can reach extremely high speeds and temperatures as it approaches the event horizon, resulting in the production of intense X-ray emissions. These X-rays are one of the primary observable signatures of black holes with active accretion disks. In cases where the black hole is supermassive, such as those found at the centers of galaxies, and is attracting large amounts of matter, a phenomenon known as a quasar is created. *Quasars* are among the most luminous objects in the universe, powered by accretion disks that emit extraordinary amounts of energy.

Neutron stars and white dwarfs can also host accretion disks, with similar characteristics, although the radiation emitted differs due to the differences in mass and the physical conditions of the surrounding region. Moreover, accretion disks are not lim-

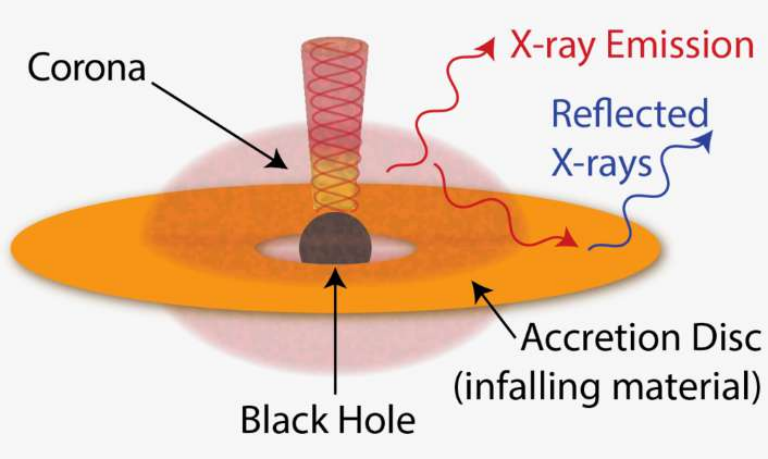

Figure 1.5: Schematic of the innermost regions around the supermassive black hole in an AGN. (Credit: D. Wilkins (https://danwilkins.net/research)).

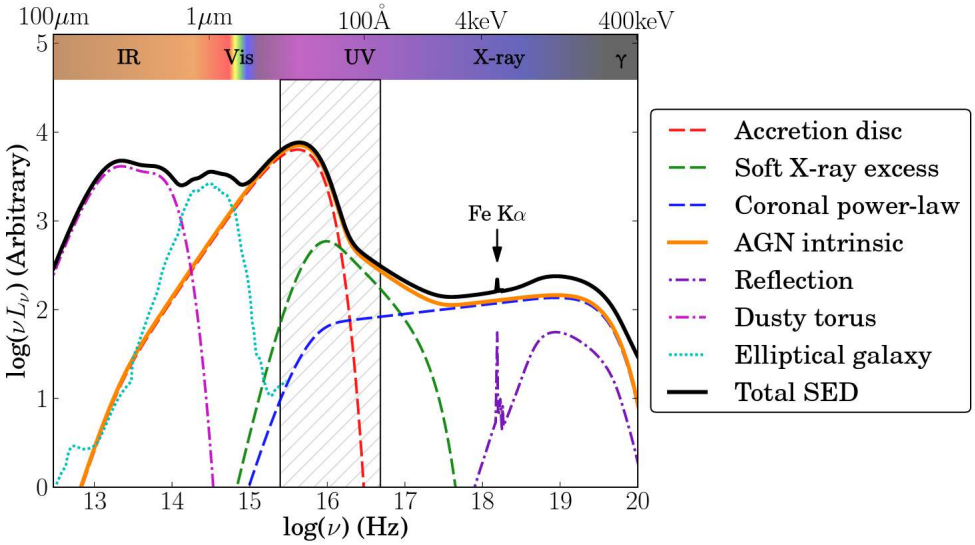

Figure 1.6: Simplified schematic diagram of an AGN SED (Collinson et al. 2016).

ited to compact and extremely massive objects: protostars, or newly formed stars, can also have disks of gas and dust that fuel their growth, contributing to the formation of planets and solar systems.

1.2.1 Active Galactic Nuclei

An Active Galactic Nucleus (AGN) can be defined as a nucleus that produces a significant amount of non-stellar energy, with a spectral distribution ranging from radio to X-ray and gamma-ray wavelengths.

In the spectrum of AGNs, an X-ray component is observed, which can only be explained through Inverse Compton scattering[2] of photons emitted by the disk by randomly distributed hot electrons forming what is known as the "*corona*" (Figure 1.5). The cooling due to Inverse Compton scattering occurs extremely quickly, indicating that there must be some mechanism by which the disk supplies energy to the corona. The exact nature of this mechanism is still unknown; one hypothesis suggests that there may be a magnetic connection between the disk and the corona.

Observing the *Spectral Energy Distribution* (SED) of AGN (Figure 1.6), it is evident that these objects exhibit a peak in emission in the ultraviolet (UV) range at an energy approximately equal to that of hydrogen ionization. A closer examination of the spectrum reveals the presence of several emission lines, which vary in width and require a strong continuous source of UV radiation.

Upon closer examination of the X-ray spectrum of an AGN, several emission lines can be observed. Among these, the most prominent is the Kα line of iron at approximately 6.4 keV, which arises from fluorescence emission in the inner region of the disk. The profile of this line allows for the determination of both the Doppler effect and gravitational redshift.

1.3 Gamma-Ray Bursts

(Main references: Meszaros 1992, Carroll and Ostlie 2017)

Gamma-ray bursts (GRBs) are brief and intense flashes of gamma radiation, lasting from a few milliseconds to several minutes. These explosions are highly directional, with energy emitted along narrow cones or jets rather than uniformly in all directions.

There are two primary categories of GRBs based on their duration. *Long GRBs*, lasting more than two seconds, are associated with the explosive death of massive stars when their core collapses into a black hole or neutron star. During the process, a relativistic jet is formed, traveling at nearly the speed of light and emitting intense radiation, which is observed as a GRB. *Short GRBs*, on the other hand, last less than two seconds and are linked to the merger of two compact objects, such as neutron stars or a black hole and a neutron star.

[2] The *inverse Compton scattering* is a physical phenomenon in which a low-energy photon interacts with a high-energy electron, resulting in a transfer of energy from the photon to the electron. Unlike the *direct Compton scattering*, where the photon loses energy and increases its wavelength, in this process, the photon gains energy and shifts to shorter wavelengths, becoming a high-energy photon, such as X-rays or gamma rays.

An indirect but significant role in the processes leading to GRB emission is played by the plasma's electrical resistivity, which measures the plasma's ability to oppose the flow of electric currents. n a plasma with non-zero resistivity, *magnetic reconnection* can occur. This is a process in which opposing magnetic field lines break and reconnect in a different configuration, releasing large amounts of energy suddenly and violently. Magnetic reconnection has been proposed as one of the key mechanisms for accelerating particles and producing the highly energetic gamma-ray emission observed in GRBs (Drenkhahn and Spruit 2002, Zhang and Yan 2011).

In the relativistic jets expelled during a GRB, the plasma's resistivity can affect the efficiency with which magnetic energy is converted into the energy of charged particles, which in turn generate electromagnetic radiation, including gamma rays. If the plasma were perfectly conductive (i.e., with zero resistivity), magnetic reconnection would not occur or would be much less efficient. However, in the presence of some resistivity, reconnection can rapidly release energy, contributing to the acceleration of particles to relativistic speeds and the collimation of the jets.

Additionally, plasma resistivity may also play a role in the Kelvin-Helmholtz instability (Section 2.4), which occurs when the plasma within the jet interacts with the surrounding material. This type of instability can promote turbulence and contribute to energy dissipation, thereby affecting the final gamma-ray emission (Lazarian and Vishniac 1999).

1.4 Gravitational waves

(Main references: Prix 2009, Maggiore 2007, Maggiore 2018)

Gravitational waves (GWs) are perturbations of spacetime caused by cataclysmic cosmic events, such as the coalescence of black holes or neutron stars. Propagating at the speed of light, these waves traverse the cosmos undeterred by intervening matter or energy. Their detection was achieved for the first time in 2015 by the LIGO and Virgo collaborations (Abbott et al. 2016), confirming a century-old prediction of Einstein's general theory of relativity.

Their detection heralds a new era in astronomy, providing a novel window into the universe and enabling the observation of phenomena otherwise invisible through traditional electromagnetic means. These signals provide fundamental insights into the nature of gravity, the structure of spacetime, and extremely compact objects such as black holes and neutron stars. Furthermore, gravitational waves allow for the exploration of distant cosmological events, such as the Big Bang and the early universe, while also confirming key aspects of general relativity and demonstrating that they carry energy through space in the form of gravitational radiation.

While the merger of compact objects is among the most powerful and easily detectable sources of gravitational waves, these waves are not exclusively emitted during such events. In fact, any accelerating mass can generate gravitational waves, at least in

theory. However, the intensity and strength of these waves are strongly influenced by the mass of the object and the speed of its acceleration. For detection, it is essential that the object involved possesses a significant mass and undergoes high accelerations.

Gravitational wave emission from isolated objects requires an asymmetry in their motion. Perfectly symmetric objects, such as a uniformly rotating sphere, do not emit gravitational waves. However, objects with deviations from spherical symmetry can produce gravitational waves, particularly when they are rapidly rotating. The deformation of these objects and their rotational motion provide the necessary conditions for gravitational wave emission. It is believed that certain neutron stars, characterized by structural irregularities, are sources of continuous gravitational waves due to their rapid rotation and surface deformations.

At frequencies lower than the Keplerian limit, instabilities driven by gravitational radiation can arise, limiting the rotation of stars. These instabilities, moderated by the star's viscosity, are both caused by and contribute to the emission of gravitational waves. Given the temperature dependence of stellar viscosity, neutron stars born with high initial rotation rates near the Keplerian limit are likely to experience a rapid spin-down due to these instabilities. The resulting gravitational waves, though weak, provide a valuable probe into the internal structure and evolution of these compact objects. The asymmetry in the mass distribution and the rapid rotation of neutron stars create the necessary conditions for the generation of continuous gravitational wave signals, offering unique insights into the physics of ultra-dense matter.

Like most objects, stars exhibit normal modes of vibration. In non-rotating stars, viscosity effectively suppresses all vibrational modes. However, in rotating stars, certain modes can become unstable, even in the presence of viscosity. These unstable modes are particularly prone to excitation at higher rotation frequencies. Such instabilities can lead to non-axisymmetric deformations, resulting in the emission of gravitational waves. The energy carried away by these waves feeds back into the instability, causing the star to spin down more rapidly. The interplay between centrifugal and tidal forces plays a crucial role in triggering and sustaining these instabilities, which can be further influenced by the viscosity of the stellar material.

Objects that approach a black hole, without necessarily merging with it, can also emit gravitational waves, such as an object orbiting a supermassive black hole. However, the most intense gravitational waves are usually generated by binary systems, such as merging black holes or neutron stars. Although, in theory, any object undergoing accelerated motion emits gravitational waves, in the case of relatively small mass objects, such as planets and normal stars, the produced waves are so weak as to be virtually undetectable. Only events involving enormous masses and high accelerations, like mergers of compact objects or the rotations of deformed neutron stars, generate waves sufficiently powerful to be detected with current technologies.

1.4.1 The geometric approach

Gravitational waves are purely transverse waves, characterized by two polarization states, denoted as "+" and "×", which differ by a 45° rotation around the propagation axis, reflecting the quadrupolar nature of the gravitational field.

A linearized form of general relativity is often used to describe gravitational waves in terms of a small perturbation to the spacetime metric, $h_{\mu\nu}$. In this framework, the metric tensor is written as

$$g_{\mu\nu} = \eta_{\mu\nu} + h_{\mu\nu} \tag{1.8}$$

where $\eta_{\mu\nu}$ is the Minkowski metric of flat, unperturbed spacetime, and $|h_{\mu\nu}| \ll 1$ represents the gravitational wave perturbation. In vacuum, the Einstein field equations are reduced to

$$\Box h^{\mathrm{TT}}_{\mu\nu} = 0 \tag{1.9}$$

a wave equation for $h_{\mu\nu}$ propagating through flat spacetime. Here[3]

$$\Box = -\partial_t^2 + \boldsymbol{\nabla}^2 \tag{1.10}$$

is the *d'Alembert operator*, and $h^{\mathrm{TT}}_{\mu\nu}$ refers to the perturbation expressed in the *transverse-traceless* (TT) *gauge*, a choice of coordinates that ensures the perturbation is *transverse* (orthogonal to the propagation direction) and *traceless* (does not compress or expand spacetime).

In the TT gauge, a plane gravitational wave propagating along the z-axis can be written as[4]

$$h^{\mathrm{TT}}_{\mu\nu}(t,z) = h^{\mathrm{TT}}_{\mu\nu}(t-z) = \begin{pmatrix} 0 & 0 & 0 & 0 \\ 0 & h_+ & h_\times & 0 \\ 0 & h_\times & -h_+ & 0 \\ 0 & 0 & 0 & 0 \end{pmatrix} \tag{1.11}$$

where $h_{+,\times}(t-z)$ are the two polarizations of the wave.

The emission of gravitational waves is well-described by the quadrupole formula[5]

$$h^{\mathrm{TT}}_{ij} = \frac{2}{r}\ddot{Q}^{\mathrm{TT}}_{ij}(t-r) \tag{1.12}$$

[3]We remind the reader that in this work, we are using the signature $(-,+,+,+)$ for the metric tensor, and we have set $c = 1$. In physical units, we would have had

$$\Box = -\big(1/c^2\big)\partial_t^2 + \boldsymbol{\nabla}^2$$

[4]We remind the reader that in this work, we have set $c = 1$. In physical units we would have had $h^{\mathrm{TT}}_{\mu\nu}(t,z) = h^{\mathrm{TT}}_{\mu\nu}(t - z/c)$.

[5]We remind the reader that in this work, we have set $c = G = 1$. In physical units we would have had

$$h^{\mathrm{TT}}_{ij} = \frac{2}{r}\frac{G}{c^4}\ddot{Q}^{\mathrm{TT}}_{ij}(t - r/c)$$

where r is the distance to the source, accounting for the time delay, and the dots denote time derivatives. The tensor $\ddot{Q}_{ij}$ represents the mass-quadrupole moment of the source, which for sources with weak internal gravity can be expressed as

$$Q_{ij} = \int \rho(t, \mathbf{x}) \left(x_i x_j - \frac{r^2}{3} \delta_{ij} \right) \mathrm{d}^3 x \tag{1.13}$$

where $\rho(t, \mathbf{x})$ is the mass density.

The energy emission rate (or, in notation commonly used in astrophysics, the total gravitational luminosity of the source) L_{GW} in gravitational waves can be expressed in the quadrupole formalism as[6]

$$L_{GW} = \frac{1}{5} \left\langle \dddot{Q}_{ij} \dddot{Q}^{ij} \right\rangle \tag{1.14}$$

where $\dddot{Q}_{ij}$ must be evaluated at the retarded time $t - r$, and $\langle \ldots \rangle$ denotes the time average over several characteristic periods of the gravitational wave. This equation highlights that the gravitational luminosity is dependent on the dynamics of the mass distribution, specifically how it changes over time. Thus, sources with significant variations in their mass quadrupole moment will emit gravitational waves more effectively, resulting in a higher total gravitational luminosity.

1.4.2 Continuous gravitational waves from neutron stars

Continuous gravitational waves are long-lasting, quasi-monochromatic signals characterized by slowly varying intrinsic frequencies. Three primary mechanisms are typically considered for the emission of continuous GWs from spinning neutron stars within the frequency range of current ground-based detectors (approximately 20 Hz to 2 kHz).

The first mechanism involves *non-axisymmetric distortions* on the neutron star's surface. Such distortions, often referred to as "mountains", cannot exist in idealized perfect fluid stars. However, in realistic neutron stars, these deformations can be supported by either elastic stresses in the crust or by magnetic fields. The degree of deformation is commonly quantified by the equatorial ellipticity

$$\varepsilon = \frac{I_{xx} - I_{yy}}{I_{zz}} \tag{1.15}$$

where I_{jj} are the three principal moments of inertia of the star. A spinning, non-axisymmetric neutron star located at a distance d and rotating with a frequency ν

[6] We remind the reader that in this work we have set $c = G = 1$. In physical units we would have had

$$L_{GW} = \frac{G}{5c^5} \left\langle \dddot{Q}_{ij} \dddot{Q}^{ij} \right\rangle$$

and the delayed time would correspondingly be $t - r/c$.

around the I_{zz} axis emits monochromatic GWs at a frequency $f = 2\nu$ with an amplitude given by

$$h_0 = \frac{16\pi^2 I_{zz}\nu^2}{d}\varepsilon \tag{1.16}$$

The relevant question is what actual deformations are likely to exist in real neutron stars. For example, a strong dipolar magnetic field that is misaligned with the rotation axis could lead to deformations of up to $\varepsilon \lesssim 10^{-6}$ in the case of a type-I superconducting[7] core. These non-aligned deformations would typically result in gravitational wave emission at both the first and second harmonics of the rotation rate, i.e., $f = \nu$ and $f = 2\nu$. Another possibility is that the differential rotation present after the formation of a neutron star could "wind up" large toroidal magnetic fields. Dissipation would then drive the symmetry axis of a toroidal field toward the star's equator, resulting in ellipticities on the order of $\varepsilon \sim 10^{-6}$ for toroidal magnetic fields of approximately $B_{tor} \sim 10^{-6}$.

The second mechanism for the emission of continuous gravitational waves from spinning neutron stars involves *non-axisymmetric instabilities*. These instabilities, driven by hydrodynamic and gravitational forces, can arise in rapidly rotating neutron stars, particularly in newly formed stars or during accretion phases. If a newly born neutron star has a sufficiently high rotation rate (typically if $T/|W| \gtrsim 0.24$, where T is the rotational kinetic energy and W is the gravitational binding energy), it may be subject to dynamical instability driven by hydrodynamics and gravity. This instability can deform the star into a bar shape, which would be a strong source of gravitational waves, albeit likely short-lived (on the order of a few rotations).

The third mechanism for the emission of continuous gravitational waves from spinning neutron stars is *free precession*. This occurs when a neutron star's rotation axis is misaligned with its symmetry axis, causing the star to "wobble" like a spinning top. Generally, free precession leads to gravitational wave emission at approximately the rotation rate ν and at twice the rotation rate, specifically at frequencies $f = \nu + \nu_{\text{prec}}$ (where ν_{prec} is the precession frequency) and $f = 2\nu$.

[7] The interior of a bulk superconductor cannot be penetrated by a weak magnetic field, a phenomenon known as the *Meissner effect* (Meissner and Ochsenfeld 1933). Bulk *type-I superconductors* remain in the Meissner state with no field inside the sample if the external field is below a critical value H_c. They suddenly become normal metals when the external field is above H_c.

Chapter 2

Magnetic fields: origin and evolution

The astrophysical sources discussed in Chapter 1 exhibit extremely strong magnetic fields. The origin and evolution of these magnetic fields, particularly those of magnetars, are not fully understood. The magnetic fields of these stars are so intense that they significantly impact both their internal structure and their emissions, whether electromagnetic or gravitational.

Such intense fields physically deform the star (e.g., Mastrano et al. 2013, Mallick and Schramm 2014, Mastrano et al. 2015), inducing anisotropic forces causing a deviation from the spherical symmetry typical of a neutron star. Consequently, magnetars may assume an ellipsoidal shape, either elongated or flattened along the magnetic axis. The resulting internal stresses can lead to fractures in the star's crust, triggering explosive events known as "starquakes", which release enormous amounts of energy in a very short time. These events are often associated with violent gamma-ray and X-ray emissions.

In terms of electromagnetic emissions, magnetars are among the most powerful astrophysical sources. The physical processes occurring within these extremely intense magnetic fields generate extremely violent energy bursts, particularly visible in X-rays and gamma-rays. Events such as *soft gamma repeaters* (e.g., Thompson and Duncan 1995) are caused by *magnetic reconnection*, a process in which the magnetic field reorganizes itself and releases explosive energy. Moreover, electromagnetic emissions from a magnetar can be strongly polarized due to the interaction with the magnetic field, providing valuable information about its geometry. In such extreme environments, the properties of the quantum vacuum are modified: phenomena such as *vacuum birefringence* (Heisenberg and Euler 1936), typical of quantum electrodynamics, can alter the propagation of photons, changing the appearance and polarization of the emissions (Mignani et al. 2016).

A crucial role in the emissions of magnetars is played by the *synchrotron* process, which occurs when charged particles, such as electrons or protons, are accelerated to relativistic speeds within the extremely powerful magnetic fields of the magnetar. As

these particles move along curved trajectories induced by the magnetic field, they emit synchrotron radiation, which manifests across a wide spectrum of frequencies, from radio waves to X-rays and gamma rays. The synchrotron emissions of magnetars are particularly intense due to the strength of the magnetic field and are highly polarized.

Gravitational waves can also be produced by the immense magnetic field of a magnetar. The anisotropic deformations of the star can lead to the continuous emission of gravitational waves, albeit with lower intensity compared to more cataclysmic events such as the merger of black holes or neutron stars. Additionally, during starquakes, the fracturing of the star's crust can generate impulsive gravitational waves associated with these violent events. The detection of such signals using instruments like LIGO or Virgo is a primary goal in astrophysical research, despite the extreme difficulty posed by the weakness of the signal and the very high frequencies involved.

Beyond physical deformations and emissions, such an intense magnetic field can trigger magnetohydrodynamic instabilities within the magnetar. *Magnetic reconnection*, a phenomenon where field lines reorganize abruptly, can cause intense particle acceleration, increasing synchrotron radiation production and leading to flares observed as gamma-ray bursts or X-ray flares. These explosive processes are a direct consequence of the complex interaction between the magnetic field and the matter that composes the star.

Over time, the magnetic field of a magnetar tends to decay in a process known as *magnetic decay*. The energy stored in the field is gradually dissipated as radiation and heat, contributing to the cooling of the star. Even during this decay phase, the magnetar continues to emit radiation, especially in the soft X-ray band, although less violently than in the earlier stages of its life.

As previously mentioned, the origin of these intensely strong magnetic fields, as well as the processes underlying their evolution, remains a subject of ongoing discussion. In this chapter, we present an overview of the processes that have been proposed to date.

2.1 The fossil hypothesis

The fossil field hypothesis, also known as the "flux conservation hypothesis", was initially proposed by Woltjer 1964. According to this model, magnetic fields are merely remnants of the fields of their main sequence (MS) progenitors. However, this model faces several challenges.

Firstly, assuming a relatively uniform field, the flux contained within a neutron star's core would be insufficient to explain the intense magnetic fields observed in magnetars. Even if the progenitor star had a magnetic field as strong as 10^4 G, the strongest known in main sequence stars, the resulting field in the neutron star would only be around 10^{14} G.

Secondly, only a small fraction of main sequence stars have magnetic fields as strong as 10^4 G. Yet, the birth rate of magnetars is comparable to that of normal neutron stars.

This suggests that magnetars may have a different origin than normal pulsars. However, this raises the question of why a process capable of generating such intense magnetic fields in magnetar progenitors does not also operate, albeit at a lower strength, in the progenitors of normal pulsars.

2.2 Dynamo mechanism

The dynamo mechanism is a process through which a rotating, convecting, and electrically conducting fluid can generate a magnetic field by self-inductive action, converting kinetic energy into magnetic energy and maintaining it over astronomical time scales. (e.g., Moffatt 1983, Biskamp 1997, Brandenburg and Subramanian 2005).

When a conductor moves through a magnetic field, an electric field is induced. This electric field, in accordance with *Ohm's law*, generates a current. According to *Ampère's law*, this current produces a magnetic field. This newly generated magnetic field can, on the one hand, induce a new electric field through *Faraday's law*. On the other hand, it can oppose the motion of the conductor due to the *Lorentz force*. This is a highly nonlinear system.

However, for a lasting magnetic field to be established, the dynamo process must be self-sustaining. his means that the generated electric currents must reinforce the preexisting magnetic field rather than dissipate it. This is known as the "*self-sustaining dynamo effect*". The initial magnetic field (which can be very weak or even the result of magnetic remnants from the body's formation phase) deflects internal fluid motions, inducing new electric currents that, in turn, create or amplify the existing magnetic field. This creates a continuous cycle where the magnetic field and electric currents mutually sustain each other.

For the dynamo mechanism to be triggered, a certain degree of complexity in the motions of the conducting fluid is necessary. Specifically, there must be irregularities or deviations from axial symmetry. This means that three-dimensional, turbulent fluid motions, such as convective or differential motions, must break perfect symmetry to generate and sustain a long-lasting magnetic field. If a system were perfectly axisymmetric, the motions of the conducting fluid would be too regular to generate a self-sustaining magnetic field. The outcome would be the gradual dissipation of the magnetic field as a result of resistive effects, since, in a symmetric system, the field lacks the opportunity to "wrap around" and reinforce itself. In contrast, the breaking of axial symmetry allows the generation of vortices, irregular flows, and differential regions of motion, all of which enable electric currents to continually feed the magnetic field and keep it active. This is a well-known result of dynamo theory, often associated with the so-called "*anti-dynamo theorem*" (or Cowling's theorem), which states that axisymmetric magnetic fields cannot generate a self-sustaining dynamo.

This asymmetry can arise from various factors such as differential rotation, turbulent fluid motions, or variations in temperature and composition within the celestial

body. Even small perturbations or deviations from symmetry can trigger the dynamo mechanism.

Of particular importance is the so-called mean-field dynamo. This theory separates the total magnetic field and fluid motions into large-scale (mean) and small-scale (fluctuating) components. In this way, the observed magnetic field, which is generally the large-scale one, is modeled by accounting for the average influence of turbulent motions. In other words, the magnetic field ($\mathbf{B}$) and fluid velocity ($\mathbf{U}$) are rewritten as:

$$\mathbf{B} = \mathbf{B}_0 + \mathbf{b} \qquad \langle \mathbf{b} \rangle = 0 \qquad b \ll B_0 \tag{2.1}$$

$$\mathbf{U} = \mathbf{U}_0 + \mathbf{u} \qquad \langle \mathbf{u} \rangle = 0 \qquad u \ll U_0 \tag{2.2}$$

where $\mathbf{B}_0$ and $\boldsymbol{\mathcal{U}}_0$ represent the mean values, and $\mathbf{b}$ and $\mathbf{u}$ are the turbulent fluctuations.

From a classical (i.e., non-relativistic) perspective, the evolution of the magnetic field is described by the equation:

$$\partial_t \mathbf{B}_0 = \boldsymbol{\nabla} \times (\mathbf{U}_0 \times \mathbf{B}_0 + \boldsymbol{\mathcal{E}}) + \eta \nabla^2 \mathbf{B}_0 \tag{2.3}$$

where η is the magnetic diffusivity (or electrical resistivity, assumed to be constant here), and

$$\boldsymbol{\mathcal{E}} = \alpha \mathbf{B}_0 - \beta \boldsymbol{\nabla} \times \mathbf{B}_0 \tag{2.4}$$

is the *mean electromotive force* (EMF) representing the overall effect of turbulent fluctuations on the electric currents. Here

$$\alpha \approx -\frac{1}{3} \tau_{\text{cor}} \langle \mathbf{u} \cdot \boldsymbol{\nabla} \times \mathbf{u} \rangle \tag{2.5}$$

is the so-called *dynamo parameter*, and

$$\beta \approx \frac{1}{3} \tau_{\text{cor}} \langle \mathbf{u} \cdot \mathbf{u} \rangle \tag{2.6}$$

is the turbulent magnetic diffusivity, with τ_{cor} is the correlation time of the turbulence.

Mean-field dynamos are typically classified into two types (Figure 2.1). In the α^2-dynamo, turbulent fluctuations and rotation generate a poloidal field from a pre-existing toroidal field. Subsequently, the same α-*effect* converts part of this poloidal field back into a toroidal field. In the $\alpha\Omega$-dynamo, the α-effect is responsible for generating the poloidal field, while the Ω-*effect* (resulting from differential rotation) transforms the poloidal field into a toroidal field.

In the case of the Sun, the ($\alpha\Omega$-)dynamo mechanism occurs in the transition zone between the inner radiative layer and the outer convective layer, in a region known as the "*tachocline*". In this region, the conductive plasma moves under the influence of the Sun's differential rotation, generating a magnetic field that varies cyclically, thereby elucidating the 11-year solar cycle characterized by the periodic increase and decrease of sunspots.

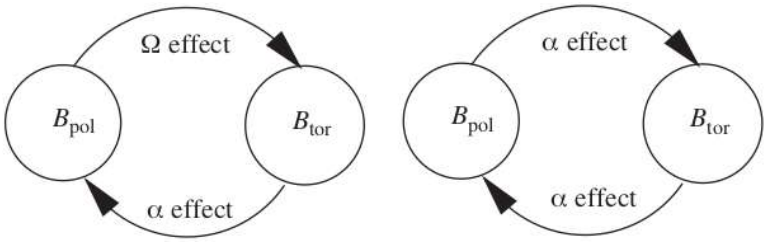

Figure 2.1: Mutual regeneration of poloidal and toroidal fields in the case of the $\alpha\Omega$-dynamo (left) and the α^2-dynamo (right) (Brandenburg and Subramanian 2005).

A tachocline is hypothesized to exist within proto-neutron stars, at the boundary between two unstable zones (e.g., Bonanno et al. 2003, Naso et al. 2008). In the inner *convectively unstable* region, hydrodynamic instabilities are driven by negative entropy gradients, while in the *neutron-finger unstable* region, they are driven by lepton gradients. The *neutron-finger instability* (NFI) operates in the outer regions of the proto-neutron star and is expected to evolve by generating finger-like downflows when the neutrinos are still confined. The presence of the NFI and the tachocline in proto-neutron stars remains a matter of ongoing investigation and controversy within the scientific community.

2.3 Magnetorotational instability

The *magneto-rotational instability* (MRI, Figure 2.2) occurs when an electrically conducting fluid, subjected to a magnetic field, rotates. Under these conditions, instabilities can arise, leading to the formation of vortices and turbulent motions. This instability was initially observed by Evgeny Velikhov in 1959 while studying the stability of Couette flow in an ideal hydromagnetic fluid (Velikhov 1959). This work was later generalized by Chandrasekhar 1960. Although these studies focused on phenomena in non-astrophysical contexts, their significance became apparent when D. J. Acheson and Raymond Hide proposed in 1973 that the instability could play a role in the Earth's geodynamo problem (Acheson and Hide 1973). Despite some subsequent work in the following years, the general understanding and power of the instability were not fully appreciated until 1991, when Steven A. Balbus and John F. Hawley provided a relatively simple explanation and physical description of this crucial process in an astrophysical context (Balbus and Hawley 1991).

The magnetorotational instability has become a key concept for understanding turbulence in accretion disks, where the magnetic field and rotation interact in complex ways. Its significance is evident in the study of phenomena such as the accretion of matter onto black holes and the emission of radiation from the accretion disks surrounding neutron stars and young stars.

In an accretion disk, matter moves toward a central object, and the gravitational

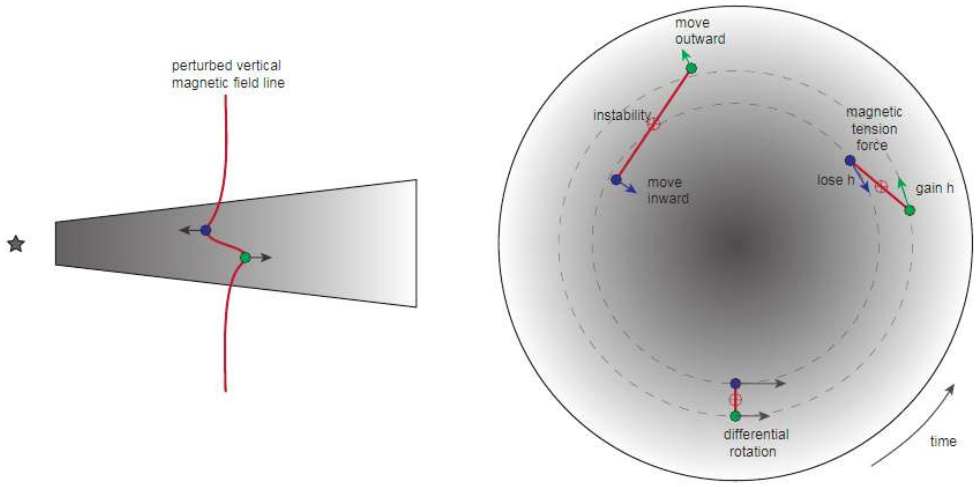

Figure 2.2: Magnetorotational instability for a perturbed vertical magnetic field in ideal magnetohydrodynamics (Armitage 2022).

force acts to pull it in. If the disk is sufficiently hot, the matter within it can conduct electricity. As the disk rotates, the magnetic field lines present can interact with the motion of the plasma, leading to instabilities. This interaction is particularly pronounced when the rotational velocity of the disk decreases with distance from the center, creating a situation where magnetic pressure can contribute to destabilizing the flow.

The mechanism of magnetorotational instability is characterized by the presence of magnetic fields and the disk's ability to transport angular momentum. In this context, the disk's rotation and the magnetic field generate a configuration that allows for the exponential growth of small perturbations in the plasma. Once amplified, these perturbations can lead to the formation of turbulence, which in turn increases the efficiency with which the material can lose angular momentum and fall towards the central body.

As highlighted in Reboul-Salze et al. 2021, MRI may function as a promising mechanism for amplifying the magnetic field in fast rotating proto-neutron stars, facilitating the formation of magnetars.

2.4 Kelvin–Helmholtz instability

The *Kelvin-Helmholtz instability* is a phenomenon that occurs when two fluids with differing velocities come into contact, creating waves that can lead to the formation of complex structures.

The underlying principle of the Kelvin-Helmholtz instability is the velocity shear between two fluid layers. When one layer moves faster than the other, the interface between them becomes unstable. Small perturbations at this interface amplify, giving rise to waves that can grow into vortices or other turbulent structures. This process

is often accompanied by energy release, enhancing turbulence and promoting mixing between the two fluids.

The Kelvin-Helmholtz instability can occur during the merger of two neutron stars (e.g., Obergaulinger et al. 2010, Kiuchi et al. 2015). As the neutron stars approach each other, gravitational interactions can strip away their outer atmospheres, forming an accretion disk around the binary system. The material from each star moves at different velocities within this disk, leading to velocity shear that can trigger Kelvin-Helmholtz instabilities, resulting in waves and turbulence.

Furthermore, the presence of strong magnetic fields can amplify these instabilities. The interplay between differential fluid motion and magnetic interactions can generate vortices and complex structures, contributing to the turbulent dynamics of the merger event. These structures can influence the emission of electromagnetic radiation, such as radio waves or gamma-rays, making neutron star mergers a source of explosive events like gamma-ray bursts.

The Kelvin-Helmholtz instability can play a significant role as a seed to both the dynamo process and the magnetorotational instability.

Chapter 3

Mathematical Framework

The study of the evolution of a system in general relativity (GR) represents a complex challenge, as it requires the simultaneous solution of Einstein, Euler and Maxwell equations. These equations govern spacetime dynamics, fluid dynamics, and electromagnetism, respectively, thus representing the theoretical foundations necessary to describe complex astrophysical phenomena.

In this chapter, we focus on the equations of magnetohydrodynamics (MHD), a theory that combines the principles of hydrodynamics with those of electromagnetism to describe the behavior of conducting fluids in the presence of magnetic fields. In particular, resistive magnetohydrodynamics (RMHD) extends the idealized theory of MHD to include the effects of electrical resistivity, which are crucial for accurately describing plasma dynamics under realistic astrophysical conditions.

We begin by presenting the equations in the covariant approach, which offers a compact and elegant description of the laws of physics in tensor form, making evident the invariance of the equations under coordinate transformations. This formalism is particularly useful for highlighting the geometric properties of equations. However, from a numerical point of view, the covariant approach has significant disadvantages. Its completely four-dimensional formulation does not lend itself easily to the separation of spatial and temporal variables, making the implementation of effective numerical methods complex. In addition, the abstract nature and intricate structure of tensor equations make it difficult to define boundary conditions and stable and accurate numerical schemes of temporal evolution.

To overcome these limitations, we present the so-called 3+1 formalism, the most widely used method in numerical relativity. This approach makes it possible to decompose covariant equations into a form more suitable for numerical solving, explicitly separating spatial and temporal variables. The 3+1 formalism allows a more direct treatment of initial conditions and evolutionary equations, facilitating the numerical simulation of the time evolution of astrophysical systems in GR.

3.1 Covariant approach

The relativistic Euler equations are a set of quasi-linear partial differential equations governing inviscid flow taking into account the effects of GR. This set of equations consists of the *baryon number* (or equivalently *mass*) *conservation*

$$\nabla_\mu N^\mu = 0 \tag{3.1}$$

and the *energy-momentum conservation*

$$\nabla_\mu T^{\mu\nu} = 0 \tag{3.2}$$

where N^ν is the 4-vector number current, $T^{\mu\nu}$ the energy-momentum tensor, and ∇_μ the geometric covariant derivative associated to the metric tensor $g_{\mu\nu}$, i.e. $\nabla_\lambda g_{\mu\nu} = 0$. The energy-momentum tensor is a symmetric tensor, source of the gravitational field in the *Einstein field equations*

$$R_{\mu\nu} - \frac{1}{2} R g_{\mu\nu} = 8\pi T_{\mu\nu} \tag{3.3}$$

or, equivalently,

$$R_{\mu\nu} = 8\pi\left(T_{\mu\nu} - \frac{1}{2} T g_{\mu\nu}\right) \tag{3.4}$$

where $R_{\mu\nu}$ is the Ricci curvature tensor, $R = R^{\mu\nu} g_{\mu\nu}$ the scalar curvature (corresponding to the trace of the Ricci tensor), and $T = T^{\mu\nu} g_{\mu\nu}$ the trace of the energy-momentum tensor.

The energy-momentum tensor consists of two terms which are not conserved when considered separately:

$$\nabla_\mu T^{\mu\nu}_m = -\nabla_\mu T^{\mu\nu}_{em} = -I_\mu F^{\mu\nu} \tag{3.5}$$

where $T^{\mu\nu}_m$ is the contribution to the energy-momentum tensor due to matter, $T^{\mu\nu}_{em}$ that due to the electromagnetic field, I^μ the 4-current, and $F^{\mu\nu}$ the Faraday (antisymmetric) electromagnetic tensor. The relation between $T^{\mu\nu}_{em}$ and $F^{\mu\nu}$ is

$$T^{\mu\nu}_{em} = F^\mu{}_\lambda F^{\nu\lambda} - \frac{1}{4}\left(F^{\lambda\kappa} F_{\lambda\kappa}\right) g^{\mu\nu} \tag{3.6}$$

The electromagnetic field obeys *Maxwell equations*

$$\nabla_\mu F^{\mu\nu} = -I^\nu \tag{3.7}$$

$$\nabla_\mu F^{*\mu\nu} = 0 \tag{3.8}$$

where $F^{*\mu\nu} = \frac{1}{2}\varepsilon^{\mu\nu\lambda\kappa} F_{\lambda\kappa}$ is the dual of the Faraday tensor, with $\varepsilon^{\mu\nu\lambda\kappa}$ the spacetime Levi-Civita tensor density, related to the standard Levi-Civita symbol $[\mu\nu\lambda\kappa]$ via the relation $\varepsilon^{\mu\nu\lambda\kappa} = \frac{1}{\sqrt{-g}}[\mu\nu\lambda\kappa]$ (and $\varepsilon_{\mu\nu\lambda\kappa} = \sqrt{-g}[\mu\nu\lambda\kappa]$) with $g = \det[g_{\mu\nu}]$.

Given a timelike[8] 4-vector u^μ normalized as $u^\mu u_\mu = -1$, each quantity defined above can be decomposed into a parallel timelike and an orthogonal spacelike part:

$$N^\mu = \rho u^\mu + N^\mu_\perp \tag{3.9}$$
$$F^{\mu\nu} = u^\mu e^\nu - u^\nu e^\mu + \varepsilon^{\mu\nu\lambda\kappa} b_\lambda u_\kappa \tag{3.10}$$
$$F^{*\mu\nu} = u^\mu b^\nu - u^\nu b^\mu - \varepsilon^{\mu\nu\lambda\kappa} e_\lambda u_\kappa \tag{3.11}$$
$$I^\mu = q_0 u^\mu + j^\mu \tag{3.12}$$
$$T^{\mu\nu}_m = (\rho h - p) u^\mu u^\nu + p\Delta^{\mu\nu} + q^\mu u^\nu + q^\nu u^\mu + \tau^{\mu\nu} \tag{3.13}$$
$$T^{\mu\nu}_{em} = u_{em} u^\mu u^\nu + p^\mu u^\nu + p^\nu u^\mu + u_{em}\Delta^{\mu\nu} - e^\mu e^\nu - b^\mu b^\nu \tag{3.14}$$

with

$$N^\mu_\perp u_\mu = e^\mu u_\mu = b^\mu u_\mu = j^\mu u_\mu = q^\mu u_\mu = p^\mu u_\mu = 0 \tag{3.15}$$

and

$$\Delta^{\mu\nu} u_\nu = \tau^{\mu\nu} u_\nu = 0 \tag{3.16}$$

Here ρ is the *rest mass density*, p the *thermal pressure*, $h = 1 + \epsilon + p/\rho$ the *specific enthalpy* - with ϵ the *specific internal energy* -, $N^\mu_\perp$ the 4-vector particle current, q^μ the 4-vector energy flow, $\tau^{\mu\nu}$ the viscous stress-tensor, $\Delta^{\mu\nu} = g^{\mu\nu} + u^\mu u^\nu$ the projection operator, e^μ the 4-vector electric field, b^μ the 4-vector magnetic field, j^μ the 4-vector conduction current density, $u_{em} = \left(e^2 + b^2\right)/2$ the electromagnetic energy density, q_0 the proper electric charge density, and $p^\mu = \varepsilon^{\mu\lambda\kappa} e_\lambda b_\kappa$ - with $\varepsilon^{\mu\lambda\kappa} = \varepsilon^{\mu\lambda\kappa\tau} u_\tau$ - the Poyting 4-vector. All these quantities are measured by the observer with 4-velocity u^μ. This implies the presence of an ambiguity in their definition. Three possible frames are

- *Eckart* or *material* or *comoving* frame (Eckart 1940): the particle current vanishes, i.e. $N^\mu_\perp = 0$.
- *Landau-Lifshitz* or *energy* frame (Landau and Lifshitz 1987): the energy flow vanishes, i.e. $q^\mu = 0$.
- *Jüttner* or *thermometer* or β frame: the thermometer is at local equilibrium with the system; $\beta^\mu = u^\mu/T$, where T is the temperature and β^μ is the Lagrange multiplier emerging in the Maxwell-Boltzmann distribution.

Other flow frames are also possible. For a *perfect* (or *ideal*) *fluid* - assumed in this work - we have $N^\mu_\perp = q^\mu = \tau^{\mu\nu} = 0$, the frames coincide and Equation (3.13) becomes

$$T^{\mu\nu}_m = (\rho h - p) u^\mu u^\nu + p\Delta^{\mu\nu} \tag{3.17}$$

[8] A 4-vector is said to be *timelike* if its norm is negative, *spacelike* if its norm is positive, and *lightlike* if its norm is zero.

3.2 3+1 decomposition

In the covariant approach described in the previous section, there is no distinction between space and time coordinates. While this "covariance" is mathematically important and elegant, the covariant formulation is difficult to use in numerical analysis. Indeed, numerical methods require the separation of time and space. The most used approach to decompose the spacetime into "space" + "time" is the *3+1 decomposition* (Alcubierre 2008, Baumgarte and Shapiro 2010, Gourgoulhon 2012). The 4D spacetime is foliated into non-intersecting space-like hypersurfaces $(\Sigma_t)_{t\in\mathbb{R}}$, i.e., hypersurfaces with a time-like unit normal vector n^ν, which is the 4-velocity of the observer moving along the worldline orthogonal to the hypersurface, called *Eulerian observer*.

3.2.1 3+1 decomposition for the metric

The 4D line element is written as

$$\mathrm{d}s^2 = \left(-\alpha^2 + \beta^i\beta_i\right)\mathrm{d}t^2 + 2\beta_i \mathrm{d}t\mathrm{d}x^i + \gamma_{ij}\mathrm{d}x^i\mathrm{d}x^j \tag{3.18}$$

where $\alpha\left(t, x^j\right) \in (0, 1]$ is called *lapse function*, $\beta^i\left(t, x^j\right)$ is called *shift vector*, and γ_{ij} is the 3D *induced metric* (or *spatial metric*), with Riemannian signature $(+,+,+)$. The lapse function relates the "coordinate time" $\mathrm{d}t$ to the proper time $\mathrm{d}\tau$ measured by the Eulerian observer: $\mathrm{d}\tau = \alpha \mathrm{d}t$. The shift vector is the relative velocity between the Eulerian observer and the lines of constant spatial coordinates: $x^i(t + \mathrm{d}t) = x^i(t) - \beta^i(t, x^j)\mathrm{d}t$. Notice that α and β^i are not unique but depend on the arbitrarily chosen foliation. These quantities, therefore, contain information about the chosen coordinates. The 4D metric is then

$$g_{\mu\nu} = \left(\begin{array}{c|c} -\alpha^2 + \beta_i\beta^i & \beta_i \\ \hline \beta_j & \gamma_{ij} \end{array}\right) \qquad g^{\mu\nu} = \left(\begin{array}{c|c} -1/\alpha^2 & \beta^i/\alpha^2 \\ \hline \beta^j/\alpha^2 & \gamma^{ij} - \beta^i\beta^j/\alpha^2 \end{array}\right) \tag{3.19}$$

The 4D volume element is therefore given by $\sqrt{-g} = \alpha\sqrt{\gamma}$, where $\gamma = \det\left[\gamma_{ij}\right]$. The unit vector components are

$$n^\mu = \left(1/\alpha, -\beta^i/\alpha\right) \qquad n_\mu = (-\alpha, 0_i) \tag{3.20}$$

Its covariant derivative can be written as

$$\nabla_\mu n_\nu = -K_{\mu\nu} - n_\mu n^\alpha \nabla_\alpha n_\nu \tag{3.21}$$

where the symmetric tensor $K_{\mu\nu}$ is known as *extrinsic curvature*. The extrinsic curvature should not be confused with the *intrinsic curvature*: the former measures how the normal vector n^μ changes along the hypersurface under parallel transport, while the latter one describes the curvature at a point on the surface and is given by the 3D Riemann tensor, which is defined in terms of γ_{ij}. The extrinsic curvature is such that

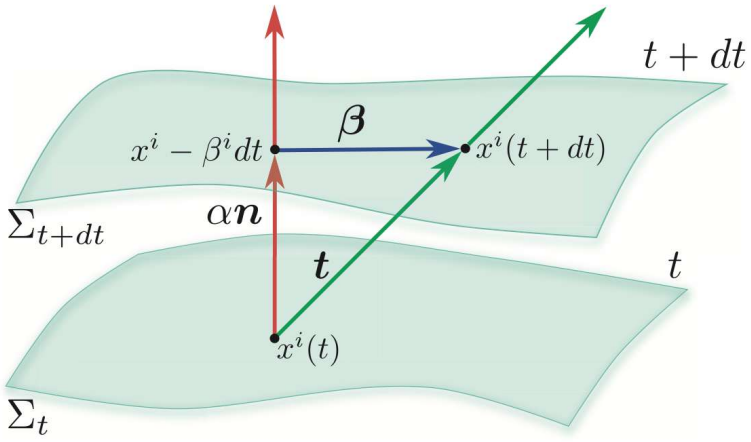

Figure 3.1: Schematic representation of the 3+1decomposition (Rezzolla and Zanotti 2013).

$n^\mu K_{\mu\nu} = 0$. This means that $K^{00} = K^{i0} = 0$ (but K_{00} and K_{i0} are in general not zero). The extrinsic curvature also measures how the spatial metric changes in time as seen by the Eulerian observer:

$$\mathfrak{L}_n \gamma_{ij} = -2K_{ij} \tag{3.22}$$

where $\mathfrak{L}_n$ is the Lie derivative along n^μ, or, equivalently,

$$\partial_t \gamma_{ij} = -2\alpha K_{ij} + \mathscr{D}_i \beta_j + \mathscr{D}_j \beta_i \tag{3.23}$$

where $\mathscr{D}_i$ is the 3D covariant derivative (i.e. associated with the 3-metric γ_{ij}, $\mathscr{D}_k \gamma_{ij} = 0$). Finally, Equation (3.21) gives

$$\partial_t \sqrt{\gamma} = \sqrt{\gamma}\left(-\alpha K + \mathscr{D}_i \beta^i\right) \tag{3.24}$$

where $K = \gamma^{ij} K_{ij} = -\nabla_\mu n^\mu$ is the trace of K_{ij}.

A schematic representation of the 3+1decomposition is shown in Figure 3.1.

3.2.2 3+1 decomposition for vectors and tensors

We can now decompose vectors and tensors into parallel timelike and orthogonal spacelike components to n^μ. A vector V^μ can therefore be written as

$$V^\mu = N n^\mu + V^\mu_\perp \tag{3.25}$$

with $N = -n_\mu V^\mu$ and $V^\mu_\perp n_\mu = 0$, while a tensor $T^{\mu\nu}$ can be written as

$$T^{\mu\nu} = T n^\mu n^\nu + Q^\mu n^\nu + P^\nu n^\mu + W^{\mu\nu} \tag{3.26}$$

with $T = T^{\mu\nu} n_\mu n_\nu$, $Q^\mu n_\mu = P^\mu n_\mu = 0$, and $W^{\mu\nu} n_\mu = W^{\mu\nu} n_\nu = 0$. For a symmetric tensor we have $P^\mu = Q^\mu$, while for an antisymmetric tensor we have $P^\mu = -Q^\mu$ and $T = 0$.

It is important to note that - for each vector V^μ and tensor $T^{\mu\nu}$ - conditions $V^\mu n_\mu = 0$ and $T^{\mu\nu} n_\mu = T^{\mu\nu} n_\nu = 0$ imply

$$V^0 = T^{0\nu} = T^{\mu 0} = 0 \tag{3.27}$$

but, in general, V_0, $T_{0\nu}$, and $T_{\mu 0}$ are not zero. In fact

$$V_0 = \beta_i V^i \qquad V_i = \gamma_{ij} V^j \tag{3.28}$$

and

$$T_{\mu\nu} = g_{\mu i}\, g_{\nu j}\, T^{ij} \tag{3.29}$$

that is

$$T_{00} = \beta_i \beta_j T^{ij} \qquad T_{k0} = \gamma_{ki} \beta_j T^{ij} = T_k{}^j \beta_j \tag{3.30}$$

$$T_{0k} = \beta_i \gamma_{kj} T^{ij} = \beta_i T^i_{\ k} \qquad T_{kl} = \gamma_{ki} \gamma_{lj} T^{ij} \tag{3.31}$$

Finally, for each 3-vector $\mathbf{V}$ we have

$$\boldsymbol{\nabla} \cdot \mathbf{V} = \mathscr{D}_i V^i = \frac{1}{\sqrt{\gamma}} \partial_i \big(\sqrt{\gamma}\, V^i \big) \tag{3.32}$$

$$(\boldsymbol{\nabla} \times \mathbf{V})^i = \varepsilon^{ijk} \partial_j V_k = \frac{1}{\sqrt{\gamma}} [ijk] \partial_j V_k \tag{3.33}$$

with $\partial_i = \partial / \partial x^i$ and $\varepsilon^{ijk} = -\varepsilon^{0ijk} n_0 = \frac{1}{\sqrt{\gamma}} [ijk]$ (and $\varepsilon_{ijk} = \sqrt{\gamma} [ijk]$).

3.2.3 3+1 decomposition for Euler and Maxwell equations

At this point it is possible to decompose all quantities introduced in Section 3.1 as

$$u^\mu = W n^\mu + W v^\mu \tag{3.34}$$

$$N^\mu = D n^\mu + F^\mu \tag{3.35}$$

$$T^{\mu\nu} = \mathcal{E} n^\mu n^\nu + S^\mu n^\nu + S^\nu n^\mu + S^{\mu\nu} \tag{3.36}$$

$$F^{\mu\nu} = n^\mu E^\nu - E^\mu n^\nu + \varepsilon^{\mu\nu\lambda\kappa} B_\lambda n_\kappa \tag{3.37}$$

$$F^{*\mu\nu} = n^\mu B^\nu - B^\mu n^\nu - \varepsilon^{\mu\nu\lambda\kappa} E_\lambda n_\kappa \tag{3.38}$$

$$I^\mu = q n^\mu + J^\mu \tag{3.39}$$

$$e^\mu = W \Big[(\mathbf{E} \cdot \mathbf{v}) n^\mu + E^\mu + \varepsilon^{\mu\lambda\sigma} v_\lambda B_\sigma \Big] \tag{3.40}$$

$$b^\mu = W \Big[(\mathbf{B} \cdot \mathbf{v}) n^\mu + B^\mu - \varepsilon^{\mu\lambda\sigma} v_\lambda E_\sigma \Big] \tag{3.41}$$

$$j^\mu = (q - q_0 W) n^\mu + J^\mu - q_0 W v^\mu \tag{3.42}$$
$$q_0 = W(q - \mathbf{J} \cdot \mathbf{v}) \tag{3.43}$$

where

$$W = 1/\sqrt{1 - v^2} \quad \text{(Lorentz factor)} \tag{3.44}$$
$$D = W\rho \quad \text{(rest mass density)} \tag{3.45}$$
$$\mathcal{E} = \mathcal{E}_F + U_{em} \quad \text{(total energy density)} \tag{3.46}$$
$$S^i = M^i + P^i \quad \text{(total momentum)} \tag{3.47}$$
$$E^i \quad \text{(electric field)} \tag{3.48}$$
$$B^i \quad \text{(magnetic field)} \tag{3.49}$$
$$J^i \quad \text{(current density)} \tag{3.50}$$
$$q \quad \text{(electric charge density)} \tag{3.51}$$
$$F^i = W\rho\bar{v}^i \tag{3.52}$$
$$S^{ij} = \rho h W^2 v^i v^j - E^i E^j - B^i B^j + (p + U_{em})\gamma^{ij} \tag{3.53}$$

with

$$\bar{v}^i = \alpha v^i - \beta^i \tag{3.54}$$
$$\mathcal{E}_F = \rho h W^2 - p \quad \text{(fluid energy density)} \tag{3.55}$$
$$M^i = \rho h W^2 v^i \quad \text{(fluid momentum)} \tag{3.56}$$
$$P^i = \varepsilon^{ijk} E_j B_k \quad \text{(Poynting vector)} \tag{3.57}$$
$$U_{em} = \big(E^2 + B^2\big)/2 \quad \text{(electromangetic energy density)} \tag{3.58}$$

With this decomposition, Euler and Maxwell equations become

$$\partial_t \tilde{D} + \partial_k \Big(\tilde{D}\bar{v}^k\Big) = 0 \tag{3.59}$$
$$\partial_t \tilde{\mathcal{E}} + \partial_k \Big(\alpha \tilde{S}^k - \tilde{\mathcal{E}}\beta^k\Big) = \alpha\sqrt{\gamma}\, S^{lm} K_{lm} - \tilde{S}^k \partial_k \alpha \tag{3.60}$$
$$\partial_t \tilde{S}_i + \partial_k \Big(\alpha\sqrt{\gamma}\, S^k{}_i - \beta^k \tilde{S}_i\Big) = \frac{\alpha\sqrt{\gamma}}{2} S^{lm} \partial_i \gamma_{lm} + \tilde{S}_k \partial_i \beta^k - \tilde{\mathcal{E}} \partial_i \alpha \tag{3.61}$$
$$\partial_t \tilde{B}^i + [ijk]\partial_j \Big(\alpha E_k + [klm]\beta^l \tilde{B}^m\Big) = 0 \tag{3.62}$$
$$\partial_t \tilde{E}^i - [ijk]\partial_j \Big(\alpha B_k - [klm]\beta^l \tilde{E}^m\Big) = -\alpha\sqrt{\gamma}\, J^i + \sqrt{\gamma}\, q\beta^i \tag{3.63}$$
$$q = \mathscr{D}_i E^i \tag{3.64}$$
$$\mathscr{D}_i B^i = 0 \tag{3.65}$$

where $\tilde{A} = \sqrt{\gamma}\, A$ for each quantity A. The last two equations can be rewritten as

$$\sqrt{\gamma}\, q = \partial_i \tilde{E}^i \tag{3.66}$$

$$\partial_i \tilde{B}^i = 0 \tag{3.67}$$

The vector form of Euler and Maxwell equations is[9]

$$\partial_t(\sqrt{\gamma}\, D) + \sqrt{\gamma}\boldsymbol{\nabla}\cdot(D\bar{\mathbf{v}}) = 0 \tag{3.68}$$

$$\partial_t(\sqrt{\gamma}\, \mathcal{E}) + \sqrt{\gamma}\boldsymbol{\nabla}\cdot(\alpha\mathbf{S} - \mathcal{E}\boldsymbol{\beta}) = \sqrt{\gamma}\Big(\alpha\overline{\overline{\boldsymbol{S}}} : \overline{\overline{\boldsymbol{K}}} - \mathbf{S}\cdot\boldsymbol{\nabla}\alpha\Big) \tag{3.69}$$

$$\partial_t(\sqrt{\gamma}\, \mathbf{S}) + \sqrt{\gamma}\boldsymbol{\nabla}\cdot\Big(\alpha\overline{\overline{\boldsymbol{S}}} - \boldsymbol{\beta}\mathbf{S}\Big) = \sqrt{\gamma}[\mathbf{S}\cdot(\boldsymbol{\nabla}\boldsymbol{\beta}) - \mathcal{E}\boldsymbol{\nabla}\alpha] \tag{3.70}$$

$$\partial_t(\sqrt{\gamma}\, \mathbf{B}) + \sqrt{\gamma}\boldsymbol{\nabla}\times(\alpha\mathbf{E} + \boldsymbol{\beta}\times\mathbf{B}) = \mathbf{0} \tag{3.71}$$

$$\partial_t(\sqrt{\gamma}\, \mathbf{E}) - \sqrt{\gamma}\boldsymbol{\nabla}\times(\alpha\mathbf{B} - \boldsymbol{\beta}\times\mathbf{E}) = -\sqrt{\gamma}(\alpha\mathbf{J} - q\boldsymbol{\beta}) \tag{3.72}$$

$$q = \boldsymbol{\nabla}\cdot\mathbf{E} \tag{3.73}$$

$$\boldsymbol{\nabla}\cdot\mathbf{B} = 0 \tag{3.74}$$

This is not a complete set of equations, but requires some additional constraints to admit a unique solution: a relation between pressure, density and internal energy, and an expression for the current density. Possible choices are described below.

3.3 Equation of State

To close the system, we need a way to relate pressure, density, and internal energy. The most used way is to give a relationship between these three quantities, the so-called *Equation of State* (EoS). The equation of state is a fundamental relation that describes the behavior of a physical system in terms of its thermodynamic variables. It plays a crucial role in understanding the propagation of sound waves within a fluid. The speed of sound, defined as the rate at which a pressure wave propagates, is intimately connected to the EOS through the partial derivatives of physical quantities. Specifically, the speed of sound c_s in a relativistic fluid can be expressed as (Alcubierre 2008)

$$c_s^2 = \frac{1}{h}\left.\frac{\partial p}{\partial e}\right|_s \tag{3.75}$$

This formula indicates that the speed of sound is determined by the variation of pressure with respect to energy density $e = \rho(1+\epsilon)$, while keeping the entropy s of the system constant. This connection highlights how the properties of the fluid influence the propagation of sound waves: a change in pressure in response to a variation in energy density directly affects the speed at which perturbations propagate through the

[9] Here the notation $\overline{\overline{\boldsymbol{T}}}$ denotes a second-order spatial tensor.

fluid. Therefore, the equation of state provides an essential theoretical framework for analyzing and understanding the behavior of sound waves in a relativistic context.

Equation (3.75) can be rewritten as

$$c_s^2 = \frac{1}{h}\left(\frac{\partial p}{\partial \rho} + \frac{p}{\rho^2}\frac{\partial p}{\partial \epsilon}\right) \tag{3.76}$$

Calculating the pressure derivatives is straightforward for analytical equations of state. One of the simplest is the *polytropic*, in which the pressure is a function only of the density:

$$p = K\rho^{\Gamma} \tag{3.77}$$

where $K > 0$ is the *polytropic constant* and $\Gamma \geq 1$ the *polytropic index*. The specific internal energy results to be

$$\epsilon = \frac{K}{\Gamma - 1}\rho^{\Gamma - 1} \tag{3.78}$$

This is a one-dimensional EoS, and it is known that this type of equation is unable to conserve both density and total energy simultaneously. Nonetheless, one-dimensional equations of state, in which a fixed relationship exists between density and energy, are typically used in the absence of dynamic evolution and may be regarded as fixed-temperature (zero-temperature) equations.

The polytrope is a particular case of the *Ideal fluid* EoS (also known as Γ-law EoS):

$$p = (\Gamma_{\rm th} - 1)\rho\epsilon \tag{3.79}$$

The parameter $\Gamma_{\rm th}$ depends on the heat capacity of the fluid. For example, for a non-relativistic ideal monatomic gas, we have $\Gamma_{\rm th} = 5/3$, while for a relativistic one, $\Gamma_{\rm th} = 4/3$.

A third analytical equation, particularly appropriate for astrophysical jets, is the so-called *Taub* EoS (Mignone and McKinney 2007, Mattia et al. 2023):

$$p = \frac{\rho\epsilon}{3}\frac{\epsilon + 2}{\epsilon + 1} \tag{3.80}$$

Unlike the Ideal Fluid and Taub equations of state, the polytropic EoS is a zero-temperature equation. To address this limitation, it has been proposed to modify it by adding a thermal term derived from the Ideal Fluid as follows (Douchin and Haensel 2001):

$$p = \Gamma_{\rm th}\rho(\epsilon - \epsilon_{\rm cold}) \tag{3.81}$$

where $\epsilon_{\rm cold}$ is the specific internal energy given by the polytropic expression. However, within objects such as neutron stars, density varies drastically from the surface (where densities approach atomic levels) to the core (where densities are extremely high,

exceeding nuclear levels). In each density region, matter exhibits very different characteristics, requiring a specific description. The polytropic EOS is unable to capture these significant structural changes. To overcome this limitation, *piecewise polytropes* have been proposed as a replacement for the polytropic EoS (Read et al. 2009). This model describes the pressure-density relation in a fluid through a series of polytropic segments, each valid within a specific density interval:

$$p_{\text{cold}} = K_i \rho^{\Gamma_i} \qquad \text{for} \qquad \rho_{i-1} \leq \rho \leq \rho_i \tag{3.82}$$

for each segment i. The parameters K_i are chosen to ensure continuity of pressure and internal energy, given by

$$\epsilon_{\text{cold}} = \epsilon_i + \frac{K_i}{\Gamma_i - 1} \rho^{\Gamma_i - 1} \tag{3.83}$$

with

$$\epsilon_i = \epsilon_{\text{cold}}(\rho_{i-1}) - \frac{K_i}{\Gamma_i - 1} \rho_{i-1}^{\Gamma_i - 1} \tag{3.84}$$

While piecewise polytropes offer the advantage of better adapting to the varying properties of matter at different densities, they suffer from the drawback of having a discontinuous sound speed, defined piecewise (Appendix C of De Pietri et al. 2020).

More realistic equations of state, which account for nuclear and subnuclear interactions, relativistic effects, and long-range interactions, lack a true analytical expression and are instead provided as numerical tables in online repositories like `CompOSE`[10] (Typel et al. 2015). These tables include specific values for density, temperature, and sometimes electron fraction, allowing for the description of various matter states under different conditions. The data points are organized into grids of density and temperature values. Even if the values needed for simulation do not align precisely with grid points, they can be calculated via interpolation, typically linear or spline-based. This grid-based format is essential for numerical applications and enables simulations to explore realistic conditions without the need to calculate properties from scratch at every state change.

Despite their widespread use in simulations, tabulated equations of state exhibit several inherent limitations that can compromise accuracy and efficiency. Firstly, the discrete nature of the data, due to the fixed grid of density and temperature values, limits resolution and can lead to a loss of information, especially in critical regions such as phase transitions. Interpolation, employed to estimate values between grid points, inevitably introduces errors, particularly in regions where physical properties vary rapidly. These errors can propagate through the simulation, resulting in inaccurate outcomes. Secondly, the size of the tables poses a significant challenge. To ensure sufficient accuracy, a large number of grid points must be included, leading to increased table size and memory consumption. This can substantially slow down simulations,

[10] https://compose.obspm.fr

especially three-dimensional simulations of complex astrophysical objects that require frequent access to the table data. Finally, tabulated EoS are constructed for a specific range of density and temperature. If simulation conditions reach values outside of this range, the representation provided by the table becomes inadequate, potentially leading to calculation errors or unreliable results. This inadequacy arises because the thermodynamic properties of matter are not well-defined beyond the pre-calculated range in the table: without data covering these conditions, interpolation cannot reliably estimate the physical properties. Consequently, the simulation loses precision and reliability in regions not covered by the table and one needs to use an extended version of the table able to cover the whole range of density that is going to be simulated.

3.3.1 Taub's inequality

In the most general case, ρ, ϵ and p lie in ranges

$$\rho \in [0, \infty) \qquad \epsilon \in (-1, \infty) \qquad p \in [0, \infty) \tag{3.85}$$

although the upper and lower bounds may change depending on the EoS. However, in 1948 it was proved by Taub that to ensure consistency with the kinetic relativistic theory ρ, ϵ and p must respect the so-called *Taub's fundamental inequality* (Taub 1948):

$$(h - \Theta)(h - 4\Theta) \geq 1 \tag{3.86}$$

where $\Theta = p/\rho$ is the temperature function. Taub EoS (3.80) is obtained by imposing the equal sign in the previous inequality.

The Ideal Fluid EoS satisfies Taub's inequality for all values of ϵ if $\Gamma_{\rm th} \leq 4/3$. In contrast, it does not satisfy this inequality for any value of ϵ when $\Gamma_{\rm th} \geq 5/3$, while in the intermediate range $4/3 < \Gamma_{\rm th} < 5/3$ the inequality holds only if

$$\epsilon \leq \frac{5 - 3\Gamma_{\rm th}}{3\Gamma_{\rm th} - 4} \qquad \text{with} \qquad \Gamma_{\rm th} \in \left(\frac{4}{3}, \frac{5}{3}\right) \tag{3.87}$$

from which

$$p \leq \frac{(5 - 3\Gamma_{\rm th})(\Gamma_{\rm th} - 1)}{3\Gamma_{\rm th} - 4}\rho \qquad \text{with} \qquad \Gamma_{\rm th} \in \left(\frac{4}{3}, \frac{5}{3}\right) \tag{3.88}$$

3.4 Closures for Maxwell equations

To close the system in the magnetized case we need a way to derive the electric field. The most used closure is given by the so-called *Ideal MHD* (IMHD) (e.g., Duez et al. 2005, Shibata and Sekiguchi 2005, Ciolfi et al. 2017, Ciolfi et al. 2019, Ciolfi 2020, Endrizzi et al. 2016, Giacomazzo et al. 2011a, Sur et al. 2022, Rezzolla et al. 2011 and Baiotti and Rezzolla 2017, where the authors reviewed the amount of work on the

post-merger phase available up to 2017, and references therein)[11]:

$$\mathbf{E} = -\mathbf{v} \times \mathbf{B} \tag{3.89}$$

This is a particular case of the *Resistive MHD* (RMHD) closure, given by the Ohm's law:

$$j^\mu = \sigma^{\mu\nu} e_\nu \tag{3.90}$$

where

$$\sigma^{\mu\nu} = \sigma\Big(g^{\mu\nu} + \xi^2 b^\mu b^\nu + \xi \epsilon^{\mu\nu\lambda\kappa} u_\lambda b_\kappa\Big) \tag{3.91}$$

is the electric conductivity tensor (Bekenstein and Oron 1978, Zanotti and Dumbser 2011). Parameters σ and ξ are related to the microphysics of the plasma via

$$\sigma = \frac{\sigma_0}{1 + (\xi B)^2} \qquad \sigma_0 = \frac{n_e e^2 \tau_c}{m_e} \tag{3.92}$$

$$\xi = \frac{e\tau_c}{m_e} \tag{3.93}$$

with n_e the electron density, e the electron's charge, m_e the electron's mass, and τ_c the collision time. In this work we consider the isotropic case, in which $\sigma = \sigma_0$ and

$$\sigma^{\mu\nu} = \sigma g^{\mu\nu} = \sigma_0 g^{\mu\nu} \tag{3.94}$$

therefore

$$j^\mu = \sigma e^\mu \tag{3.95}$$

The 3+1 split gives the following expression for the electric current (e.g., Bucciantini and Del Zanna 2012, Dionysopoulou et al. 2013, Del Zanna and Bucciantini 2018, Tomei et al. 2019, Franceschetti and Del Zanna 2020, Del Zanna et al. 2022):

$$\mathbf{J} = q\mathbf{v} + \sigma W[\mathbf{E} + \mathbf{v} \times \mathbf{B} - (\mathbf{E} \cdot \mathbf{v})\mathbf{v}] = q\mathbf{v} + \frac{W[\mathbf{E} + \mathbf{v} \times \mathbf{B} - (\mathbf{E} \cdot \mathbf{v})\mathbf{v}]}{\eta} \tag{3.96}$$

where $\eta = 1/\sigma$ is the *electrical resistivity*. The IMHD regime corresponds to the limit

$$\sigma \to \infty \Longrightarrow \eta \to 0 \tag{3.97}$$

and $e^\mu = 0$.

[11] A general discussion about general relativistic magnetohydrodynamics simulations and their applications to binary neutron star mergers can be found in https://doi.org/10.48550/arXiv.2405.10081.

3.5 Extracting gravitational waves

In an asymptotically flat spacetime, such as that expected in regions far from an astrophysical source of gravitational waves, the spacetime metric approaches the Minkowski metric as one moves away from the source. In such a scenario, to extract gravitational waves, it is convenient to introduce the *Newman-Penrose quantity* Ψ_4, which, at asymptotically large distances, is related to the metric perturbation $h_{\mu\nu}$ (introduced in Section 1.4.1) through the relation

$$\Psi_4 = \ddot{h}_+ - i\ddot{h}_\times \tag{3.98}$$

where i denotes the imaginary unit. From this, it follows that:

$$\ddot{h}_+ = \mathrm{Re}\{\Psi_4\} \qquad \text{and} \qquad \ddot{h}_\times = -\,\mathrm{Im}\{\Psi_4\} \tag{3.99}$$

Integrating twice in time yields the gravitational wave polarizations. During the integration, two constants of integration arise for each polarization. These constants correspond to:

- The initial conditions for h_+ and $h_\times$ (potential time shifts);
- The initial velocities of the polarizations (i.e., the first time derivatives of the polarizations at the initial moment).

In many cases, it is assumed that at a sufficiently large time interval far from the source, the gravitational wave behaves in such a way that these constants are zero (i.e., the gravitational wave is considered to be "switched off" at an earlier time).

In order to evaluate the quantity Ψ_4, it is useful to introduce the *Weyl tensor*

$$C_{\mu\nu\rho\sigma} = R_{\mu\nu\rho\sigma} - \frac{1}{2}(g_{\mu\rho}R_{\nu\sigma} - g_{\mu\sigma}R_{\nu\rho} + g_{\nu\sigma}R_{\mu\rho} - g_{\nu\rho}R_{\mu\sigma}) + \frac{R}{6}(g_{\mu\rho}g_{\nu\sigma} - g_{\mu\sigma}g_{\nu\rho}) \tag{3.100}$$

where $R_{\mu\nu\rho\sigma}$ is the Riemann tensor, $R_{\mu\nu}$ is the Ricci tensor, and R is the scalar curvature. The Weyl tensor has the same symmetries as the Riemann tensor. The Weyl tensor represents the "free curvature" of spacetime. It is the part of the Riemann tensor that remains after subtracting the influences of matter, as represented by the Ricci tensor. This means that the Weyl tensor is associated with gravitational effects that can be perceived even in the absence of matter. In an asymptotically flat spacetime, the Weyl tensor provides a description of the spacetime curvature far from sources of matter.

It is also useful to define the so-called *null tetrad*, a set of four null vectors (l^μ, q^μ, m^μ, $\bar{m}^\mu$) that form a local basis for spacetime. These vectors are characterized by being null vectors, which means that they satisfy the following conditions:

$$g_{\mu\nu}l^\mu l^\nu = g_{\mu\nu}q^\mu q^\nu = g_{\mu\nu}m^\mu m^\nu = g_{\mu\nu}\bar{m}^\mu \bar{m}^\nu \tag{3.101}$$

Furthermore,

$$g_{\mu\nu} m^\mu \bar{m}^\nu = 1 \qquad \text{and} \qquad g_{\mu\nu} l^\mu q^\nu = -1 \tag{3.102}$$

The four-vectors l^μ and q^μ are real and represent an outgoing null vector and an incoming null vector, respectively. In contrast, the four-vectors m^μ and $\bar{m}^\mu$ are complex (with $\bar{m}^\mu$ being the complex conjugate of m^μ) and represent spatial directions. The null tetrad can be chosen in various ways, depending on the geometry of spacetime and the present symmetries. Moreover, the tetrad can be modified through Lorentz transformations, thus allowing a great deal of flexibility in its definition.

The quantity Ψ_4 is defined as one of the five complex components of the Weyl tensor projected onto the null tetrad:

$$\Psi_4 = C_{\mu\nu\rho\sigma} q^\mu \bar{m}^\nu q^\rho \bar{m}^\sigma \tag{3.103}$$

Chapter 4

The MIR code

The equations presented in Chapter 3 cannot be solved analytically, but numerical methods are required. For this purpose, several codes have been developed to date, both public - such as `GRHydro` (Mösta et al. 2013), `IllinoisGRMHD` (Etienne et al. 2015), and `Spritz` (Cipolletta et al. 2020), `Athena++` (Cook et al. 2023), and `AsterX` (Kalinani et al. 2024) - and private - such as `ECHO` (Del Zanna et al. 2007), `GRaM-X` (Shankar et al. 2023), and the `SACRA` variant of Kiuchi et al. 2022. However, all these codes work in the ideal regime.

Numerically solving this system of highly nonlinear and strongly coupled partial differential equations represents a significant computational challenge, particularly when considering the resistive regime. Compared to the ideal regime, the presence of dissipative terms requires the use of different numerical schemes to guarantee stability and accuracy. For this purpose, we have developed a new numerical code, `MIR` (an acronym for "**M**agneto**I**drodinamica **R**esistiva", i.e., "resistive magnetohydrodynamics" in Italian), developed within the Einstein Toolkit framework (Löffler et al. 2012), a powerful freely accessible computational infrastructure which provides a collection of computational tools (called "thorns") for numerical simulation. Written in `Fortran90`, `MIR` is capable of solving the GRMHD equations in 3D Cartesian coordinates and on a dynamical spacetime using the 3+1 Eulerian formalism, in both the ideal and resistive regimes, filling a crucial gap in the toolkit's capabilities.

The initial sections of this chapter are dedicated to providing an overview of the various numerical methods employed (main reference: Press et al. 2007), while the later sections focus on their implementation and application within our code.

4.1 Definitions and structure of the code

The equations presented in Chapter 3 are written in the form

$$\partial_t \boldsymbol{\mathcal{U}} + \partial_i \boldsymbol{\mathcal{F}}^i = \boldsymbol{\mathcal{S}} \tag{4.1}$$

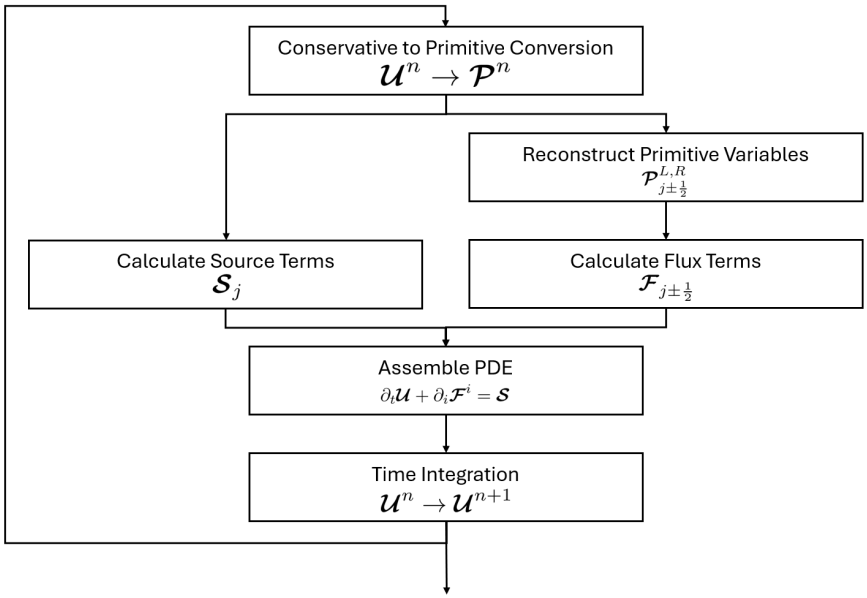

Figure 4.1: Typical structure of a code based on high-resolution schemes.

where $\boldsymbol{\mathcal{U}}$ is the vector of *evolved* variables, $\boldsymbol{\mathcal{F}}^i$ are the *flux* vectors, and $\boldsymbol{\mathcal{S}}$ is the *source* vector. An equation written in form (4.1) is said to be written in *conservative form*, because it explicitly expresses the conservation principle of the physical quantity $\boldsymbol{\mathcal{U}}$ within a control volume, accounting for the fluxes of this quantity through the surfaces of the volume and the sources within the volume itself. In fact, this form ensures that in the absence of sources $\boldsymbol{\mathcal{S}} = \mathbf{0}$) and in a closed system (without fluxes through the boundaries), the total amount of $\boldsymbol{\mathcal{U}}$ in the control volume remains constant over time. For this reason, evolved variables are sometimes called *conserved* or *conservative*.

Evolved variables, fluxes, and sources are built out of the so-called *primitive* variables $\boldsymbol{\mathcal{P}}$, i.e., those physical quantities that describe the local state of the system. In our case:

$$\boldsymbol{\mathcal{U}} = \sqrt{\gamma}\left[D, S_i, \mathcal{E}, B^i, E^i\right]^T \tag{4.2}$$

and

$$\boldsymbol{\mathcal{P}} = \left[\rho, \epsilon, p, v^i, B^i, E^i\right]^T \tag{4.3}$$

where the superscript ^{T} denotes the transposed vector. As we shall see later, the derivation of primitive variables from conservative ones is one of the challenges of numerics.

To solve the system of equations written in form (4.1), the `MIR` code operates on a discretized grid of the computational domain, dividing the space into cells. Each variable, defined at the cell center, is then reconstructed at each cell boundary using high-resolution shock capturing methods. his reconstruction is essential for capturing

spatial variations of the solution, especially in the presence of steep gradients or discontinuities. At this point, the code calculates the numerical fluxes at the cell interfaces via a Riemann solver. These fluxes represent the amount of a physical quantity crossing the interface within a given time interval. Flux calculation is crucial, as the exchange of information between cells is what enables the simulation of the system's evolution over time. Finally, once the numerical fluxes and source terms, the latter as a function of cell-centered variables, have been computed, the variable values are passed to the `MoL` (an acronym for "**M**ethod **o**f **L**ines") thorn, which uses them to advance the solution in time through a time integrator. Figure 4.1 illustrates the typical structure of a code based on high-resolution schemes, such as MIR.

In the following Sections 4.2 to 4.6, we describe the general operation of each numerical method used within the `MIR` code, before focusing on the presentation of the specific numerical schemes we have implemented.

4.2 Finite differences

To solve an equation written in form (4.1), so-called *grid-based methods* are used, which are based on discretizing the solution domain in a grid of discrete points and approximating the solution of the equation at each point on the grid. The first method we present is the so-called *finite difference method* (FDM), in which derivatives are replaced by finite incremental ratios, i.e.

$$\frac{\partial f}{\partial x} \approx \frac{\Delta f}{\Delta x} \tag{4.4}$$

The accuracy of these approximations depends on the grid spacing and the order of the method.

The *forward* FDM uses the point of interest and subsequent points to approximate the derivative, and the n-th derivative is given by

$$f^{(n)}(x) = \frac{1}{h^n} \sum_{i=0}^{n} (-1)^{n-i} \binom{n}{i} f(x + ih) \qquad \text{(forward)} \tag{4.5}$$

On the contrary, the *backward* FDM uses the point of interest and preceding points to approximate the derivative, and the n-th derivative is given by

$$f^{(n)}(x) = \frac{1}{h^n} \sum_{i=0}^{n} (-1)^{i} \binom{n}{i} f(x - ih) \qquad \text{(backward)} \tag{4.6}$$

Finally, a third commonly used method is the *central* FDM, which uses points both before and after the point of interest to approximate the derivative:

$$f^{(n)}(x) = \frac{1}{h^n} \sum_{i=0}^{n} (-1)^{i} \binom{n}{i} f\left(x - \left(\frac{n}{2} - i\right)h\right) \qquad \text{(central)} \tag{4.7}$$

The order of accuracy is $\mathcal{O}(h)$ for forward and backward differences, and $\mathcal{O}\left(h^2\right)$ for central differences. Higher-order differences can also be used to construct better approximations. However, these use a larger number of points to compute the derivative, thus requiring the function to be smooth over a wider range. For example, the second-order central differences for the first derivative is given by

$$f'(x) = \frac{f(x+h) - f(x-h)}{h} + \mathcal{O}\left(h^2\right) \tag{4.8}$$

while the fourth order is given by

$$f'(x) = \frac{f(x-2h) - 8f(x-h) + 8f(x+h) - f(x+2h)}{12h} + \mathcal{O}\left(h^4\right) \tag{4.9}$$

Simple and easy to implement, FDMs require the derived function to be sufficiently smooth within the domain of interest. This implies difficulties in treating problems with discontinuities or strong gradients. It is, therefore, convenient to reconstruct the function at cell faces $x_{j\pm\frac{1}{2}}$ using one of the methods described in Section 4.3 below and compute the derivative using the second-order central differences:

$$f'(x_j) = \frac{f\left(x_{j+\frac{1}{2}}\right) - f\left(x_{j-\frac{1}{2}}\right)}{h_j} \tag{4.10}$$

4.3 Reconstruction and high-resolution shock capturing methods

To estimate the value of a function at the cell faces of the numerical grid, we need to "reconstruct" the function at those points. Reconstruction consists in finding a new function, often simpler or with desired properties, that approximates the original one.

To evaluate the quality of a reconstruction, it is essential to consider several aspects that measure the accuracy, stability, and efficiency of the method used. A fundamental parameter in this evaluation is the *reconstruction error*, which represents the discrepancy between the reconstructed values and the exact values of the function. This error can be measured in different ways, including absolute error, which corresponds to the difference between the reconstructed and exact values at a specific point, and relative error, which expresses this difference as a fraction of the exact value.

An important criterion for evaluating the quality of the reconstruction is the *smoothness* or *regularity* of the reconstructed function. This aspect refers to the continuity of the function and its derivatives, as a well-reconstructed function should be free of unwanted oscillations. Analyzing the derivatives of the reconstructed function is useful for identifying any discontinuities or irregularities, which indicate low reconstruction quality. In certain numerical contexts, especially with high-order interpolation methods, spurious oscillations may occur, which degrade the reconstruction quality.

In many cases, the reconstruction must also preserve certain physical properties of the original function. For example, it may be crucial that the method conserves the

integral of the function, representing quantities such as mass or energy. Similarly, the method should respect the monotonicity of the function, avoiding the introduction of new maxima or minima that were not present in the original function.

Another essential parameter in evaluating the quality of reconstruction is the *order of accuracy* of the method, which describes how quickly the error decreases as the grid resolution increases. A method of order p has an error that decreases proportionally to h^p, where h is the grid spacing. Verifying that the error decreases consistently with the predicted theoretical order is a clear indicator of the reconstruction quality. This property is particularly important for high-accuracy methods used in solving partial differential equations, as it ensures the precision of the results.

In contexts where discontinuities are present, such as in hyperbolic equations or problems involving shock waves, it is crucial that the reconstruction is robust and does not introduce spurious oscillations near these discontinuities.

Alongside accuracy, an equally important aspect is *computational efficiency*. In practice, it is often necessary to strike a balance between the precision of the reconstruction and the associated computational cost. A more complex and precise method can involve a higher computational cost, which is not always justified in terms of performance improvement compared to a simpler method.

Reconstruction methods are a key component of *high-resolution shock capturing* methods, a class of numerical techniques designed to capture discontinuities with the highest possible accuracy, while avoiding the occurrence of spurious numerical oscillations that could compromise the quality of the solution. There are several methods in the literature. In our code, we decided to implement two methods: the TVD and the WENO-Z method.

4.3.1 Total Variation Diminishing (TVD) methods

Total Variation Diminishing (TVD) methods (Harten 1983, Toro 2009) are numerical techniques that guarantee the total variation (TV)

$$TV(f) = \sum_i |f_{i+1} - f_i| \tag{4.11}$$

of the numerical solution does not increase over time, preventing the formation of non-physical oscillations and preserving the monotonicity of the exact solution. In other words, a TVD scheme satisfies the inequality

$$TV\left(f^{n+1}\right) \leq TV(f^n) \tag{4.12}$$

where f^n and f^{n+1} denote the approximate solutions at time steps t_n and t_{n+1}, respectively.

A common approach to achieving the TVD property is through the use of *flux limiters*, which adapt the scheme's behavior based on the local smoothness of the solution.

Flux limiters are functions designed to control the slope of the numerical solution near discontinuities. These limiters reduce the steepness of the solution in regions where discontinuities or sharp gradients occur, thereby preventing unwanted oscillations.

A typical flux-limited form of the flux is

$$\boldsymbol{\mathcal{F}}_{i+\frac{1}{2}} = \boldsymbol{\mathcal{F}}^{\text{low}}_{i+\frac{1}{2}} + \phi(r_i)\left(\boldsymbol{\mathcal{F}}^{\text{high}}_{i+\frac{1}{2}} - \boldsymbol{\mathcal{F}}^{\text{low}}_{i+\frac{1}{2}}\right) \tag{4.13}$$

where $\boldsymbol{\mathcal{F}}_{i+\frac{1}{2}} = \boldsymbol{\mathcal{F}}\left(f_{i+\frac{1}{2}}\right)$ represent edge flux for the i-th cell, $\boldsymbol{\mathcal{F}}^{\text{low}}$ is the flux computed using a low order scheme, $\boldsymbol{\mathcal{F}}^{\text{high}}$ is the flux computed using a high order scheme, $\phi(r_i)$ is the flux limiter, and the parameter

$$r_i = \frac{f_i - f_{i-1}}{f_{i+1} - f_i} \tag{4.14}$$

measures the regularity of the solution in neighboring cells. In this way, the flux limiter determines how much of the high-order scheme should be used relative to the low-order scheme: in smooth regions (i.e., $r_i \approx 1$), the limiter allows the high-order scheme to be fully utilized, while near discontinuities or steep gradients (i.e., when r_i is very large or small), the limiter reduces the contribution of the high-order scheme, favoring the more diffusive and stable low-order scheme. In `MIR`, we implemented the following two limiters:

- *minmod* limiter:

$$\phi(r) = \max\{0, \min\{1, r\}\} \qquad \lim_{r\to\infty} \phi(r) = 1 \tag{4.15}$$

- *monotonized central* (MC) limiter:

$$\phi(r) = \max\left\{0, \min\left\{2r, \frac{1+r}{2}, 2\right\}\right\} \qquad \lim_{r\to\infty} \phi(r) = 2 \tag{4.16}$$

The minmod limiter is quite aggressive in limiting the slope to avoid oscillations, but it may also significantly reduce accuracy in smooth regions, while the MC limiter strikes a balance between accuracy and monotonicity.

4.3.2 The WENO-z method

A *WENO* (Weighted Essentially Non-Oscillatory) method is a high-resolution numerical scheme that, through a weighted combination of different stencils (groups of points used to approximate spatial derivatives), aims to maintain accuracy in smooth regions and avoid oscillations near discontinuities. The formula to compute the flux is

$$\boldsymbol{\mathcal{F}}_{i+\frac{1}{2}} = \sum_{k=0}^{r} \omega_k \boldsymbol{\mathcal{F}}^k_{i+\frac{1}{2}} \tag{4.17}$$

where r is the number of stencils used, $\boldsymbol{\mathcal{F}}^k_{i+\frac{1}{2}}$ is the flux computed using the k-th stencil, and ω_k is the weight associated with the k-th stencil.

However, the classical WENO scheme suffers from a loss of accuracy in smooth regions, where the approximations computed using the different stencils should yield very similar results. This occurs because the weights are not optimally tuned, reducing the overall accuracy of the method. The *WENO-Z* scheme (Borges et al. 2008) was introduced to address this limitation. The key difference from the classical WENO scheme is the introduction of a correction term τ_5 in the formula for computing the nonlinear weights. This correction factor represents a global measure of the smoothness of the high-order polynomial constructed using all possible stencils. The formula for the weights in the WENO-Z scheme is given by

$$\omega_k = \frac{\alpha_k}{\sum_{j=0}^{r} \alpha_j} \qquad \text{where} \qquad \alpha_k = d_k \left(1 + \frac{\tau_5}{\beta_k + \epsilon}\right) \tag{4.18}$$

with d_k the linear weights associated with each stencil, β_k the smoothness indicator of each stencil, and ϵ a very small positive value used to avoid division by zero.

In smooth regions, τ_5 reduces the influence of the nonlinear weights, thus maintaining optimal accuracy, while in regions with discontinuities, it has no significant effect, preserving the essential non-oscillatory properties of the method.

4.4 Riemann solvers

Once the fluxes on the right and left sides of each cell interface have been reconstructed, it is necessary to compute the flux that crosses it. This is computed using a so-called *Riemann solver*. Given a left and right state of the cell interface, the Riemann solver computes the resulting flux using different techniques, depending on the required level of accuracy and complexity.

There are different types of Riemann solvers. *Exact solvers* offer a precise solution but are often computationally expensive. Alternatively, *approximate solvers* are commonly used, which allow for a significant reduction in computational costs while maintaining good accuracy.

To compute the numerical flux across the cell interface, a Riemann solver requires the computation of characteristic waves, which describe how discontinuities or perturbations propagate through the fluid. The resulting flux depends on the direction in which the waves propagate, their velocity, and the amplitude of the variations associated with each wave.

The first solver implemented in `MIR` is the *Harten-Lax-van-Leer-Einfeldt* (HLLE) *solver* (Harten et al. 1983), where, for each component i and each direction j,

$$\boldsymbol{\mathcal{F}}^i_j = \frac{a^j_+ \boldsymbol{\mathcal{F}}^i_{L,j} + a^j_- \boldsymbol{\mathcal{F}}^i_{R,j} - a^j_+ a^j_- \left(\boldsymbol{\mathcal{U}}^i_{R,j} - \boldsymbol{\mathcal{U}}^i_{L,j}\right)}{a^j_+ + a^j_-} \tag{4.19}$$

where the subscript $_R$ ($_L$) means that the quantity is computed at the right (left) side of the cell interface and (Del Zanna et al. 2007)

$$a^j_{\pm} = \max\left\{0, \pm\lambda^j_{\pm,L}, \pm\lambda^j_{\pm,R}\right\} \tag{4.20}$$

and $\lambda_{\pm}$ are the characteristic speeds.

The HLLE solver demonstrates good numerical stability, effectively mitigating the risk of spurious oscillations that can occur near shock waves. This stability is crucial for ensuring reliable results in regions with high gradients, where the behavior of the flow can be unpredictable. Furthermore, it exhibits robust performance across a wide range of compressible flow scenarios, effectively handling discontinuities and shock waves, which are common in fluid dynamics applications. Another significant advantage of the HLLE solver is its favorable cost-accuracy trade-off. It provides an acceptable balance between computational efficiency and the accuracy of results, enabling the simulation of large-scale problems without compromising the integrity of the findings.

The second solver implemented in our code is the Lax–Friedrichs (LF) solver (Toro 2009):

$$\boldsymbol{\mathcal{F}}^i_j = \frac{\boldsymbol{\mathcal{F}}^i_{L,j} + \boldsymbol{\mathcal{F}}^i_{R,j} - c(\boldsymbol{\mathcal{U}}^i_{R,j} - \boldsymbol{\mathcal{U}}^i_{L,j})}{2} \tag{4.21}$$

where $c = \max\left\{a^j_+, a^j_-\right\}$. The LF solver is highly diffusive, which means it introduces a certain degree of smoothing in the solutions. This characteristic makes it useful in cases of strong jumps in pressure, as the numerical diffusion helps stabilize the solution and prevent spurious oscillations around discontinuities. However, it is important to note that while this smoothing can improve stability, it may also reduce accuracy in capturing very fine features of the flow.

To compute the characteristic speeds $\lambda_{\pm}$ we follow the approach presented in Gammie et al. 2003, where

$$\lambda^i_{\pm} = \alpha\bar{\lambda}^i_{\pm} - \beta^i \tag{4.22}$$

with

$$\bar{\lambda}^i_{\pm} = \frac{(1-a^2)v^i \pm \sqrt{a^2(1-v^2)\left[(1-v^2a^2)\gamma^{ii} - (1-a^2)(v^i)^2\right]}}{1-v^2a^2} \tag{4.23}$$

In the hydro (i.e., in the absence of electromagnetic fields) and IMHD regimes, we set (Gammie et al. 2003, Del Zanna et al. 2007)

$$a^2 = c_s^2 + c_a^2 - c_s^2 c_a^2 \tag{4.24}$$

- with c_s the sound speed and c_a the Alfvén speed

$$c_a^2 = \frac{b^2}{\rho h + b^2} = \frac{B^2 - E^2}{\rho h + B^2 - E^2} \tag{4.25}$$

- while in the resistive regime we assume $a^2 = 1$ as in Del Zanna et al. 2007 and Bucciantini and Del Zanna 2012, so

$$\lambda^i_\pm = \pm\alpha\sqrt{\gamma^{ii}} - \beta^i \qquad \text{(resistive regime)} \tag{4.26}$$

4.5 Time integrators

Time integrators are numerical methods used to approximate the solutions of ordinary differential equations (ODEs) and partial differential equations (PDEs), i.e. equations of the form

$$\frac{\mathrm{d}y}{\mathrm{d}t} = f(t, y) \tag{4.27}$$

These methods are essential for approximating the solution of differential problems when an exact analytical solution is difficult or impossible to find. Time integrators work by stepping through time and providing discrete solutions at specific time intervals for time-varying equations. They are divided into explicit and implicit methods. The choice between these types of methods has significant implications for stability, accuracy, and computational cost.

In *explicit methods*, the solution at the next time step depends only on information from the current or previous time steps. In other words, given an equation of the form (4.27), an explicit method computes the next value y_{n+1} as

$$y_{n+1} = y_n + \Delta t \cdot f(t_n, y_n) \tag{4.28}$$

Since there are no equations to solve at each time step, these methods are computationally efficient and easy to implement. They can also be *conditionally stable*, meaning they are only stable if the time step Δt is sufficiently small. For certain problems, particularly stiff equations, the required time step may be prohibitively small, making these methods inefficient or impractical.

In *implicit methods*, the solution at the next time step depends not only on the current state but also on the unknown future state. This creates an implicit equation that must be solved at each time step, usually through iteration or by solving a system of equations. In other words, given an equation of the form (4.27), an implicit method computes the next value y_{n+1} as

$$y_{n+1} = y_n + \Delta t \cdot f(t_{n+1}, y_{n+1}) \tag{4.29}$$

This equation is called "implicit" because y_{n+1} appears on both sides, and solving it often requires a root-finding algorithm (see Section 4.6 below). These methods are generally *unconditionally stable*, meaning they can handle much larger time steps without becoming unstable, even for stiff systems. This makes them the preferred choice for stiff problems.

Since implicit methods cannot always be applied to every type of differential operator, it is sometimes advisable to rewrite the differential operator as the sum the

differential operators, where one is handled explicitly and the other implicitly. Usually, the implicit term is chosen to be linear, while the explicit term can be nonlinear. This combination is called *IMEX* (**IM**plicit-**EX**plicit) *method*.

4.5.1 IMEX Runge-Kutta methods

Among the most widespread iterative methods for numerically solving initial value problems for ordinary differential equations, Runge-Kutta (RK) methods stand out, providing a solid foundation for accurate approximations. They are popular for their ability to achieve high accuracy without requiring higher-order derivatives, making them more efficient and easier to implement compared to other methods.

The core idea behind Runge-Kutta methods is to approximate the solution of an ODE over a small interval by taking a weighted average of several slopes calculated at different points within that interval. This weighted average is then used to advance the solution to the next time step. Here we describe how the IMEX Runge-Kutta (IMEX-RK) scheme (Pareschi and Russo 2005, Palenzuela et al. 2009) works, following the prescription presented in Tomei et al. 2019, itself based on Bucciantini and Del Zanna 2012 and Del Zanna and Bucciantini 2018. The usual explicit method can be easily obtained by setting the implicit terms to zero.

Conserved variables can be split as $\boldsymbol{\mathcal{U}} = \{\boldsymbol{\mathcal{X}}, \boldsymbol{\mathcal{Y}}\}$, where $\boldsymbol{\mathcal{X}}$ is the set of conserved variables with stiff source terms and $\boldsymbol{\mathcal{Y}}$ refers to the remaining ones. It is then convenient to rewrite system (4.1) as

$$\partial_t \boldsymbol{\mathcal{X}} = \boldsymbol{\mathcal{Q}}_{\boldsymbol{\mathcal{X}}}[\boldsymbol{\mathcal{U}}] + \boldsymbol{\mathcal{R}}_{\boldsymbol{\mathcal{X}}}[\boldsymbol{\mathcal{U}}] \qquad \partial_t \boldsymbol{\mathcal{Y}} = \boldsymbol{\mathcal{Q}}_{\boldsymbol{\mathcal{Y}}}[\boldsymbol{\mathcal{U}}] \tag{4.30}$$

with $\boldsymbol{\mathcal{Q}}$ the right-hand side (RHS) without stiff terms (including flux derivatives) and $\mathbb{R}$ the RHS containing the stiff terms. Let Δt be the time interval in which the conserved variables is updated from $\boldsymbol{\mathcal{U}}^n$ to $\boldsymbol{\mathcal{U}}^{n+1}$. The IMEX-RK scheme consists in the following steps:

- First, for each step $i = 1, 2, \ldots, s$ (with s the number of IMEX-RK substeps) we have

$$\boldsymbol{\mathcal{X}}_*^{(i)} = \boldsymbol{\mathcal{X}}^n + \Delta t \sum_{j=1}^{i-1} \tilde{a}_{ij} \boldsymbol{\mathcal{Q}}_{\boldsymbol{\mathcal{X}}} \left[\boldsymbol{\mathcal{U}}^{(j)}\right] + \Delta t \sum_{j=1}^{i-1} a_{ij} \boldsymbol{\mathcal{R}}_{\boldsymbol{\mathcal{X}}} \left[\boldsymbol{\mathcal{U}}^{(j)}\right] \tag{4.31}$$

  and

$$\boldsymbol{\mathcal{Y}}_*^{(i)} = \boldsymbol{\mathcal{Y}}^n + \Delta t \sum_{j=1}^{i-1} \tilde{a}_{ij} \boldsymbol{\mathcal{Q}}_{\boldsymbol{\mathcal{Y}}} \left[\boldsymbol{\mathcal{U}}^{(j)}\right] \tag{4.32}$$

  where $\tilde{a}_{ij}$ and a_{ij} are lower triangular matrices with dimensions $s \times s$.

- Second, for $j = i$ variables $\boldsymbol{\mathcal{X}}_*^{(i)}$ undergo an extra *implicit* evolution with $\tilde{a}_{ii} = 0$ and $a_{ii} \neq 0$:

$$\boldsymbol{\mathcal{X}}^{(i)} = \boldsymbol{\mathcal{X}}_*^{(i)} + a_{ij} \Delta t \boldsymbol{\mathcal{R}}_{\boldsymbol{\mathcal{X}}} \left[\boldsymbol{\mathcal{X}}^{(i)}, \boldsymbol{\mathcal{Y}}_*^{(i)}\right] \qquad \boldsymbol{\mathcal{Y}}^{(i)} = \boldsymbol{\mathcal{Y}}_*^{(i)} \tag{4.33}$$

Notice that for $i = 1$ only the implicit step is needed.

- Finally, the conserved variables are updated as

$$\boldsymbol{\mathcal{U}}^{n+1} = \boldsymbol{\mathcal{U}}^{n} + \Delta t \sum_{i=1}^{s} \left[\tilde{b}_i \boldsymbol{\mathcal{Q}}\left[\boldsymbol{\mathcal{U}}^{(i)}\right] + b_i \boldsymbol{\mathcal{R}}\left[\boldsymbol{\mathcal{U}}^{(i)}\right] \right] \tag{4.34}$$

  where $\tilde{b}_i$ and b_i are additional coefficients required by the scheme.

In Appendix A we describe our implementation of the SSP2(2,2,2) scheme (i.e. an IMEX extension of the second-order RK (RK2) scheme) presented in Pareschi and Russo 2005 and Palenzuela et al. 2009 in the `MoL` thorn.

4.6 Root-finding algorithms

A root-finding algorithm is a computational method used to determine the zeros (or "roots") of a function, i.e. the values of x such that $f(x) = 0$. Root-finding algorithms work iteratively, progressively refining the estimate of the root with each step. As the iterations proceed, the approximation becomes more accurate, continuing until a specified level of precision is achieved. Typically, these algorithms assume the function is continuous within a certain interval or that specific conditions are satisfied to ensure convergence toward the root. Nevertheless, the rate at which they converge and their reliability can differ depending on the method used. Additionally, most algorithms rely on either an initial guess or an initial interval to begin the search. The selection of this starting point or interval can impact both the likelihood of success and the speed of convergence. As a result, there is a balance to be struck between how quickly an algorithm converges on a root and how consistently it can do so across different scenarios. In this section, we briefly describe the functioning of the two algorithms that were implemented in our code.

4.6.1 Bisection method

One of the simplest and most intuitive algorithms used is the *bisection* method. It is based on the *intermediate value theorem*, which states that if a continuous function changes sign over an interval $[a, b]$ (i.e., $f(a) \cdot f(b) < 0$), then there is at least one root within that interval. Thus, the method always guarantees convergence to a root, as long as the function is continuous and the initial interval contains a root. However, if the function has multiple roots in the initial interval, the method will find only one. Additionally, the method is simple to implement and does not require the derivative of the function. However, it has linear convergence, which means that the number of correct digits increases slowly compared to other methods. Bisection method works as follow:

1) Given an initial interval $[a, b]$ such that $f(a) \cdot f(b) < 0$, calculate the midpoint $m = (a + b)/2$.

2) Evaluate the faction at the midpoint.

- If $f(m) = 0$, m is the root we are looking for and the algorithm terminates.
- If $f(m) \neq 0$ and $f(a) \cdot f(m) < 0$, the root lies in the interval $[a, m]$, so we set $b = m$ and return to step 1.
- If $f(m) \neq 0$ and $f(a) \cdot f(m) > 0$, the root lies in the interval $[m, b]$, so we set $a = m$ and return to step 1.

This process is repeated iteratively, until the length of the interval becomes sufficiently small or until the absolute value of $f(m)$ becomes less than a predefined tolerance.

4.6.2 Newton-Raphson method

Another widely used method is the *Newton-Raphson* (NR) method. The basic idea of the NR method is to use the tangent to the curve of the function to approximate the root. Starting from an initial point x_0, the method iteratively refines the approximation using the derivative of the function, following the formula

$$x_{n+1} = x_n - \frac{f(x_n)}{f'(x_n)} \tag{4.35}$$

where $f'(x_n)$ is the first derivative of the function evaluated at x_n. The calculation is repeated until the value of x_n is sufficiently close to the root. The algorithm stops when $|x_{n+1} - x_n|$ is smaller than a predefined tolerance or when the value of $f(x_n)$ is close to zero.

If the initial guess x_0 is sufficiently close to the root, the NR method exhibits quadratic convergence, which means that the number of correct digits in the approximation increases exponentially with each iteration. As a result, the method often needs significantly fewer iterations to reach an accurate solution. However, if the initial guess is too distant from the root or if the function behaves problematically (e.g., a zero or changing derivative), the method may fail to converge or might converge to a different root.

The NR method can be naturally extended to the multidimensional case, that is, to solve systems of nonlinear equations. In this case, instead of dealing with a single function, we work with a vector of functions $\mathbf{f}(\mathbf{x})$, where $\mathbf{x}$ is a vector of variables. n this context, the most direct generalization involves replacing the first derivative with the inverse of the Jacobian matrix

$$\mathbf{J}_{ij}(\mathbf{x}) = \frac{\partial f_i}{\partial x_j} \tag{4.36}$$

The iterative formula of the multidimensional NR method becomes

$$\mathbf{x}_{n+1} = \mathbf{x}_n - \mathbf{J}^{-1}(\mathbf{x}_n) \cdot \mathbf{f}(\mathbf{x}_n) \tag{4.37}$$

The calculation of the Jacobian matrix and its inverse at each iteration can be computationally expensive.

4.7 The Conservative-to-Primitive (C2P) scheme

One of the challenges in numerical methods is the recovery of primitive variables from conserved ones. This is due to several factors, including the non-linearity of the relations, the possible presence of unstable, unphysical, or multiple solutions, and the potential dependence on the imposed initial conditions, which may affect the convergence of the iterative methods used to solve the problem. To this end, many schemes have been proposed to date. Many of them use the Newton-Raphson method (e.g. Del Zanna et al. 2007, Dionysopoulou et al. 2013, Mösta et al. 2013). However, the requirement to compute pressure derivatives means that this algorithm works well with analytical equations of state, but it can return inaccurate results with tabulated equations of state. For this reason, in hydro and IMHD regimes, algorithms based on the bisection method have also been used (e.g., Galeazzi et al. 2013, Kastaun et al. 2021), which, as we have seen earlier, do not require any derivative computation. However, the implicit step required in the resistive case greatly complicates matters. For this reason, until now, the algorithms proposed in this regime have relied on 3D Newton-Raphson (e.g., Tomei et al. 2019, Mattia et al. 2023). In this section, we describe the scheme implemented in our code `MIR`, which, by combining the bisection method with the 3D Newton-Raphson method, extends the scheme proposed by Kastaun et al. 2021. The reasons that motivated us to develop a new scheme, rather than using one of those already available in the literature, will be discussed later at the end of this section, specifically in Section 4.7.8.

After each `MoL` step, we have available the values of the following fluid variables:

$$D \qquad \mathbf{S} \qquad \mathcal{E} \tag{4.38}$$

and, in the magnetized case, the following electromagnetic variables:

$$\mathbf{B} \qquad \mathbf{E}_* \tag{4.39}$$

Here, $\mathbf{E}_*$ is the value of the electric field that must undergo the implicit step, and is therefore available only in the resistive case. From the values of these conservative variables, we need to derive the primitive variables. Since the number of variables available to us is insufficient, we must use an equation of state to derive the pressure.

4.7.1 Definitions

Firstly, it is useful to define the following variable

$$\mu = \frac{1}{Wh} \tag{4.40}$$

- with W the Lorentz factor and h the specific enthalpy -, the following renormalized quantities

$$\mathbf{r} = \frac{\mathbf{S}}{D} \tag{4.41}$$

$$\bar{r}(\mu) = \frac{M(\mu)}{D} \qquad M(\mu) = \|\mathbf{M}(\mu)\| \tag{4.42}$$

$$\bar{q}(\mu) = \frac{\mathcal{E}_F(\mu)}{D} \tag{4.43}$$

and the modified velocity

$$\tilde{u}(\mu) = \sqrt{W^2(\mu) - 1} \tag{4.44}$$

In the resistive case, it is also helpful to introduce the following renormalized vectors

$$\mathbf{b} = \frac{\mathbf{B}}{\sqrt{D}} \qquad \mathbf{e} = \frac{\mathbf{E}}{\sqrt{D}} \qquad \mathbf{e}_* = \frac{\mathbf{E}_*}{\sqrt{D}} \tag{4.45}$$

and the following coefficients for the computation of the electric field:

$$A_0 = \frac{\tilde{\eta}}{\tilde{\eta} + W} = 1 - A_1 \tag{4.46}$$

$$A_1 = \frac{W}{\tilde{\eta} + W} = \frac{1}{1 + y} \tag{4.47}$$

$$A_2 = \frac{W^2 \tilde{\eta}}{(1 + W\tilde{\eta})(\tilde{\eta} + W)} = A_1 \left(1 - \frac{1}{1 + z}\right) \tag{4.48}$$

where

$$\tilde{\eta} = \frac{\eta/\alpha}{a_{ii}\Delta t} \qquad y = \frac{\tilde{\eta}}{W} \qquad z = W\tilde{\eta} \tag{4.49}$$

with a_{ii} the coefficient for the implicit step of the IMEX-RK scheme, Δt the time step, η the electrical resistivity, and α the lapse function.

We recall that the fluid variables are related to the conserved variables and the electromagnetic fields through the following relations:

$$\mathbf{M}(\mu) = \begin{cases} \mathbf{S} & \text{hydro case} \\ \mathbf{S} - \mathbf{E}(\mu) \times \mathbf{B} & \text{otherwise} \end{cases} \tag{4.50}$$

$$\mathcal{E}_F(\mu) = \begin{cases} \mathcal{E} & \text{hydro case} \\ \mathcal{E} - \dfrac{B^2 + E^2(\mu)}{2} & \text{otherwise} \end{cases} \tag{4.51}$$

Note that the electric field also depends on the variable μ. In fact, as mentioned earlier, the electric field is not known after the `MoL` step, even in the resistive case, as it is subject to the implicit step.

Variable μ plays a central role in the bisection algorithm, and it is not difficult to prove that

$$0 < \mu \leq \frac{1}{h_0} \tag{4.52}$$

where h_0 is the lower bound for the specific enthalpy, which depends on the chosen EoS.

4.7.2 Upper limits

Before proceeding with the execution of the C2P scheme, it is essential to calculate the following upper limits. These limits are necessary to ensure both the convergence of the numerical scheme and the compliance with physical constraints.

The first bound is the maximum of the conserved momentum **S**:

$$S^2_{\max} = \left(\mathcal{E} + B\sqrt{2\mathcal{E}}\right)^2 \tag{4.53}$$

The second bound is the maximum of the fluid momentum **M**:

$$M_{\max} = \begin{cases} M^{(res)}_{\max} & \text{resistive case} \\ S & \text{otherwise} \end{cases} \tag{4.54}$$

where

$$M^{(res)}_{\max} = A_{0,\max} E_* B + \sqrt{A^2_{0,\max} E^2_* B^2 + S^2} \tag{4.55}$$

with

$$A_{0,\max} = \frac{\tilde{\eta}}{\tilde{\eta}+1} = 1 - \frac{1}{1+\tilde{\eta}} \tag{4.56}$$

the maximum of coefficient A_0. Detailed calculations for the derivation of these two upper limits can be found in Appendix B.

The third bound is the maximum of the fluid velocity:

$$v_{\max} = \min\left\{v_{\max,1}, v_{\max,2}\right\} \tag{4.57}$$

where

$$v_{\max,1} = \frac{\tilde{u}_{\max}}{\sqrt{1+\tilde{u}^2_{\max}}} \qquad v_{\max,2} = \sqrt{1 - \frac{1}{W^2_{\max}}} \tag{4.58}$$

with $W_{\max}$ the maximum allowed value for the Lorentz factor (a free parameter, typically set to 2000), and

$$\tilde{u}_{\max} = \frac{\bar{r}_{\max}}{h_0} \qquad \bar{r}_{\max} = \frac{M_{\max}}{D} \tag{4.59}$$

This limit is necessary to prevent the fluid velocity from exceeding the speed of light.

4.7.3 The scheme

The purpose of the scheme is to determine the value of μ for which the function

$$f(\mu) = \mu - \frac{1}{\dfrac{h(\mu)}{W(\mu)} + W(\mu)\bar{r}^2(\mu)} \tag{4.60}$$

equals zero in the interval $\left(0, h_0^{-1}\right]$ using the bisection method. This is achieved through the following steps:

1) Following the prescription described in Section 4.7.4 below, compute the electric field $\mathbf{E}(\mu)$ in the magnetized case.

2) For the magnetized case, isolate the fluid variables $\mathbf{M}(\mu)$ and $\mathcal{E}_F$ by removing the electromagnetic contributions from the conserved quantities.

3) Derive the hydro primitive variables

$$\rho(\mu) = \max\{\rho_{\min}, \min\{\hat{\rho}(\mu), \rho_{\max}\}\} \qquad \hat{\rho}(\mu) = \frac{D}{W(\mu)} \tag{4.61}$$

$$\epsilon(\mu) = \max\{\epsilon_{\min}, \min\{\hat{\epsilon}(\mu), \epsilon_{\max}\}\} \qquad \hat{\epsilon}(\mu) = W(\mu)\bar{q}(\mu) - \bar{r}(\mu)\tilde{u}(\mu) - 1 \tag{4.62}$$

$$p(\mu) = p(\rho(\mu), \epsilon(\mu)) \tag{4.63}$$

$$v(\mu) = \min\{\mu\bar{r}(\mu), v_{\max}\} \tag{4.64}$$

Here, $\rho_{\min}$ ($\rho_{\max}$) and $\epsilon_{\min}$ ($\epsilon_{\max}$) represent the lower (upper) limits for the density and internal energy, respectively, both of which depend on the chosen EoS.

4) Evaluate the specific enthalpy

$$h(\mu) = 1 + \epsilon(\mu) + \frac{p(\mu)}{\rho(\mu)} \tag{4.65}$$

After determining the zero of Equation (4.60) and the associated primitive variables $[\rho, \epsilon, p]$, we can compute the fluid velocity as

$$\mathbf{v} = \frac{\mathbf{M}}{\rho h W^2} \tag{4.66}$$

4.7.4 Electric field

To compute the electric field in step 1, the fluid velocity is needed. However, this quantity is not yet known at this point. Nevertheless, it can be expressed as a function of the parameter μ and the electric field by inverting the expression for the conserved momentum:

$$\mathbf{v} = \mu(\mathbf{r} - \mathbf{e} \times \mathbf{b}) \tag{4.67}$$

This expression can be substituted into the electric field equation, thereby eliminating the dependence on velocity. In the IMHD regime, this yields the expression

$$\mathbf{E} = -\mu x \mathbf{r} \times \mathbf{B} \qquad x = \frac{1}{1 + \mu b^2} \qquad b^2 = \mathbf{b} \cdot \mathbf{b} \tag{4.68}$$

In the resistive case, the electric field undergoes the implicit step

$$\mathbf{E} = \mathbf{E}_* - \frac{W[\mathbf{E} + \mathbf{v} \times \mathbf{B} - (\mathbf{v} \cdot \mathbf{E})\mathbf{v}]}{\tilde{\eta}} \tag{4.69}$$

which can be rewritten as

$$\mathbf{E} = A_0\mathbf{E}_* - A_1\mathbf{v}\times\mathbf{B} + A_1(\mathbf{v}\cdot\mathbf{E})\mathbf{v} \tag{4.70}$$

where, as a reminder, the coefficients A_i are themselves functions of the velocity, and therefore of the electric field. A 3D root-finding algorithm is thus necessary to solve the equation. Therefore, we define the function

$$f_i\left(e^j\right) = A_0 e_{*,i} - A_1\epsilon_{ilm}v^l b^m + \mu A_1\Big(r_k e^k\Big)v_i - e_i \tag{4.71}$$

The Jacobian matrix is

$$\begin{aligned} J_{ij} = \frac{\partial f_i}{\partial e^j} = \frac{\partial A_1}{\partial e^j}\Big[\mu\Big(r_k e^k\Big)v_i - e_{*,i} - \epsilon_{ilm}v^l b^m\Big] \\ + A_1\mu\Big[v_i r_j + \Big(r_k e^k\Big)\frac{\partial v_i}{\partial e^j} + b_i b_j - \gamma_{ij}b^2\Big] - \gamma_{ij} \end{aligned} \tag{4.72}$$

where

$$\frac{\partial A_1}{\partial e^j} = \frac{\partial A_1}{\partial W}\frac{\partial W}{\partial e^j} = \frac{A_0}{\tilde{\eta}+W}\frac{\partial W}{\partial e^j} \tag{4.73}$$

$$\frac{\partial W}{\partial e^j} = \mu W^3\epsilon_{jlm}v^l b^m \tag{4.74}$$

and

$$\frac{\partial v_i}{\partial e^j} = -\mu\epsilon_{ijm}b^m \tag{4.75}$$

Note that, since the value of μ is given by the bisection step, the pressure derivatives do not appear.

Once all fluid quantities (including velocity) are determined in step 4 of the bisection, it is convenient to recompute the electric field to ensure consistency between the electric field and the velocity. To do this, we rewrite expression (4.70) as

$$\mathbf{E} = A_0\mathbf{E}_* - A_1\mathbf{v}\times\mathbf{B} + A_2(\mathbf{v}\cdot\mathbf{E}_*)\mathbf{v} \tag{4.76}$$

It is important to note that there is no implicit step to perform during the final step of the `MoL` (Equation (4.34)). This means that, in this case, we simply have $\mathbf{E} = \mathbf{E}_*$.

4.7.5 Artificial atmosphere

In order to ensure numerical stability and the accuracy of calculations in simulations involving low-density fluids, it is necessary to impose an artificial atmosphere. This measure prevents the density, or other physical variables, from dropping to values close to zero, thereby avoiding numerical instabilities and computational errors, such as divisions by zero. Additionally, the artificial atmosphere allows for more effective management of boundary conditions in the simulation, stabilizing outgoing flows and

preventing non-physical behaviors from arising. Furthermore, it simplifies the physical model, as introducing an artificial minimum density helps avoid the complexity of dealing with a vacuum, which would require a more advanced treatment. Finally, the use of an artificial atmosphere facilitates the convergence of numerical solutions, as it prevents the computation of extreme values of physical variables, making the system of equations more stable and better conditioned. Therefore, the imposition of an artificial atmosphere proves essential for ensuring stability, consistency, and reliability in numerical simulations in the presence of low-density regions.

The atmosphere is imposed when the density value falls below a certain threshold ρ_{cut}, i.e. when

$$D < \rho_{cut}(1+\delta_\rho) \qquad \text{or} \qquad \rho < \rho_{cut}(1+\delta_\rho) \tag{4.77}$$

where δ_ρ is a tolerance necessary to account for potential numerical errors. In this case, we set

$$\rho = \rho_{atm} \leq \rho_{cut} \tag{4.78}$$

and set the fluid velocity to zero, i.e. $\mathbf{v} = \mathbf{0}$ and $W = 1$. The internal energy and pressure are set using a polytropic equation:

$$\epsilon = \epsilon_{atm} = K\frac{\rho_{atm}^{\Gamma-1}}{\Gamma-1} \tag{4.79}$$

$$p = K\rho_{atm}^{\Gamma} \tag{4.80}$$

Typically, $K = 100$ and $\Gamma = 2$ are assumed. Therefore, the atmosphere is assumed to have a uniform temperature at every point in space.

In the points corresponding to the artificial atmosphere, which is assumed to be non-resistive, the electric field can be computed in several ways. The first method involves imposing the ideal MHD condition, which implies $\mathbf{E} = \mathbf{0}$ since $\mathbf{v} = \mathbf{0}$. The second method consists of deriving the electric field by inverting the equation for conserved momentum, following the approach presented in Paschalidis and Shapiro 2013, i.e.

$$\mathbf{E} = \frac{\mathbf{B}\times\mathbf{S}}{B^2} + \frac{(\mathbf{E}\cdot\mathbf{B})}{B^2}\mathbf{B} \tag{4.81}$$

Following Paschalidis and Shapiro 2013, we enforce the orthogonality of the electric and magnetic fields ($\mathbf{E}\cdot\mathbf{B} = 0$), typical of IMHD and Force-Free Electrodynamics (FFE) regimes, so

$$\mathbf{E} = \frac{\mathbf{B}\times\mathbf{S}}{B^2} \tag{4.82}$$

With zero fluid velocity, the conserved momentum is orthogonal to the magnetic field (i.e., $\mathbf{S}\cdot\mathbf{B} = 0$). This constraint is satisfied by adjusting the conserved momentum according to

$$\mathbf{S} \to \mathbf{S} - \frac{\mathbf{B}\cdot\mathbf{S}}{B^2}\mathbf{B} \tag{4.83}$$

Then, to guarantee a physically admissible norm for $\mathbf{S}$, we impose

$$\mathbf{S} = \mathbf{S} \min\{1, f_S\} \tag{4.84}$$

where

$$f_S = \sqrt{\left(1 - \frac{1}{W^2_{\max}}\right)\frac{B^4}{S^2}} \tag{4.85}$$

4.7.6 Error handling

We now present the error policy that delineates the conditions under which unphysical values of the evolved variables are corrected, as well as the methods used for these corrections. Most of these errors occur at the stellar surfaces, where the densities are low; therefore, the corrections have a minor (though not negligible) impact on the overall dynamics. In detail, we distinguish the following cases:

- If $D < \rho_{cut}(1 + \delta_\rho)$, we set the artificial atmosphere (see Section 4.7.5).
- If $\tau = \mathcal{E} - D < \tau_{atm}$, with $\tau_{atm} = \rho_{atm}\epsilon_{atm}$, adjust $\mathcal{E} = \tau_{atm} + D$.
- If $S^2 > S^2_{\max}$, with $S^2_{\max}$ given by Equation (4.53), adjust

$$\mathbf{S} \to \mathbf{S}\sqrt{\frac{S^2_{\max}}{S^2}} \tag{4.86}$$

Furthermore, the C2P algorithm may occasionally yield unphysical values for the primitive variables. Once these primitive variables are obtained, we evaluate whether any corrections are required:

- If $\rho < \rho_{cut}(1 + \delta_\rho)$ set the artificial atmosphere (see Section 4.7.5).
- In the IMHD regime, if $E \geq B$ adjust

$$\mathbf{E} \to \mathbf{E}\sqrt{\left(1 - \frac{1}{W^2_{\max}}\right)\frac{B^2}{E^2}} \tag{4.87}$$

following the idea presented in Paschalidis and Shapiro 2013. This adjustment is carried out only in the ideal regime because in the resistive regime it is possible to have $E > B$ (Dionysopoulou et al. 2013).

4.7.7 Kinematic approximation

In MIR, we have also implemented the so-called *kinematic approximation*, which assumes that the fluid is in stationary hydrodynamic equilibrium, allowing only electromagnetic quantities to evolve over time. This approximation has been utilized, for

instance, in Bugli et al. 2014, Franceschetti and Del Zanna 2020, Del Zanna et al. 2022 to investigate the dynamo action in accretion disks and proto-neutron stars. Since all hydrodynamic quantities are predetermined, the C2P algorithm is significantly simplified, as only the electric field needs to be computed. In the IMHD regime, this is achieved using Equation (3.89), while in the RMHD regime, it is done using Equation (4.76). However, within the kinematic approximation, we can replace the evolution of the electric field with that of the conserved momentum $\mathbf{S}$, as in Paschalidis and Shapiro 2013. In this approach, we first compute

$$\mathbf{P} = \mathbf{E} \times \mathbf{B} = \mathbf{S} - \mathbf{M} = \mathbf{S} - \rho h W^2 \mathbf{v} \tag{4.88}$$

and then compute the electric field using Equation (4.82), with the substitution $\mathbf{S} \to \mathbf{P}$.

4.7.8 Development decisions: from literature to a custom approach

At the beginning of this section we briefly mentioned that several schemes have been proposed in the literature for recovering primitive variables from conservative ones. Now, we provide a general overview of the advantages and disadvantages of the various existing schemes, without analyzing each one individually. We also present the reasons why we chose to develop a new algorithm for the resistive case, rather than using one of the previously established methods.

The system of evolution equations, comprising two scalar equations (density and energy) and three vector equations (momentum and electromagnetic fields), is incomplete. To complete the system, constitutive relations are required to link thermodynamic quantities (such as pressure, described by the equation of state) and electromagnetic quantities (such as current density) to the other variables of the system. The equation of state provides a relation between pressure, density, and temperature, while an additional constitutive relation is necessary to describe the current density as a function of other variables, such as the electric field. The functional form of these constitutive relations limits the physical phenomena that can be modeled. Processes that significantly modify the EoS or the electromagnetic constitutive relations are not permitted within this formalism. The algorithms used to convert conserved variables into primitive ones are strongly dependent on the adopted functional relations. As a result, an algorithm that is robust in a specific physical regime may become unstable under different conditions, or even fail entirely when applied to a different EoS or physical regime.

Bracketing methods, such as bisection, are known for their robustness but exhibit slow convergence. In contrast, Newton-Raphson method converges rapidly but requires an accurate initial guess and the computation of pressure derivatives. The latter represents a significant challenge, especially for tabulated equations of state. Tabulated equations of state contain a finite number of data points, limiting the accuracy with which derivatives can be computed. In particular, as the number of equation of state parameters increases, the density of points in the table decreases for each parameter

combination. Consequently, estimates of derivatives, obtained through finite differences or interpolation, are subject to increased numerical noise. To overcome these difficulties, bracketing methods are preferred in ideal hydro and MHD regimes, as they do not require the computation of derivatives. Although convergence is slower, their robustness and the ability to reformulate the problem in terms of a single scalar parameter make them a reliable choice in these cases (e.g., Galeazzi et al. 2013, Kastaun et al. 2021).

The presence of the implicit step in the resistive regime prevents the reformulation of the problem in terms of a single scalar parameter, due to the presence of three additional unknowns (namely, the components of the electric field). The application of multidimensional bisection becomes thus unfeasible. The problem of bisection in a space of dimension $N > 1$ is primarily characterized by geometric complexity and the management of subsections. Unlike lower dimensions, where subdivision is relatively straightforward, in N dimensions one works with hyper-rectangles, and each subdivision generates an exponential number of subregions. This exponential growth makes it challenging to monitor the boundary surfaces and the interactions between the various volumes. Moreover, creating very small subsections, while it may seem an effective way to approach the solution, introduces the risk of converging to a root different from the one sought. Excessive subdivision of the volume can lead to local fluctuations that do not represent the true trend of the function, as well as potential rounding errors and inaccurate estimates. In the case of multiple roots, the algorithm may also ignore other valid solutions or halt in insignificant regions. The management of subsections thus becomes a complex task, increasing the computational load and making it difficult to interpret the results.

This is why in Bucciantini and Del Zanna 2012, Del Zanna and Bucciantini 2018, Tomei et al. 2019, Mattia et al. 2023 and other works, a 3D Newton-Raphson method has been preferred for recovering primitive variables. However, even this scheme presents several significant challenges. First, the calculation of the Jacobian matrix is essential, as it represents the partial derivatives of the functions with respect to the variables. Nevertheless, this calculation can be computationally expensive and complex, especially when the functions are intricate. Additionally, local convergence is a critical issue. Although the method is known for its rapid convergence when close to a root, this characteristic is not guaranteed throughout the entire space. If the starting point is too far from the solution, the iteration may diverge or even converge to an incorrect root. The presence of multiple roots or complex nonlinear behaviors further complicates the situation, as the method may oscillate between different solutions, making it challenging to identify the desired one. Numerical stability also plays an important role; numerical errors can arise from the computation of derivatives and the resolution of the system of equations, potentially amplifying and compromising the final accuracy. Finally, the choice of the initial point is crucial for the success of the method. In a three-dimensional space, identifying an appropriate starting point near the desired root can be challenging. An inappropriate choice can lead to slow convergence or, worse, divergence.

As is evident from the preceding discussion, the optimal scheme for converting conservative variables into primitive variables remains elusive, given the advantages and disadvantages of various numerical methods and the increasing complexity of the equations employed as the physical regime of the simulation varies.

In developing the numerical scheme outlined in this section, we sought to leverage the strengths of various numerical methods and to mitigate their weaknesses, fully aware that complete elimination is not possible. By employing the Newton-Raphson method for electric field calculations, we achieved relatively rapid convergence for the field components. The disadvantage associated with computing the derivatives of pressure is avoided by performing this step within a bisection carried out on a parameter μ that includes the pressure itself. Therefore, the calculation of the electric field is performed at a fixed μ, eliminating the need to calculate the pressure derivatives. The bisection algorithm offers additional advantages, including robustness and the ability to handle the failure of the inner Newton-Raphson 3D scheme. In this case, an incorrect electric field leads to an incorrect μ, causing the bisection to adjust its bounds rather than failing outright. Consequently, the overall scheme can better accommodate the failure of the 3D component without jeopardizing the entire calculation. Moreover, the method is compatible with both analytical and tabulated equations of state, as it does not require the computation of pressure or other thermodynamic variable derivatives.

The challenge of computing pressure derivatives for tabulated equations of state is not confined to the recovery of primitive variables, but also extends to the calculation of flux terms. Riemann solvers, in particular, require the computation of characteristic velocities, including the speed of sound, which is directly linked to pressure derivatives. Consequently, the issues outlined above also impact other parts of the code. This is why tabulated equations of state are not currently implemented in the MIR code, despite their greater realism compared to the analytical equations presented in Section 3.3.

4.8 Electric charge

The computation of the electric current density (3.96) requires the computation of the electric charge density, given by the divergence of the electric field. We have implemented two distinct methods to achieve this. The first method employs finite differences, which is the approach utilized in the `ECHO` code. The second method employs a Riemann solver to determine the divergence. In this case, the flux is represented by the electric field and can be calculated at each cell interface using, for instance, Equation (4.19) with $\boldsymbol{\mathcal{U}}^i_{R,j} = \boldsymbol{\mathcal{U}}^i_{L,j} = 0$ (see Appendix C for the proof).

Chapter 5

Numerical results

During the development of a numerical code, it is essential to verify that the obtained solutions are both correct and reliable. In the case of magnetohydrodynamics, this requirement is particularly crucial due to the complexity of the system of equations describing the interaction between conductive fluids and magnetic fields. However, the necessity of testing a code is not limited to ensuring the correct solution of the magnetohydrodynamics equations but rather concerns the code's ability to address complex numerical problems while maintaining precision, stability, and physical consistency.

A numerical code must undergo rigorous testing for several reasons. Firstly, it is essential to verify that the implemented algorithms are correct and that the obtained solutions are consistent with theoretical expectations. Additionally, tests allow for the identification and correction of any implementation errors that could compromise the validity of the results.

In this chapter, we present the results of a series of standard tests from the literature, used to evaluate the performance of our code. These tests, designed to probe various critical aspects of numerical behavior, such as the handling of discontinuities, the conservation of physical quantities, and robustness with respect to initial and boundary conditions, provide fundamental validation. Rigorous testing of the code is an indispensable step to ensure that it can be successfully applied in practical scenarios, providing reliable and physically accurate results even in complex and realistic contexts.

Subsequently, we present the results of a specific physical application of our code, focusing on the first simulations of bar-mode instability in the resistive regime. This instability, which emerges in highly distorted rotating systems, represents a phenomenon of great interest as it closely mirrors the post-merger phase in binary neutron star systems. In the post-merger scenario, in fact, the strong deformations and present magnetic fields play a crucial role in the system's dynamical evolution.

The simulations conducted have a twofold purpose. On the one hand, we aim to study in detail the influence of resistivity in these astrophysical contexts, assessing how

it may affect the growth and dynamics of bar-mode instability. Resistivity, in fact, can play a significant role in the dissipation of the magnetic field and the alteration of the fluid-structure of the system. On the other hand, these simulations allow us to verify the ability of our code to maintain its accuracy and reliability in the presence of asymmetries and complex phenomena. In particular, verifying the convergence of the code in asymmetric situations is essential to guarantee its accuracy and robustness in highly dynamic scenarios such as those in astrophysics.

Therefore, the following results represent a critical benchmark for gaining a better understanding of the physical processes associated with bar-mode instability in the resistive regime and for demonstrating the effectiveness and reliability of our numerical approach in realistic and strongly asymmetric contexts.

The tests presented in this chapter are presented in four sections. In the first two sections, concerning one-dimensional and two-dimensional tests, the numerical grids present only one refinement level. In the last two sections, concerning three-dimensional tests and the study of the bar-mode instability in the resistive regime, the numerical grids present different refinement levels, to take into account the boundary conditions around the stars. Local resolution is increased using the Fixed Mesh Refinement (FMR), also known as Box-in-Box, where each refinement level has size and grid spacing in each direction half that of the previous one. Therefore, for grids with four refinement levels, the size of the coarsest grill is eight times that of the finest grid. For these simulations, we report the dimensions and grid spacing of the finest grid, in which the physics is simulated.

5.1 One-dimensional tests

First, we present the result of two standard one-dimensional (1D) tests. Performing 1D tests for a numerical code, even when it is designed to simulate more complex phenomena in two (2D) and three (3D) dimensions, is essential for several reasons. Firstly, one-dimensional tests provide simpler, well-controlled cases, often accompanied by analytical or semi-analytical solutions, allowing for an easier verification of the accuracy of the code's results. This is a crucial step to ensure that the implementation of the physical equations is accurate. Reduced complexity is another significant advantage of 1D tests. Simulating phenomena in a single dimension requires fewer computational resources and allows for faster simulations. This makes it easier to identify and correct errors, as the amount of data to analyze is limited, and it's simpler to verify if each component of the code is working correctly. Furthermore, problems identified in 1D tests often signal underlying systematic errors that can propagate into higher-dimensional simulations. Resolving these issues early in the 1D phase can save significant time and effort in the long run. Finally, 1D tests provide a means to directly assess the numerical stability of the code. By identifying and addressing stability issues early in the 1D phase, we can prevent them from propagating into higher-dimensional simulations and

compromising the overall accuracy of the results.

5.1.1 Self-similar current sheet

The *self-similar current sheet* is a configuration of magnetic field and electric current that evolves over time while maintaining a proportionally invariant structure. In other words, although the configuration changes, for instance, by elongating or thinning, its overall shape remains similar to itself during temporal evolution. This type of behavior is referred to as "self-similar" and occurs when a system evolves according to scaling laws that preserve the proportional relationships among the various physical quantities involved. A *current sheet* is a very thin region of space where electric current is highly concentrated. This is often associated with discontinuities in the magnetic field, creating conditions favorable for magnetic reconnection phenomena (e.g., Cassak and Drake 2013). The self-similar property of the current sheet greatly simplifies the description of the phenomenon. Even as the current sheet expands or evolves over time, the profiles of current density and magnetic field always maintain the same shape, which allows for the analysis of the system's evolution using analytical or semi-analytical methods.

The numerical problem was first proposed by Komissarov 2007. Following the same prescription, it has been presented also by Palenzuela et al. 2009, Dumbser and Zanotti 2009, and Bucciantini and Del Zanna 2012. The exact solution for the $y-$component of the magnetic field in the limit of infinite pressure is

$$B^y(x,t;\eta) = B_0 \,\mathrm{erf}\left(\frac{x}{2\sqrt{\eta t}}\right) \tag{5.1}$$

where erf is the error function. The initial conditions for the numerical test are $\rho = 1$, $p = 50$, $\mathbf{v} = \mathbf{0}$, $\mathbf{E} = \mathbf{0}$, $\mathbf{B} = (0, B^y(x,t_i;\eta), 0)$, with t_i the initial time. We have chosen $B_0 = 1$ and an adiabatic coefficient $\Gamma_{\rm th} = 4/3$. The computational domain spans the range $x \in [-1.5, 1.5]$ and is structured using a uniform grid consisting of 200 cells. In Komissarov 2007 and subsequent works, simulation results with $\eta = 10^{-2}$, $t_i = 1$, and $t_f = 10$ (where t_f is the final time) were presented. In this work, we report the results obtained with 4 different values of η, keeping the initial and final products ηt_i and $\eta t_f constant$. Specifically, the values of the times t_i and t_f were chosen based on the value of η such that $\eta t_i = 0.01$ and $\eta t_f = 0.1$. The four tercets used are, therefore:

$$(\eta, t_i, t_f) = \left(10^{-1}, 0.1, 1\right) \tag{5.2}$$

$$(\eta, t_i, t_f) = \left(10^{-2}, 1, 10\right) \tag{5.3}$$

$$(\eta, t_i, t_f) = \left(10^{-3}, 10, 100\right) \tag{5.4}$$

$$(\eta, t_i, t_f) = \left(10^{-4}, 100, 1000\right) \tag{5.5}$$

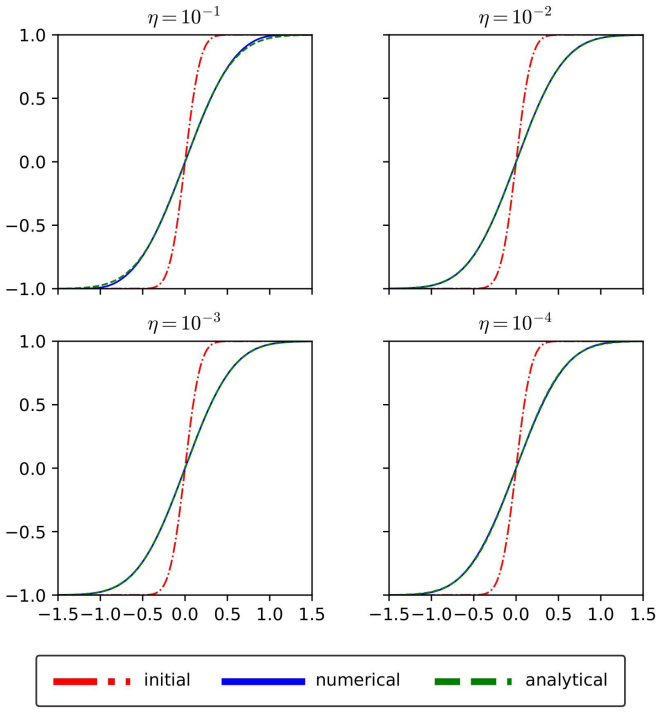

Figure 5.1: Evolution of the $y-$component of the magnetic field in a self-similar current sheet for different values of electrical resistivity η. The red dot-dashed line represents the initial condition. The blue solid line depicts the numerical solution, which is indistinguishable from the green dashed line representing the exact solution given by Equation (5.1). The initial and final times for each simulation are detailed in the text (Equations (5.2) to (5.5)).

Despite the evolution being predominantly resistive (theoretically, in the limit of infinite pressure, only the magnetic field evolves, and only the induction equation needs to be solved), the problem is treated within the fully dynamical regime. The CFL factor[12] was set to 0.125.

By maintaining the spatial numerical grid unchanged, we were able to assess the

[12]The *CFL factor* (derived from the **C**ourant-**F**riedrichs-**L**ewy condition) is a parameter used to ensure numerical stability in simulations that solve partial differential equations. The CFL condition establishes a limit on the time step Δt based on the spatial resolution Δx and the characteristic velocity of the system $v_{\max}$ (such as the speed of sound or fluid flow speed). This condition is crucial for the stability of numerical solutions, particularly when using explicit time integration methods like Runge-Kutta. The CFL condition can be written as:

$$\Delta t \leq \frac{\Delta x}{v_{\max}}$$

The CFL factor (denoted as C) is a multiplier applied to this theoretical maximum, typically

impact of numerical viscosity on our simulations. The initial and final configurations are, in fact, theoretically the same regardless of the value of η, while the evolution depends on the electrical resistivity. Substantial differences between the analytical and numerical solutions would imply a significant impact of numerical viscosity. However, as shown in Figure 5.1, there is excellent agreement between the two solutions (with the numerical solution represented in blue and the analytical solution in green, while the red line indicates the initial configuration). his indicates that, at this resolution, the intrinsic resistivity of the scheme is less than 10^{-4}.

5.1.2 Shock Tube

The second test is the *shock tube* problem presented in Dumbser and Zanotti 2009. The shock tube problem is a well-established numerical test used to evaluate the performance of computational codes, particularly in the context of fluid dynamics and magnetohydrodynamics. It involves the simulation of discontinuities, such as shock waves, contact discontinuities, and rarefaction waves, which arise from an initial imbalance between two regions of fluid or plasma.

From a numerical perspective, shock tube simulations provide insight into the code's ability to handle sharp gradients and discontinuities without introducing unphysical oscillations. Additionally, the problem reveals the effectiveness of the flux solvers and reconstruction schemes in maintaining accuracy and stability under extreme conditions. Overall, successful results in shock tube simulations are a strong indicator of a code's robustness and reliability in solving more complex physical scenarios.

The test was conducted on a stationary Cartesian grid (i.e., Minkowski spacetime). This simulation was performed under both ideal and resistive magnetohydrodynamic conditions, employing the Lax-Friedrichs flux solver. The TVD MC2 scheme was employed as the reconstruction method. The time integrator used is the second-order Runge-Kutta (RK2) scheme in the IMHD regime and the Strong Stability Preserving (SSP2(2,2,2)) scheme in the resistive regime. The CFL factor was set to 0.125 in both regimes, and the electrical resistivity remained constant throughout the domain. The results of our tests should be compared with those presented in Bucciantini and Del

chosen so that $0 < C \leq 1$. The time step used in the simulation is then determined by:

$$\Delta t = C \cdot \frac{\Delta x}{v_{\max}}$$

If C is close to 1, the time step is near the maximum allowed by the stability condition. If C is less than 1, the time step is reduced, improving numerical stability at the cost of requiring more time steps to complete the simulation. A CFL factor set to 0.125 means that the time step used in the simulation is 12.5% of the theoretical maximum allowed for stability. This choice ensures greater numerical stability, although it requires more computational time to complete the simulation.

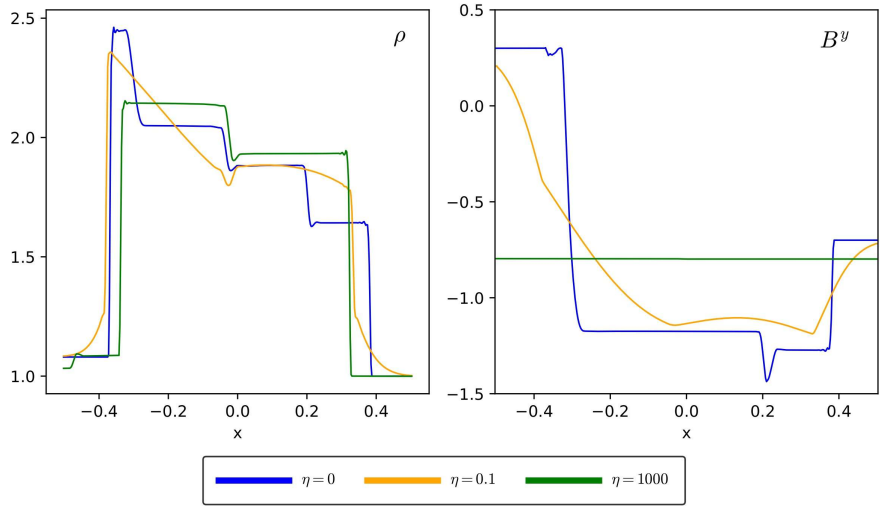

Figure 5.2: Results of the shock tube problem at the final time $t = 0.55$. The left panel shows the density, while the right panel shows the $y-$component of the magnetic field. The blue line corresponds to the case $\eta = 0$, the orange line to $\eta = 0.1$, and the green line to $\eta = 1000$.

Zanna 2012.

The initial conditions were given by[13]

$$(\rho, p, v^x, v^y, v^z, B^x, B^y, B^z) = (1.08, 0.95, 0.4, 0.3, 0.2, 2.0, 0.3, 0.3) \qquad \text{for } x < 0 \quad (5.6)$$

and

$$(\rho, p, v^x, v^y, v^z, B^x, B^y, B^z) = (1.0, 1.0, -0.45, -0.2, 0.2, 2.0, -0.7, 0.5) \qquad \text{for } x > 0 \quad (5.7)$$

while the initial electric field was set equal to the IMHD value. The x-coordinate spanned the range $[-15, 15]$, and a uniform grid with 400 cells was employed. The final time was set to $t = 0.55$. To investigate the effects of electrical resistivity, the test was repeated for three different values: $\eta = 0$, $\eta = 0.1$, and $\eta = 1000$. The adiabatic index for the Ideal Fluid EoS was $\Gamma_{\rm th} = 5/3$. The results, illustrated in Figure 5.2, demonstrate exact correspondence with those presented in Bucciantini and Del Zanna 2012 in all cases.

[13]We remind the reader that in this work we have set $G = M_\odot = c = \varepsilon_0 = \mu_0 = 1$. Therefore, in the absence of physical units and/or unless otherwise explicitly stated, numerical values in this chapter should be understood to be in geometrized units.

5.2 Two-dimensional test: magnetic rotor

We now present the results of a standard two-dimensional (2D) test: the magnetic rotor. Testing a code using two-dimensional configurations offers several advantages. In particular, 2D simulations require fewer computational resources compared to 3D simulations, allowing tests to be conducted more quickly and with lower memory requirements. This facilitates a more frequent and timely verification process. Furthermore, the results of 2D simulations are often easier to visualize and interpret, which aids in the rapid identification of errors or anomalies within the code. The simplicity of the two-dimensional system also allows for more straightforward control of variables and parameters, enabling the isolation and testing of specific aspects of the code without the additional complexities associated with three-dimensional (3D) simulations. Additionally, two-dimensional configurations facilitate the rapid identification of potential numerical instabilities or convergence issues, enabling preliminary validation of the code within a controlled environment before advancing to more complex simulations. Finally, for certain physical phenomena, a 2D simulation may be sufficiently representative, facilitating the analysis of specific dynamics without the burden of 3D complexities.

The numerical test was initially proposed in its relativistic IMHD formulation by Del Zanna et al. 2003. The resistive version was subsequently introduced by Dumbser and Zanotti 2009. It was conducted on a stationary Cartesian grid (i.e., Minkowski spacetime). This simulation was performed under both ideal and resistive magnetohydrodynamic conditions, employing the Lax-Friedrichs flux solver. The TVD MC2 scheme was employed as the reconstruction method. The time integrator used is the second-order Runge-Kutta (RK2) scheme in the IMHD regime and the Strong Stability Preserving (SSP2(2,2,2)) scheme in the resistive regime. The CFL factor was set to 0.125 in both regimes, and the electrical resistivity remained constant throughout the domain. The results of our tests should be compared with those presented in Bucciantini and Del Zanna 2012.

The initial configuration consisted of a circular region with a radius of $r = 0.1$ and a density of $\rho = 10$, rotating with a uniform angular velocity of $\Omega = 8.5$. This region was embedded within a static medium characterized by a density of $\rho = 1$. A uniform pressure of $p = 1$ and a magnetic field $(B^x, B^y, B^z) = (1, 0, 0)$ were maintained throughout the domain. The adiabatic index for the Ideal Fluid EoS was set at $\Gamma_{\rm th} = 5/3$, and the initial electric field was assigned the IMHD value. The simulation concluded at a final time of $t = 0.3$. The computational domain spanned $x = [0, 1]$ and $y = [0, 1]$, with the center of the circular region located at $(x, y) = (0.5, 0.5)$. A uniform grid comprising 400×400 cells was employed. This test was executed in both the IMHD regime and the resistive regime, with the resistivity set to $\eta = 0.1$. The results, as illustrated in Figure 5.3, demonstrate exact correspondence with those presented in Bucciantini and Del Zanna 2012 for all cases.

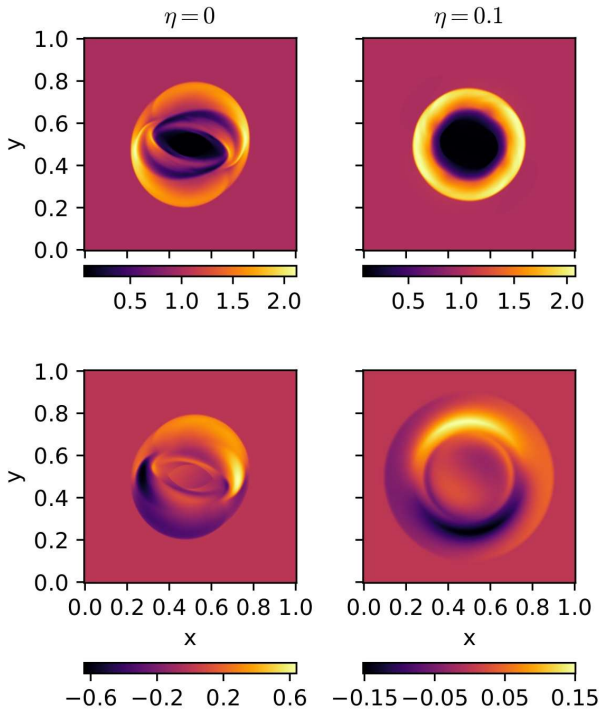

Figure 5.3: Results of the magnetized rotor problem at the final time $t = 0.3$. The upper panels illustrate the pressure, while the lower panels depict the $z-$component of the electric field. The left column corresponds to the IMHD case ($\eta = 0$), while the right column represents the resistive case with $\eta = 0.1$.

5.3 Three-dimensional tests

After validating the code through tests in both one and two dimensions, we now present the results of several standard three-dimensional (3D) tests. While 2D simulations offer valuable insights, many physical phenomena exhibit inherently three-dimensional behaviors that cannot be fully captured in two dimensions. Testing the code in 3D configurations is thus essential to ensure its robustness and accuracy in more realistic and complex scenarios.

Three-dimensional simulations introduce additional degrees of freedom, allowing for a more comprehensive exploration of physical systems, particularly when dealing with phenomena such as turbulence, instabilities, or interactions that depend on spatial variation in all three dimensions. However, this increased complexity comes with the need for greater computational resources, both in terms of processing power and memory. Consequently, 3D simulations require more time and computational effort, but they are crucial for accurately replicating the full dynamics of many astrophysical and physical systems.

Moreover, 3D tests provide a more rigorous validation of the numerical methods and algorithms used in the code. They are particularly effective in uncovering any issues related to dimensional scaling, boundary conditions, or numerical stability that may not have surfaced in 2D configurations. The ability of the code to handle these challenges in 3D is a key indicator of its reliability and applicability to real-world simulations.

5.3.1 TOV star

The first 3D test we present is that of a non-rotating star in hydrostatic equilibrium, a condition described by the Tolman-Oppenheimer-Volkoff (TOV) equation[14]:

$$\frac{\mathrm{d}p(r)}{\mathrm{d}r} = -\frac{[e(r)+p(r)]\big[m(r)+4\pi r^3 p(r)\big]}{r^2[1-2m(r)/r]} \tag{5.8}$$

where $p(r)$ and $e(r) = \rho(r)[1+\epsilon(r)]$ are pressure and energy density, respectively, at radius r, $m(r)$ is the total mass within radius r, and the term $[1-2m(r)/r]$ accounts for the curvature of spacetime around the star, as described by general relativity. This equation represents a relativistic generalization of the classical hydrostatic equilibrium equations for spherically symmetric celestial objects.

Testing the code with a star in equilibrium provides an ideal verification environment: the expected physical behavior is simple (the star should not evolve significantly), allowing us to focus on potential issues related to numerical stability and solution accuracy. In this way, any errors related to the numerical method or approximations can be efficiently identified and corrected before tackling more complex or dynamic problems.

The initial configuration was generated using the `RNS` code[15] (Font et al. 2000) for a polytropic star with adiabatic index $\Gamma = 2$, polytropic constant $K = 100$, and initial central rest-mass density $\rho_c = 1.28 \times 10^{-3}$. The subsequent evolution was carried out with the Ideal Fluid EoS, maintaining the same value of Γ. The test was performed on a cubic Cartesian grid with four refinement levels. The $x-$, $y-$, and $z-$coordinates of the finest grid spanned the range $[-15, 15]$ with grid steps $dx = dy = dz = 0.375$. The simulation ran for 8 milliseconds using the WENO-Z reconstruction method, the HLLE

[14] We remind the reader that in this work we have set $c = G = 1$. In physical units we would have had

$$\frac{\mathrm{d}p(r)}{\mathrm{d}r} = -\frac{G}{r^2}\left(e(r)+\frac{p(r)}{c^2}\right)\left(m(r)+\frac{4\pi r^3 p(r)}{c^2}\right)\left(1-\frac{2Gm(r)}{rc^2}\right)^{-1}$$

[15] The `RNS` (Rapidly **R**otating **N**eutron **S**tar) code is a numerical tool designed to compute equilibrium configurations of rapidly rotating neutron stars in general relativity. It assumes axisymmetry and solves both the Einstein field equations and the hydrostatic equilibrium equations for rotating stars in a two-dimensional framework.

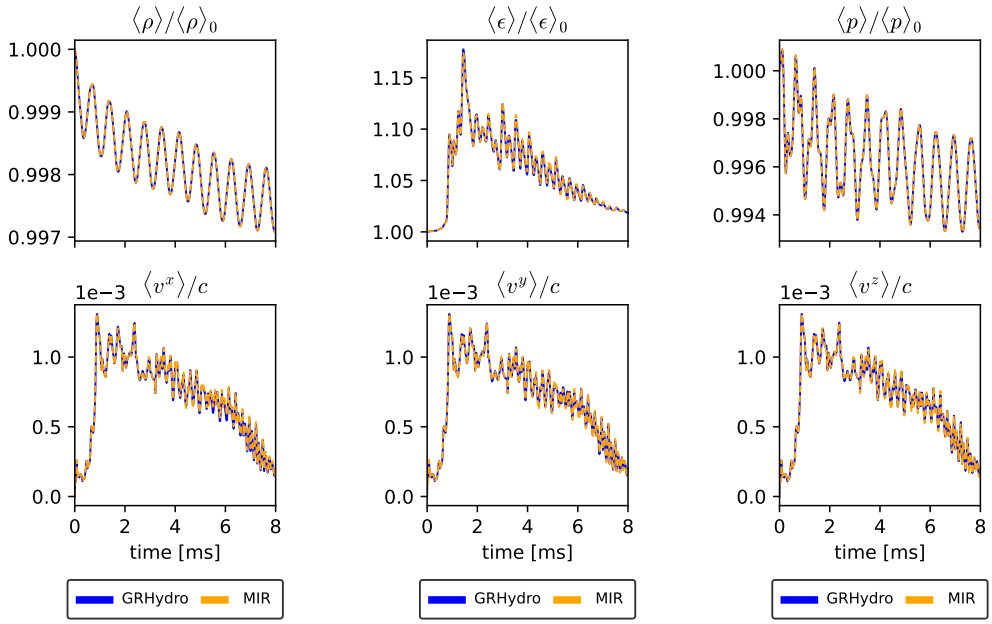

Figure 5.4: Results of the TOV star simulations. Top panel: Time evolution of the average values of the rest-mass density normalized to its initial value (left), internal energy normalized to its initial value (center), and pressure normalized to its initial value (right). Bottom panel: As in the top panel, but for the three components of the velocity normalized to the speed of light.

flux solver, and the fourth-order Runge-Kutta (RK4) time integrator with a CFL factor of 0.25.

To assess the accuracy of our code, we compared the results with those obtained using the `GRHydro` code. Figure 5.4 illustrates the time evolution of the average values of the rest-mass density, internal energy, pressure, and the three components of the fluid velocity, demonstrating strong agreement between the two codes.

Despite the star being initially in a stable equilibrium and non-rotating, the average velocity is found to be non-zero. This can be attributed to several factors, such as numerical truncation, grid resolution, and numerical instabilities introduced by the time integration algorithm, which can generate spurious velocities. However, the primary contribution is due to the presence of the so-called "numerical wind". *Numerical wind* is a phenomenon in fluid simulations, referring to artificial material flow caused by numerical errors or instabilities. It is not a physical phenomenon but rather a result of limitations and approximations inherent in the numerical methods used to solve the fluid dynamics equations, particularly in the treatment of the atmosphere. As

discussed in Section 4.7.5, numerical codes commonly model the atmosphere as a layer of low-density gas to avoid computational issues in near-vacuum regions. However, this artificial atmosphere is still governed by fluid dynamics equations, meaning that even small perturbations can generate artificial flows or non-physical motions within it. These motions can manifest as numerical wind interacting with the stellar surface, resulting in non-zero velocities. The interface between the star and the artificial atmosphere is a region where significant numerical errors can arise, particularly if the stellar density is much greater than that of the atmosphere. These errors can generate spurious flows in the atmosphere, which may subsequently be transmitted to the star, resulting in artificial motions that manifest as non-zero velocities.

5.3.2 Magnetized rotating star in the ideal regime

We now present the results of a time evolution simulation of a uniformly rotating magnetized star in equilibrium, carried out in the IMHD. The initial configuration was constructed using the `XNS`[16] (Bucciantini and Del Zanna 2011, Pili et al. 2014) code, employing the same parameters as in the previous test for the equation of state, i.e., a polytropic EoS with adiabatic index $\Gamma = 2$, polytropic constant $K = 100$, and initial central rest-mass density $\rho_c = 1.28 \times 10^{-3}$. The star's rotation rate was set to $\Omega = 1.1 \times 10^{-2}$. The magnetic field is dipolar, with a maximum strength of $B_{\max} \approx 2.63 \times 10^{12}$ G. The numerical grid, flux solver, reconstruction method, time integrator, and CFL factor are identical to those employed in the previous test.

As mentioned in the introduction to this thesis, IMHD simulations are subject to the "*energy cascade towards small scales*" due to the absence of physical dissipative terms, inevitably leading to the divergence of the numerical solution. To address this issue, Maxwell's equations, specifically the equation describing the evolution of the magnetic field, are modified by adding term that aim to dampen spurious numerical oscillations, thereby acting as dissipative terms. One of the most commonly used prescriptions is the fifth-order Kreiss-Oliger dissipation[17] (Kreiss and Oliger 1973). However, choosing the appropriate value for the dissipation parameter ϵ_{dis} is not straightforward; it must be chosen theoretically to eliminate numerical errors while simultaneously preserving

[16] The `XNS` code is a numerical tool designed to compute equilibrium configurations of rotating and magnetized neutron stars in general relativity. It assumes axisymmetry and solves both the Einstein field equations and the magnetohydrostatic equilibrium equations for neutron stars in a two-dimensional framework, doing so under the so-called *eXtended Conformally Flat Condition* (XCFC; Cordero-Carrión et al. 2009).

[17] The n-th order Kreiss-Oliger dissipation added to the right-hand side of evolution equations is

$$D_{KO} = (-1)^{(n+3)/2} \frac{\epsilon_{dis}}{2^{n+1}} \left(h_x^n \frac{\partial^{(n+1)}}{\partial x^{(n+1)}} + h_y^n \frac{\partial^{(n+1)}}{\partial y^{(n+1)}} + h_z^n \frac{\partial^{(n+1)}}{\partial z^{(n+1)}} \right) \boldsymbol{\mathcal{U}}$$

where h_x, h_y, and h_z are the local grid spacings in each Cartesian direction. The evolution equations then become $\partial_t \boldsymbol{\mathcal{U}} \to \partial_t \boldsymbol{\mathcal{U}} + D_{KO}$.

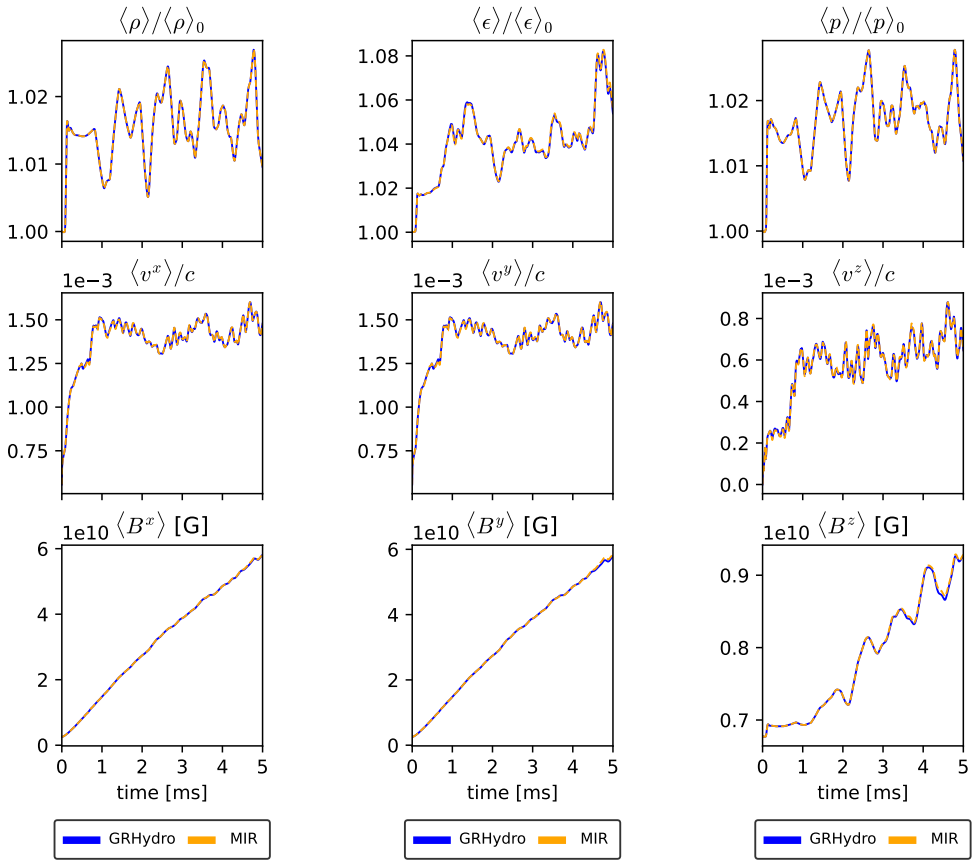

Figure 5.5: Results of the IMHD simulations for the magnetized rotating star. Top panel: Time evolution of the average values of the rest-mass density normalized to its initial value (left), internal energy normalized to its initial value (center), and pressure normalized to its initial value (right). Central panel: As in the top panel, but for the three components of the velocity normalized to the speed of light. Bottom panel: As in the central panel, but for the magnetic field in gauss.

physical instabilities. In the test presented here, we have set $\epsilon_{dis} = 10^{-2}$.

To compare the simulation results with those obtained using the `GRHydro` code, we enforced the magnetic field to be zero in the atmosphere, even when using the MIR code. Additionally, the initial electric field was evaluated using the IMHD relation and evolved using the same prescription.

The results of the simulation are illustrated in Figure 5.5. As can be seen, there is good agreement between the results of the two codes. The results presented are restricted to the first 5 milliseconds due to the onset of numerical wind effects, which, as we will see later, can significantly alter the evolution of the electromagnetic fields.

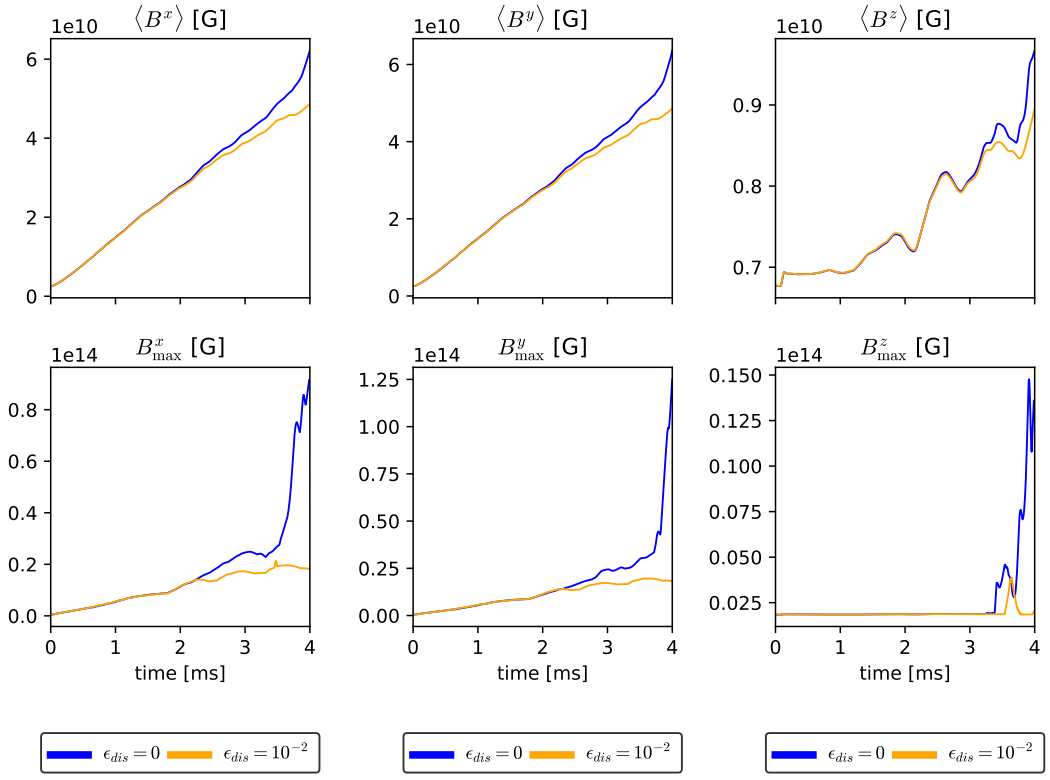

Figure 5.6: Comparison of IMHD simulation results for a magnetized rotating star, showing the effects of artificial dissipation on the magnetic field components. Top panel: average values. Bottom panel: maximum values.

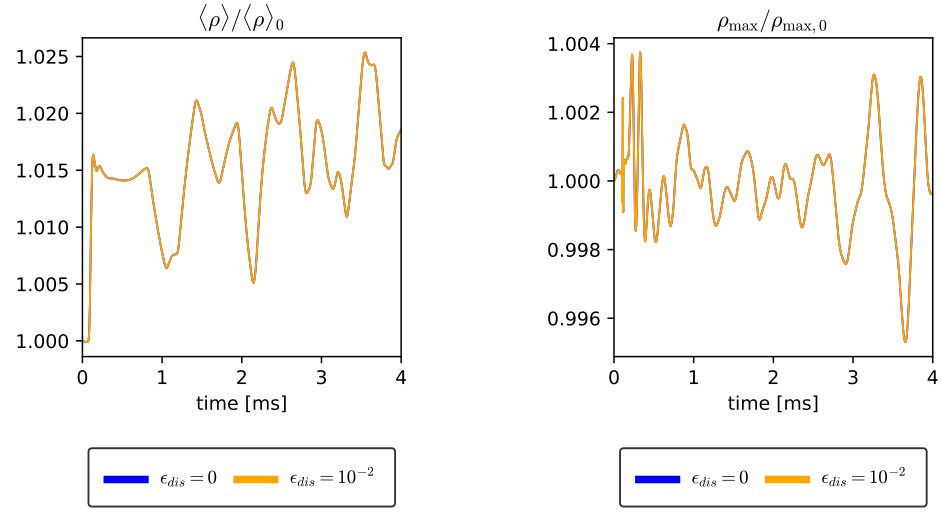

Figure 5.7: Comparison of IMHD simulation results for a magnetized rotating star, showing the effects of artificial dissipation on the rest mass density normalized to its initial value. Left: average value. Right: maximum value.

Consequently, different simulation regimes and error-handling procedures for recovering primitive variables can introduce discrepancies in the solutions.

To substantiate the aforementioned claim regarding the necessity of artificial dissipation in the ideal regime, we have repeated the simulation without including this term. Figure 5.6 shows the resulting time evolution of the mean (upper panels) and maximum (lower panels) values of the magnetic field components. As can be seen, in the absence of artificial dissipation (blue solid line), the magnetic field undergoes a rapid growth after approximately 3 ms. Over time, this growth leads to the simulation's failure. However, the density remains unaffected by this divergence, as illustrated in Figure 5.7. Therefore, artificial dissipation in the ideal regime is indeed essential to prevent an uncontrolled growth of the magnetic field.

5.3.3 Magnetized rotating star in the resistive regime

We now consider the same star as in the previous test, but this time in a resistive regime. We employed the SSP2(2,2,2) time integrator, an IMEX extension of the RK2 method. To ensure stability, the CFL factor was halved to 0.125. A constant electrical resistivity was assumed throughout the stellar interior, while the exterior was considered non-resistive. The atmosphere was thus treated as Ideal MHD, and the electric field was evaluated accordingly.

To the best of our knowledge, the effectiveness of introducing electrical resistivity in suppressing the spurious oscillations and numerical errors that commonly arise in ideal MHD simulations has not been rigorously tested in the resistive regime. This study aims to determine whether: 1) artificial dissipation can be entirely removed in resistive simulations; and 2) if artificial dissipation is still necessary, whether it should be added only to the magnetic field equation, as in the ideal case, or also to the electric field equation, despite the presence of a resistive term.

We begin by comparing the results of simulations in the resistive regime with artificial dissipation added to both electric and magnetic fields to those where artificial dissipation was added only to the magnetic field (in both ideal and resistive regimes). The electrical resistivity inside the star was set to 10^{-10}, while the artificial dissipation parameter was set to 10^{-2}, as in the previous test. The average values of the electric and magnetic field components are illustrated in Figure 5.8. The blue line corresponds to the simulation in the ideal regime, the orange line to the simulation in the resistive regime with artificial dissipation applied only to the magnetic field, and the green line to the simulation in the resistive regime with artificial dissipation applied to both fields. The enhanced fields represented by the green line are a numerical artifact introduced by the artificial dissipation in the electric field equation. This indicates that the artificial dissipation term acts as a source of amplification, which is not expected. Artificial dissipation is generally introduced to suppress numerical instabilities and spurious oscillations, not to amplify them. Therefore, the observed amplification suggests that the dissipation parameter might be incorrectly applied, leading to non-physical behavior in

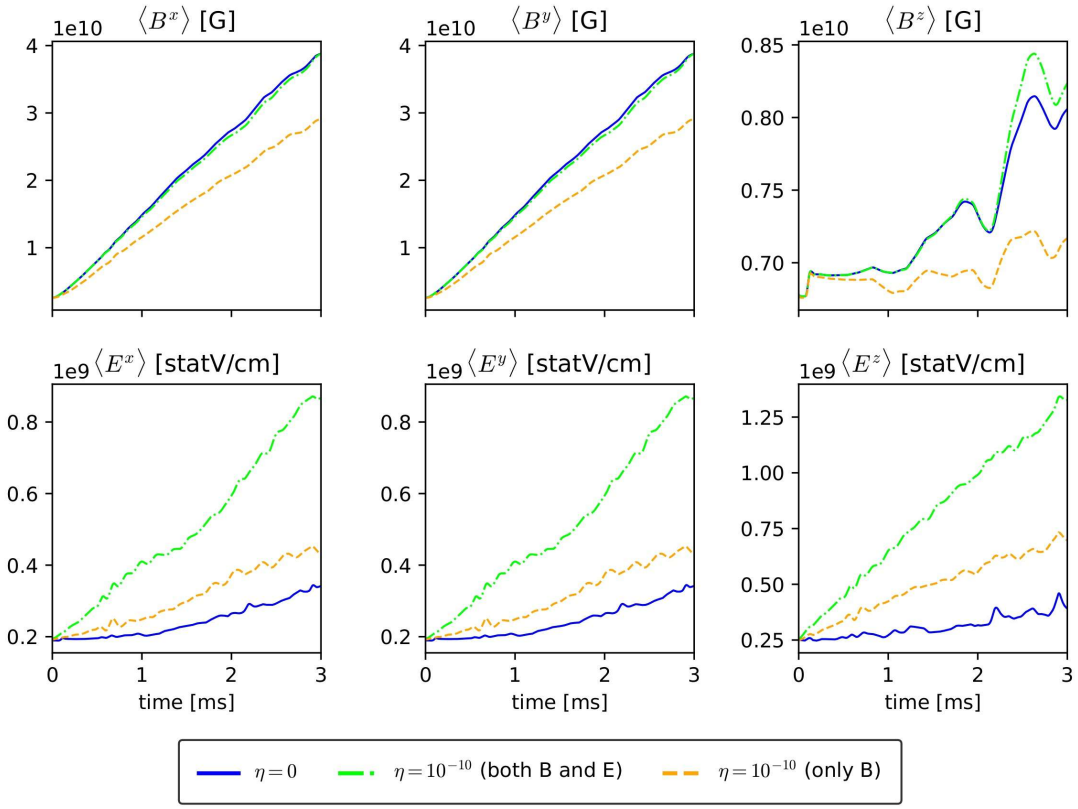

Figure 5.8: Comparison of simulation results for the magnetized rotating star in the ideal and resistive regimes with artificial dissipation ($\epsilon_{dis} = 10^{-2}$) applied to the magnetic field only (blue and orange lines) and to both the magnetic and electric fields (green line). Top row: components of the magnetic field in gauss. Bottom row: components of the electric field in statvolt per centimeter. Left column: $x-$component. Central column: $y-$component. Right column: $z-$component.

the simulation.

Further confirmation of this is provided in Figure 5.9, , which shows the time evolution of the average values of the magnetic and electric field components for a resistive simulation without artificial dissipation (blue line), compared to the resistive simulations where artificial dissipation was applied either to the magnetic field alone (orange line) or to both the magnetic and electric fields (green line). As can be seen, there is a perfect overlap between the blue and orange lines, whereas the green line clearly diverges from the other two.

Having established that artificial dissipation should not be applied to the electric field, it is essential to verify that the same holds true for the magnetic field in the resistive regime. While Figure 5.9 suggests that artificial dissipation of the magnetic field is un-

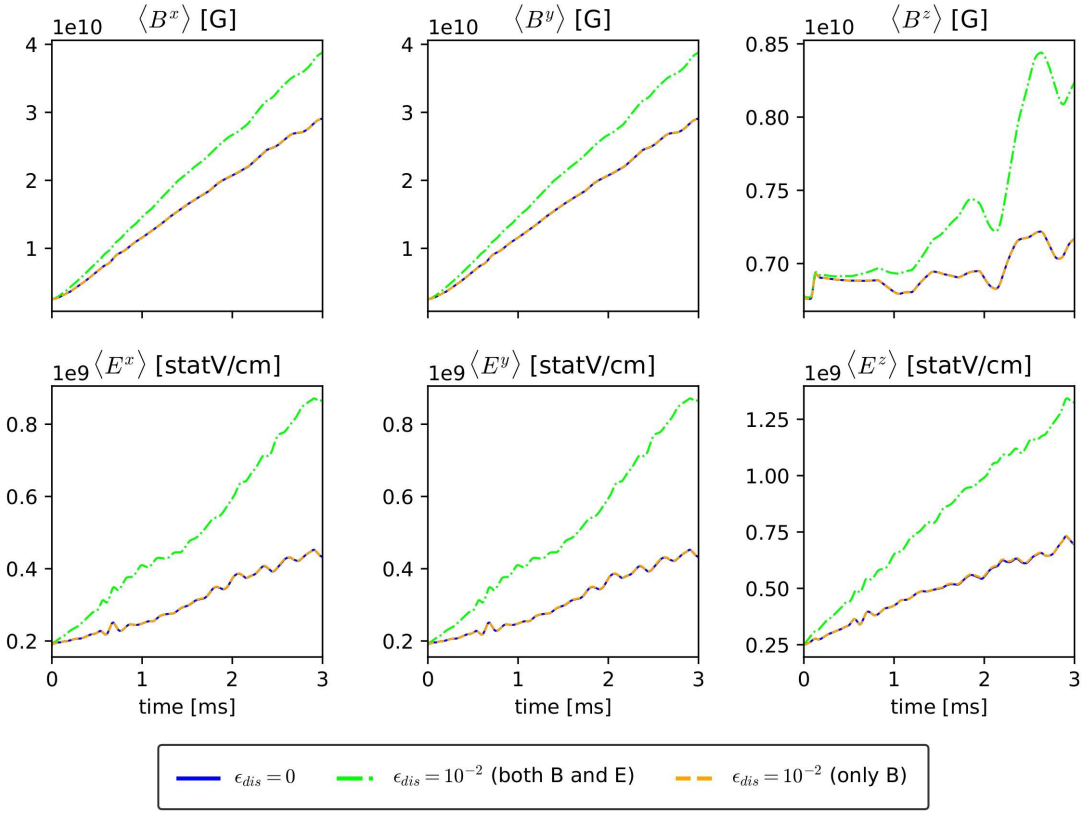

Figure 5.9: Comparison of resistive MHD simulation results for a magnetized rotating star with $\eta = 10^{-10}$. The blue line represents a simulation without artificial dissipation, while the lime and orange lines correspond to the same simulations as in Figure 5.8. Top row: components of the magnetic field in gauss. Bottom row: components of the electric field in statvolt per centimeter. Left column: $x-$component. Central column: $y-$component. Right column: $z-$component.

necessary, given the perfect overlap between the blue and orange lines, it is possible that this result is specific to our choice of dissipation parameter ϵ_{dis}. To further investigate this, we repeated the simulations for two distinct sets of values for η and ϵ_{dis}, applying artificial dissipation exclusively to the magnetic field. The results are illustrated in Figure 5.10, where the average values of the electric and magnetic fields components are reported. The blue line corresponds to the pair $(\eta, \epsilon_{dis}) = \left(10^{-10}, 10^{-2}\right)$, the orange line to the pair $(\eta, \epsilon_{dis}) = \left(10^{-3}, 10^{-5}\right)$, and the red line to the pair $(\eta, \epsilon_{dis}) = \left(10^{-3}, 10^{-2}\right)$. The orange and red lines overlap, showing that the results are unaffected by the artificial dissipation parameter. The difference from the blue line is due to resistivity. Thus, applying dissipation to the magnetic field alone is unnecessary in the resistive regime. Our results suggest that artificial dissipation is not required in the resistive regime. As

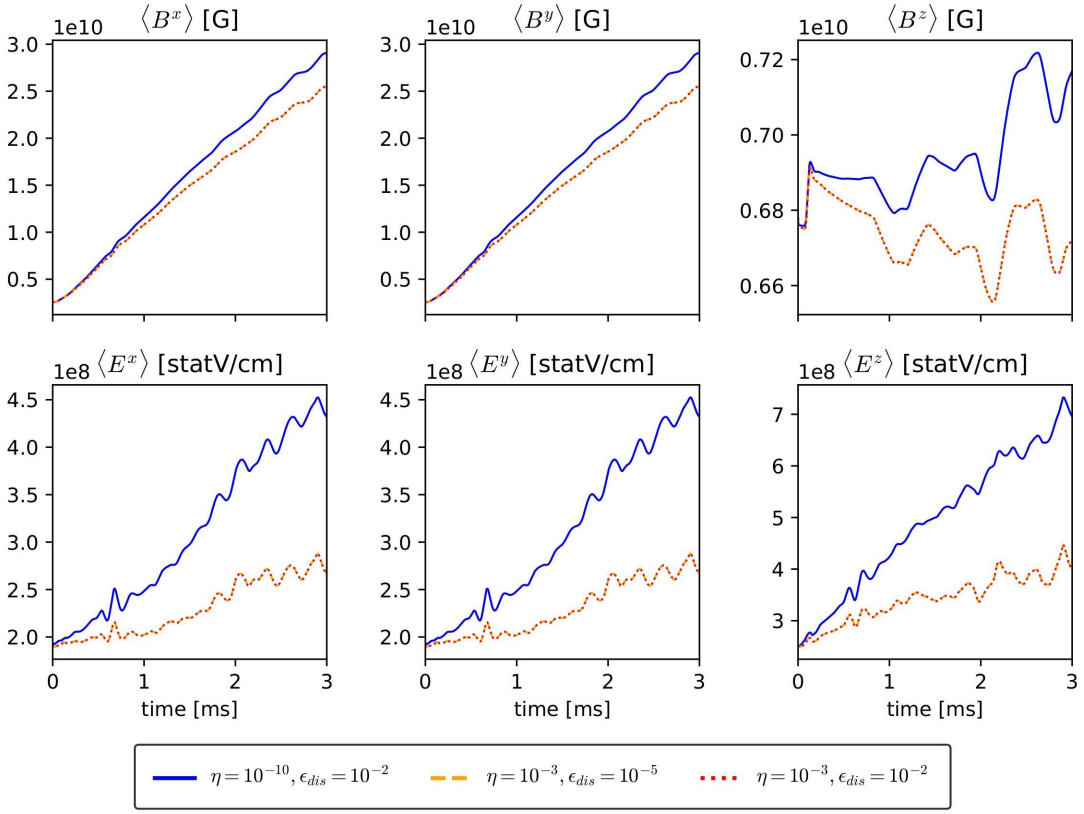

Figure 5.10: Comparison of simulation results for the magnetized rotating star in the resistive regime for different pairs (η, ϵ_{dis}) with artificial dissipation applied only to the magnetic field. Top row: components of the magnetic field in gauss. Bottom row: components of the electric field in statvolt per centimeter. Left column: $x-$component. Central column: $y-$component. Right column: $z-$component.

we will see later, the code converges smoothly without the need for artificial dissipation in the resistive regime, even in the presence of instabilities, in contrast to the ideal regime.

Starting from a 2D axisymmetric equilibrium configuration in the ideal regime and evolving the system on a 3D grid by introducing an additional term (artificial dissipation or resistivity) that was not initially present constitutes a perturbation to the system. This perturbation propagates through the numerical grid, influencing the density distribution. This is evident in the left panel of Figure 5.11, which shows the same as Figure 5.8 but for the density. The influence of the perturbation manifests as a peak at around 0.1 ms. Subsequently, the system relaxes, leading to the dissipation of this perturbation. Figure 5.11 further confirms that the addition of artificial dissipa-

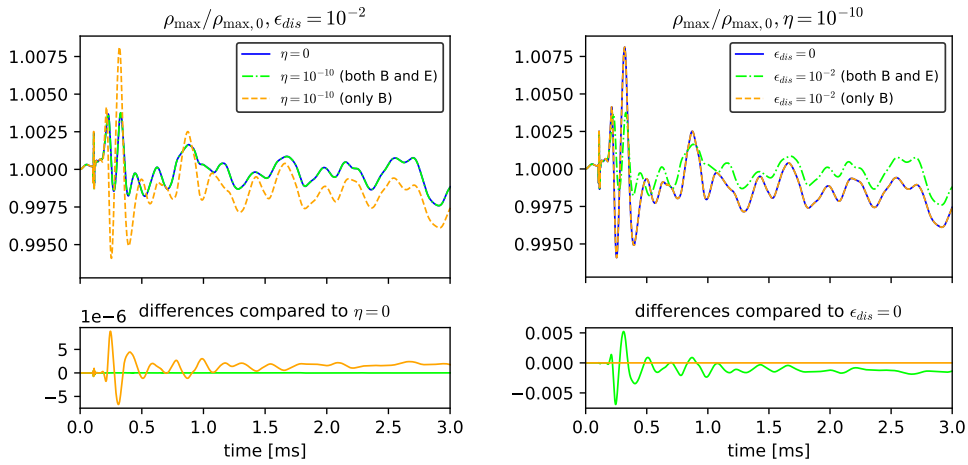

Figure 5.11: Time evolution of the maximum rest-mass density normalized to its initial value for magnetized rotating star simulations. Legend is the same as in Figure 5.8 (left panel) and Figure 5.9 (right panel).

tion is unnecessary in the resistive regime. In fact, the same matches observed for the components of the fields are evident here as well.

5.4 A physical application: bar-mode instability simulations in ideal and resistive regimes

With the successful validation of our code and the demonstration that artificial dissipation is redundant in the resistive regime, we are now able to present, to our knowledge, the first simulation results of bar-mode instability in a resistive regime.

The *bar-mode instability* is a physical phenomenon observed in rapidly rotating astrophysical objects, such as neutron stars or other compact stellar configurations. This type of instability arises when a self-gravitating body rotates fast enough to undergo non-spherical deformations. Specifically, bar-mode instability refers to the situation where an initially symmetric object becomes unstable and assumes an ellipsoidal or "bar-like" shape (hence the name "bar-mode"), rather than maintaining its axial symmetry.

The phenomenon is closely related to the rotational conditions of the system. When the rotational velocity of a self-gravitating body exceeds a certain critical limit, the centrifugal force becomes dominant over the gravitational force that maintains the object in equilibrium, leading to deformation. The instability can be analyzed through the development of perturbations of the equilibrium configuration. A key characteristic of the bar-mode instability is the transition from spherical or quasi-spherical symmetry to an elongated or elliptical shape resembling a "bar", with the principal axes of deformation

aligning in a way that lowers the system's energy.

Theoretically, this phenomenon has been extensively studied in astrophysics, both through analytical methods and numerical simulations, as it has significant implications for the stability of dense, rapidly rotating systems. Bar-mode instability can lead to the emission of gravitational waves, as the change in shape results in a variation in the mass quadrupole of the system, which is the primary source of gravitational waves. For this reason, such phenomena are of particular interest to astronomers studying gravitational waves, as they may provide valuable insights into the internal structure and dynamics of neutron stars or other rotating compact objects.

A central element in understanding bar-mode instability is the parameter β, which represents the ratio of rotational kinetic energy to the total gravitational energy of the body. If this parameter exceeds a certain critical value, typically around 0.24 (in general relativity or 0.27 in Newtonian gravity), the system becomes unstable to bar-mode type perturbations. Below this threshold, the system remains stable and tends to maintain a symmetric shape. However, when this critical threshold is reached or exceeded, centrifugal forces begin to dominate, and the body may undergo a transition to an elongated or distorted configuration.

Bar-mode instability has been observed in various simulations of neutron stars and binary systems (e.g., Shibata et al. 2000, Baiotti et al. 2007, Cerdá-Durán et al. 2007, Franci et al. 2013, Passamonti and Andersson 2020, Iosif and Stergioulas 2021, Löffler et al. 2015, De Pietri et al. 2014, Corvino et al. 2010, Manca et al. 2007), providing a unique window into understanding the processes that govern the dynamics and stability of these objects under extreme conditions.

The bar-mode instability, by breaking axial symmetry and inducing non-axisymmetric deformations, could create the necessary conditions to favor the action of a dynamo. The deformations resulting from the bar-mode instability generate plasma motions within the celestial body. These motions, in turn, can "stretch" and "twist" the lines of the pre-existing magnetic field, thereby enhancing its intensity. A more intense magnetic field further influences plasma motion, thereby generating a self-reinforcing cycle that can lead to the formation of a large-scale magnetic field.

5.4.1 Initial data

The initial configuration, built using the `XNS` code, was based on the magnetized U13 model presented in Franci et al. 2013. This is an unstable configuration that extends the sequence of models presented in Stergioulas et al. 2004 and Dimmelmeier et al. 2006. It consisted of a polytropic star with adiabatic index $\Gamma = 2$, polytropic constant $K = 100$, and initial central rest-mass density $\rho_c = 0.599 \times 10^{-4}$. The star exhibited differential rotation, characterized by the traditional constant specific angular momentum law ("j-constant" or KHE law; e.g., Komatsu et al. 1989, Friedman and Stergioulas 2013)

$$j = A^2(\Omega_c - \Omega) \tag{5.9}$$

where A is a positive constant, and Ω_c is the central rotation rate. Differential rotation was essential, as a considerable amount of it was required to achieve the large angular momentum necessary to trigger the dynamical bar-mode instability. Therefore, we have set

$$\Omega_c = 1.8 \times 10^{-2} \simeq 3654\,\mathrm{rad/s} \tag{5.10}$$

and $A^2 = 500$, resulting in a polar-to-equatorial ratio of $r_p/r_e = 0.200$. The resulting star - with a mass of $M \simeq 1.5\,\mathrm{M}_\odot$ and equatorial radius of

$$r_e = 22.55 \simeq 33.30\,\mathrm{km} \tag{5.11}$$

- is stable against gravitational collapse according to Giacomazzo et al. 2011b. A purely toroidal vector potential A_ϕ, given by

$$A_\phi = A_b(\max\{p - p_{cut}, 0\})^2 \tag{5.12}$$

where p_{cut} was 4% of the maximum pressure, and A_b was chosen to have a maximum magnetic field on the order of 10^9 gauss, was added to the initial equilibrium models to introduce an initial poloidal magnetic field perturbation, while the initial electric field was set equal to the IMHD value. The simulation was carried out for 25 ms. For the ideal regime, simulations were performed with $\epsilon_{dis} = 0.1$ (as in Franci et al. 2013) and $\epsilon_{dis} = 0.05$. For the resistive regime, simulations were run with $\eta = 10^{-12}$, $\eta = 10^{-9}$, $\eta = 10^{-6}$, and $\eta = 10^{-3}$. The lowest value corresponds to

$$\eta = 10^{-12} \simeq 5.0 \times 10^{-18}\,\mathrm{s} \simeq 5.6 \times 10^{-7}\,\Omega \cdot \mathrm{m} \tag{5.13}$$

whereas the value $\eta = 10^{-6}$ corresponds to the electrical resistivity at the base of the lower solar atmosphere (Chae and Litvinenko 2021).

5.4.2 Magnetic field decomposition

To gain a deeper understanding of the magnetic field's influence on bar-mode instability dynamics, we have augmented our diagnostic variables to quantify and characterize the magnetic field's evolution explicitly. In axisymmetric configurations, the magnetic field is typically decomposed into toroidal and poloidal components for separate analysis. However, when axisymmetry is broken, this straightforward decomposition is no longer available. Despite the loss of axisymmetry, there is still a useful decomposition that can be defined, one which reduces to the traditional poloidal-toroidal form in the axisymmetric and stationary case. The key idea behind this decomposition is to separate the magnetic field into components that are aligned with and perpendicular to the fluid motion. For an Eulerian observer, we can split the magnetic field as

$$\mathbf{B} = \mathbf{B}_\perp + \mathbf{B}_\parallel = \mathbf{B}_\perp + B_\parallel \frac{\mathbf{v}}{\|\mathbf{v}\|} \tag{5.14}$$

where the "perpendicular" component, $\mathbf{B}_\perp$, is defined by the condition

$$\mathbf{B}_\perp \cdot \mathbf{v} = 0 \tag{5.15}$$

and the "parallel" component, $B_\parallel$, is a scalar, simply defined as

$$\mathbf{B}_\parallel := \frac{\mathbf{B} \cdot \mathbf{v}}{\|\mathbf{v}\|} \tag{5.16}$$

Initially, when the flow is predominantly azimuthal, $\mathbf{B}_\perp$ corresponds to the poloidal component of the magnetic field, and $\mathbf{B}_\parallel$ represents the toroidal component. Throughout the analysis, we will refer to these as the "poloidal" and "toroidal" components, respectively, though this terminology is used loosely outside of strictly axisymmetric configurations.

5.4.3 Bar deformation diagnostics

An important set of diagnostic quantities focuses on detecting bar deformations, which can be conveniently quantified in terms of the distortion parameters given by (Saijo et al. 2001, Franci et al. 2013)

$$H_+ = \frac{I^{xx} - I^{yy}}{I^{xx} + I^{yy}} \tag{5.17}$$

$$H_\times = \frac{2I^{xy}}{I^{xx} + I^{yy}} \tag{5.18}$$

$$H = \sqrt{H_+^2 + H_\times^2} \tag{5.19}$$

The quadrupole moment of the matter distribution, I^{ij}, can be computed in terms of the conserved density D as

$$I^{jk} = \int \mathrm{d}^3x \sqrt{\gamma}\, D x^j x^k \tag{5.20}$$

It's important to note that all quantities in Equations (5.17) to (5.19) are expressed in terms of the coordinate time t. Therefore, they do not represent invariant measurements at spatial infinity. However, for the simulations presented here, the length-scale over which the lapse function varies at any given time consistently exceeds twice the stellar radius at that time. This condition guarantees that events occurring on the same time slice are also closely aligned in terms of proper time.

5.4.4 Results

Let's begin by analyzing the results of the simulations conducted in the ideal regime, represented by the blue lines (solid and dashed) in Figure 5.12, which illustrates the time evolution of the maximum values of the magnetic and electric field norms. The

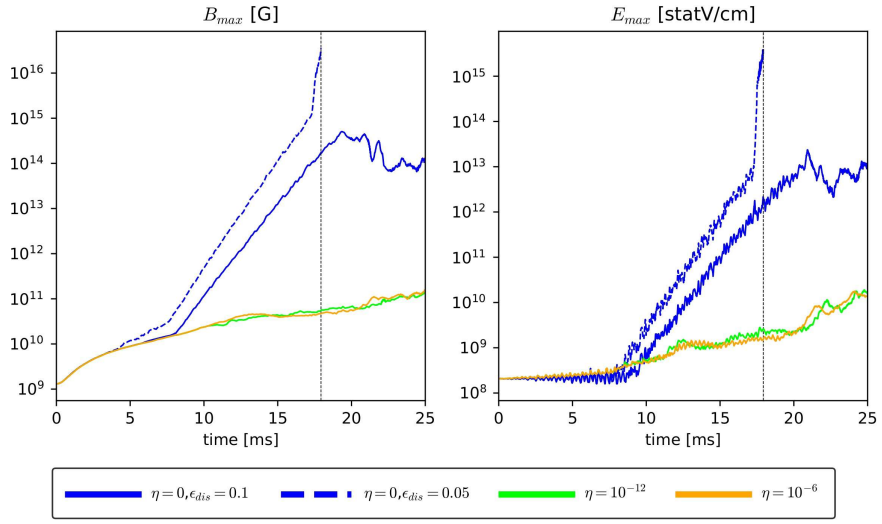

Figure 5.12: Results of the bar-mode instability simulations. Time evolution, in base-10 log scale, of the maximum values of the norms of the magnetic field (left) and the electric field (right). The black dotted vertical line indicates the time when the simulation $(\eta, \epsilon_{dis}) = (0, 0.05)$ failed.

blue solid line corresponds to the simulation with $\epsilon_{dis} = 0.1$, while the blue dashed line represents the simulation with $\epsilon_{dis} = 0.05$. As depicted in the left panel of Figure 5.12, a marked divergence between the two curves becomes evident from approximately 4 ms onwards. The simulation employing $\epsilon_{dis} = 0.05$ exhibits a more rapid growth of the magnetic field and experienced a premature termination at approximately 18 ms (black dotted vertical line), suggesting potential numerical instabilities. This value of ϵ_{dis} was, therefore, insufficient to dissipate the spurious oscillations arising from numerical errors. However, despite reaching a conclusion, the value $\epsilon_{dis} = 0.1$ was also unable to completely eliminate all numerical errors. As a result of numerical errors, the magnetic field exhibits an unphysical growth in regions close to the stellar surface, where it was initially zero and where no source terms are present. This phenomenon can be observed in the left columns of Figures 5.13 and 5.14, which display the spatial distributions on the $xz-$plane of the magnetic field (top row) and its poloidal component (bottom row) at 7 and 15 milliseconds, respectively. At 7 milliseconds, weak spurious fields begin to appear near the stellar surface, indicating the onset of numerical instability. At 15 milliseconds, during the exponential growth, these spurious fields have amplified significantly, and the maximum magnetic field strength is now located at the stellar surface, confirming the dominant role of numerical errors in the late-time evolution of the magnetic field. However, the exponential growth depicted in Figure 5.12 occurs not only for these spurious fields but also for the genuine magnetic field confined within the

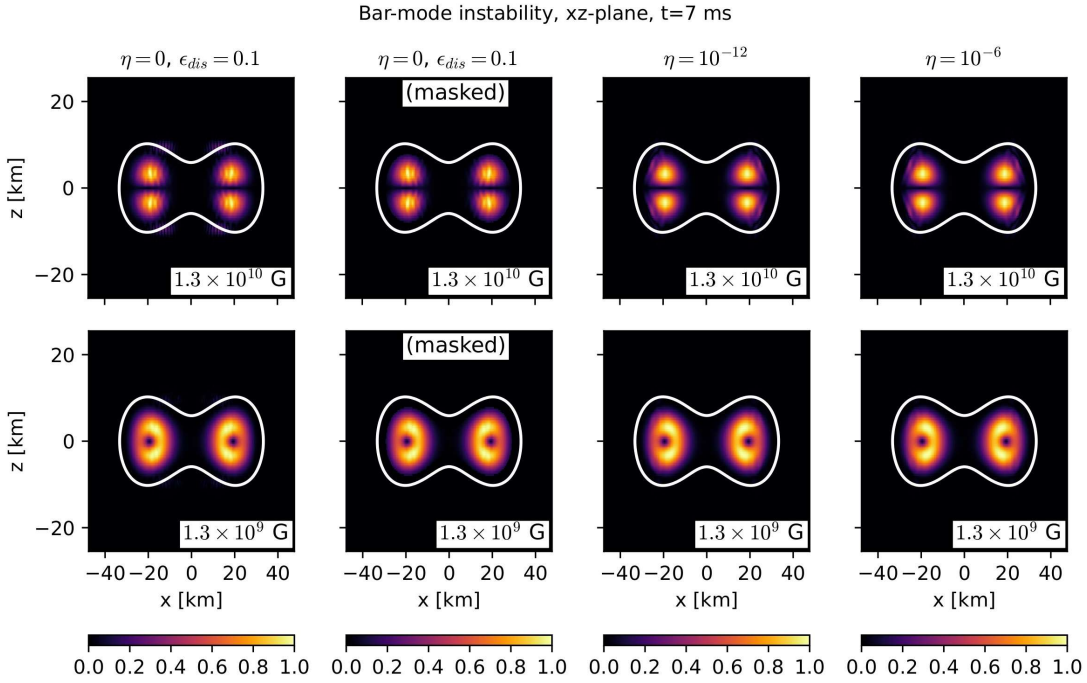

Figure 5.13: Results of the bar-mode instability simulations. Spatial distribution of the magnetic field norm (top row) and its poloidal component (bottom row) on the $xz-$plane at $t = 7\,\text{ms}$. The simulations include an Ideal MHD case with $\epsilon_{dis} = 0.1$ (first and second columns) and two resistive cases with $\eta = 10^{-12}$ (third column) and $\eta = 10^{-6}$ (fourth column). The second column shows the ideal simulation with the surface masked to reveal the internal field distribution. The values of the fields are normalized to their maximum value, displayed in the white box in the lower right corner.

star. This is illustrated in Figure 5.15, which shows the time evolution on the masked xz-plane (i.e., considering only the internal region of the star) of the maximum values of the norms of the magnetic field (left panel), its poloidal component (central panel), and the electric field (right panel). As depicted in Figure 5.16, the distortion parameter H also experiences exponential growth before saturating at approximately 20 ms, in accordance with Franci et al. 2013. This behavior is precisely what we expect from a stellar model that is unstable to the dynamical bar-mode instability (Baiotti et al. 2007).

Let us now focus on the electric field. As depicted in Figures 5.12 and 5.15, the electric field remains nearly constant for the first 7 to 8 milliseconds, before experiencing an exponential increase. This behavior is consistent with the ideal relation

$$\mathbf{E} = -\mathbf{v} \times \mathbf{B} = -\mathbf{v} \times \mathbf{B}_{\perp} \tag{5.21}$$

which links the electric field to the poloidal component of the magnetic field. Figure 5.15

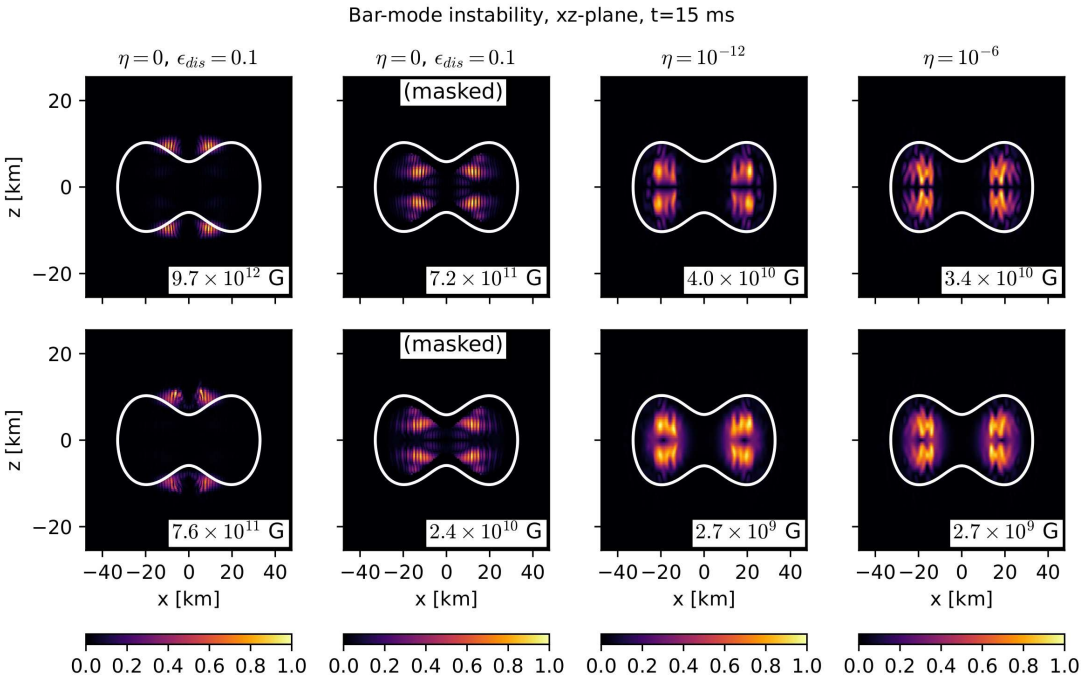

Figure 5.14: The same as Figure 5.13, but at $t = 15$ ms.

confirms that the poloidal component also remains constant until approximately 7-8 milliseconds, thus explaining the initial constancy of the electric field. Furthermore, this implies that the initial growth of the magnetic field is attributed to the formation and growth of a toroidal component.

In conclusion, the bar-mode instability appears to trigger the dynamo mechanism once axial symmetry has been broken. However, the results of the simulations in the ideal regime are highly dependent on the chosen value of the artificial dissipation parameter. This dependence is non-physical due to several reasons. First, in a physical context, the dynamics should not be sensitive to arbitrary parameters introduced to mitigate numerical instabilities. The choice of artificial dissipation should ideally not alter the fundamental behavior of the system being modeled. Second, as we have observed, the presence of spurious oscillations indicates that the numerical scheme may not accurately capture the true dynamics, leading to misleading results.

We now turn our attention to the results of the resistive simulations with $\eta = 10^{-12}$ and $\eta = 10^{-6}$. As shown in Figures 5.12 and 5.15, the fields exhibit significant damping. This is consistent with the findings of Dionysopoulou et al. 2015 for the post-merger phase of a binary neutron star system in a resistive regime with $\eta = 10^{-6}$. Furthermore, the electrical resistivity has successfully mitigated numerical errors near the stellar surface, as can be seen in Figures 5.13 and 5.14 (third and fourth panels).

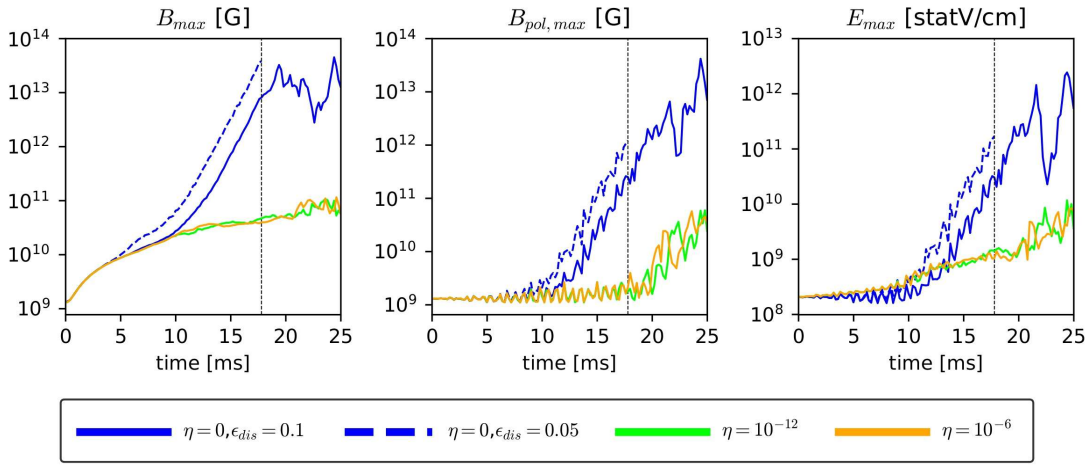

Figure 5.15: Results of the bar-mode instability simulations. Time evolution, in base-10 log scale and on the masked xz-plane (i.e., considering only the internal region of the star), of the maximum values of the norms of the magnetic field (left), its poloidal component (center), and the electric field (right). The black dotted vertical line indicates the time when the simulation $(\eta, \epsilon_{dis}) = (0, 0.05)$ failed.

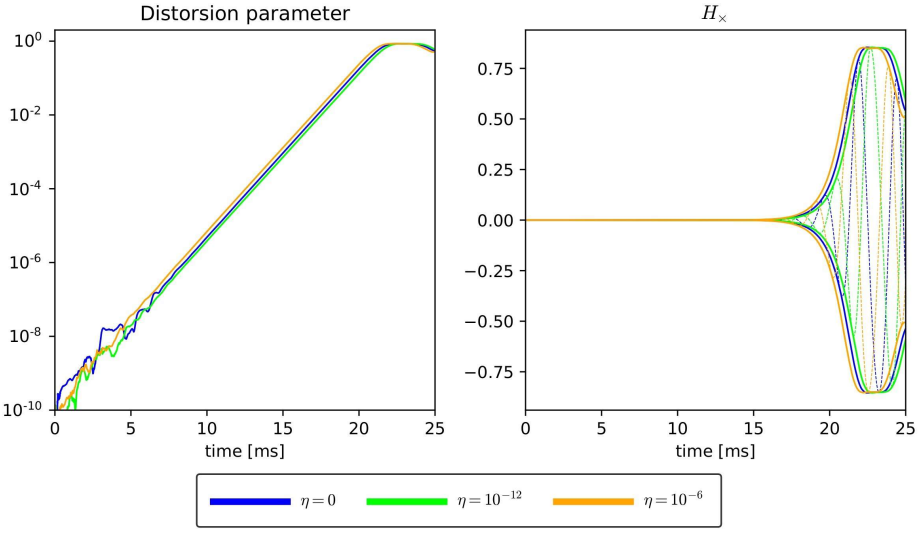

Figure 5.16: Results of the bar-mode instability simulations. Time evolution of the distortion parameters H (left panel; base-10 log scale) and $H_\times$ (right panel) in both Ideal and resistive regimes. In the right panel, dashed lines represent the $H_\times$ parameter, while solid line the distortion parameter H.

Additionally, the fact that these simulations did not require artificial dissipation is

further confirmation of the results obtained in previous tests. However, it is noteworthy that there are no significant differences observed between the results of the resistive simulations when varying η, even when considering the results of simulations with $\eta = 10^{-9}$ and $\eta = 10^{-3}$, which are not shown here. The chosen functional relationship for η (i.e., constant within the star) may be a contributing factor, as it remains the same at every point in the star, regardless of the local density. However, we do not have sufficient information to confirm this hypothesis, and other reasons cannot be ruled out. Future studies will be conducted to investigate the underlying causes.

It is noteworthy that the distortion parameter remains insensitive to variations in η. In fact, it proves to be unaffected by the regime in which the simulation was conducted (Figure 5.16). This implies that the fluid component evolves identically regardless of the considered regime, further corroborating the results of Dionysopoulou et al. 2015, which demonstrate that the evolution of the maximum density is unaffected by the simulation regime up until shortly before the collapse into a black hole.

Conclusions

This thesis presents a new numerical code, named `MIR`, designed to simulate the time evolution of complex astrophysical systems, with a particular focus on magnetohydrodynamic phenomena. Based on the general relativistic magnetohydrodynamics (MHD) equations in the 3+1 formalism (Alcubierre 2008, Baumgarte and Shapiro 2010, Gourgoulhon 2012), the code can operate in three distinct regimes: purely hydrodynamic, Ideal MHD, and resistive MHD. Developed within the Einstein Toolkit framework (Löffler et al. 2012), the code represents a significant advancement in the numerical study of these systems, as it is the first publicly available resistive code within this powerful platform. The inclusion of the resistive regime enables a more realistic investigation of various astrophysical phenomena compared to previous codes, which were limited to the hydrodynamic and ideal MHD regimes.

The study of electromagnetic fields in astrophysical sources is of fundamental importance for understanding numerous processes of cosmic relevance. Magnetic fields, in particular, play a crucial role in various astrophysical phenomena, including the accretion of matter onto black holes and neutron stars, the triggering of powerful relativistic jets, and the evolution of accretion disks. In the ideal regime, magnetohydrodynamics assumes that magnetic fields and matter are tightly coupled, without energy dissipation due to electrical resistance. However, this assumption is often unrealistic, as resistive effects are present in many astrophysical contexts, allowing for magnetic reconnection, energy dissipation, and the conversion of magnetic energy into thermal and kinetic energy. These processes underlie phenomena such as solar flares, gamma-ray bursts, and other highly energetic observable events.

Incorporating resistive terms into our numerical code enables more accurate simulations of these phenomena, offering a more complete representation of the underlying physics. The capability to model magnetic reconnection and other magnetic instabilities allows us to investigate how magnetic field evolution influences the system's overall dynamics and observable emission. This can aid in interpreting data from astrophysical observations, thereby expanding our understanding of complex phenomena.

The inclusion of electrical resistivity introduces two significant differences compared to the ideal case. First, it necessitates the evolution of the electric field as well, adding three new equations (one for each component) to the system. Second, it requires the use of so-called *IMEX schemes* (Pareschi and Russo 2005, Palenzuela et al. 2009), which combine implicit and explicit methods. This entails two substantial modifications. The first modification is that the right-hand side (RHS) of the equations comprising our system must be split into two parts, a *stiff* and a *non-stiff* part, complicating the *method of lines* (MoL). The second modification involves the evolved variables (also known as *conserved* or *conservative* variables) that exhibit stiff terms in their RHS. These variables undergo an implicit step during the recovery of the so-called *primitive* variables (those that describe a system from a physical perspective, such as density, pressure, velocity, and so on). This implicit step significantly complicates the conversion from conservative to primitive variables.

The code has been rigorously tested against a suite of standard benchmarks in one, two, and three dimensions, demonstrating a robust capability to solve complex problems. It has consistently exhibited stability and accuracy, even under demanding physical conditions. These benchmarks, well-established in the literature, have been employed to validate the code's implementation by comparing its results against existing solutions. The high accuracy achieved confirms the robustness of the numerical method and the reliability of the code in handling resistive scenarios. Our numerical results have also validated theoretical expectations, demonstrating that the resistive regime does not necessitate the introduction of artificial dissipation. This finding contrasts with the ideal regime, where artificial viscosity is essential to suppress spurious numerical oscillations that naturally arise in ideal simulations.

A significant result of this thesis work is the first study of bar-mode instability in the resistive regime. The inclusion of resistivity effects has enabled the exploration of new scenarios beyond those considered in previous studies, which were limited to the ideal regime. This critical dependence renders the results obtained in this regime particularly challenging to interpret, as even small variations in the dissipation parameter can lead to qualitatively different outcomes, including simulation failure. The difficulty in determining an optimal value for the artificial viscosity, capable of damping spurious numerical oscillations without compromising the underlying physics, represents an intrinsic limitation of such simulations. While resistive simulations have effectively suppressed spurious oscillations, our findings indicate that varying the electrical resistivity does not substantially alter the simulation outcomes. The reasons for this unexpected behavior remain unclear, as we lack sufficient information to make definitive statements, and warrant further investigation. The assumption of a constant electrical resistivity, independent of density, may limit the model's ability to capture the complex physics of stellar interiors. Additional studies are required to explore more sophisticated resistivity models and to assess their impact on simulation outcomes.

Future work will focus on extending the code to incorporate tabulated equations of

state for simulating fluids with complex properties. We also aim to utilize the `MIR` code to study binary neutron star mergers in the resistive regime, investigating the impact of non-ideal effects on post-merger remnants and associated electromagnetic and gravitational emissions. Finally, we aim to propose the inclusion of the `MIR` code in future releases of the Einstein Toolkit framework for broader accessibility and utilization.

The code used in this thesis, including the updated `MoL` thorn with the IMEX SSP2(2,2,2) scheme, is open-source and available for download, enabling researchers to build upon our work and explore further applications.

Download

The MIR code is publicly available on Zenodo (Franceschetti and De Pietri 2024b) at the following link:

https://doi.org/10.5281/zenodo.13986384

In addition to the MIR code, the downloaded folder contains two essential thorns: ElectroBase (which defines the variables necessary for the evolution of the electric field) and MIR_InitData (used to configure the initial conditions). The downloaded folder also includes updated files for the MoL thorn, featuring the newly implemented IMEX SSP2(2,2,2) scheme. Thorough reading of the README and CHANGELOG files is strongly recommended before utilizing this software.

To access the comprehensive documentation for the code and thorns, please visit:

https://einstein.pr.infn.it/gravity/MIR/doc/intro.html

Appendix A

Implementation of the SSP2(2,2,2) scheme in the Einstein Toolkit framework

By default, the `MoL` thorn included in the Einstein Toolkit requires the registration of only one RHS. However, the IMEX-RK scheme described in Section 4.5.1 requires splitting the RHS into two distinct terms and, therefore, the registration of two RHSs.

As shown in Section 4.5.1, the set of Equation (4.1) can be rewritten as

$$\partial_t \boldsymbol{\mathcal{U}} = \boldsymbol{\mathcal{Q}} + \boldsymbol{\mathcal{R}} = \boldsymbol{\mathcal{L}} \tag{A.1}$$

where $\boldsymbol{\mathcal{U}}$ is the vector of conserved variables, $\boldsymbol{\mathcal{Q}}$ is the RHS without stiff terms (including the flux terms), $\boldsymbol{\mathcal{R}}$ is the stiff term of the RHS, and $\boldsymbol{\mathcal{L}}$ is the total RHS.

In this appendix, we present the implementation of the SSP2(2,2,2) scheme (Pareschi and Russo 2005, Palenzuela et al. 2009), whose Butcher tableau (Butcher 1987) is shown in Table A.1, in the `MoL` thorn. This implementation uses so-called scratch variables, i.e., temporary variables defined within `MoL` itself, which we will denote as $\overline{\boldsymbol{\mathcal{U}}}$.

For the SSP2(2,2,2) scheme, the following three steps are required (one more than the second-order Runge-Kutta method):

- For $i = 1$ only the implicit step is needed. Then the explicit step performed by the `MoL` results to be

$$\boldsymbol{\mathcal{U}}_*^{(1)} = \boldsymbol{\mathcal{U}}^n \qquad \overline{\boldsymbol{\mathcal{U}}}^{(1)} = \mathbf{0} \tag{A.2}$$

  and the implicit step is

$$\boldsymbol{\mathcal{U}}^{(1)} = \boldsymbol{\mathcal{U}}_*^{(1)} + \gamma \Delta t \boldsymbol{\mathcal{R}}_1 \tag{A.3}$$

- For $i = 2$ the explicit step is

$$\boldsymbol{\mathcal{U}}_*^{(2)} = 3\boldsymbol{\mathcal{U}}^n - 2\boldsymbol{\mathcal{U}}^{(1)} + \Delta t \boldsymbol{\mathcal{L}}_1 \qquad \overline{\boldsymbol{\mathcal{U}}}^{(2)} = \frac{\Delta t}{2} \boldsymbol{\mathcal{L}}_1 \tag{A.4}$$

  and the implicit step is

$$\boldsymbol{\mathcal{U}}^{(2)} = \boldsymbol{\mathcal{U}}_*^{(2)} + \gamma \Delta t \boldsymbol{\mathcal{R}}_2 \tag{A.5}$$

$$\begin{array}{c|cc} 0 & 0 & 0 \\ 1 & 1 & 0 \\ \hline & 1/2 & 1/2 \end{array} \qquad \begin{array}{c|cc} \gamma & \gamma & 0 \\ 1-\gamma & 1-2\gamma & \gamma \\ \hline & 1/2 & 1/2 \end{array} \qquad \gamma = 1 - \frac{1}{\sqrt{2}}$$

Table A.1: Tableau for the explicit (left) implicit (right) IMEX-SSP2(2,2,2) L-stable scheme (Pareschi and Russo 2005, Palenzuela et al. 2009).

- The third and final step is

$$\boldsymbol{\mathcal{U}}_*^{(3)} = \boldsymbol{\mathcal{U}}^n + \overline{\boldsymbol{\mathcal{U}}}^{(2)} + \frac{\Delta t}{2}\boldsymbol{\mathcal{L}}_2 \tag{A.6}$$

$$\boldsymbol{\mathcal{U}}^{n+1} = \boldsymbol{\mathcal{U}}_*^{(3)} \tag{A.7}$$

Here, $\boldsymbol{\mathcal{U}}_*^{(i)}$ is the value of the conserved variable $\boldsymbol{\mathcal{U}}$ returned by the `MoL` thorn after the i-th explicit step. Note that since $\boldsymbol{\mathcal{R}}_i$ depends on $\boldsymbol{\mathcal{U}}^{(i)}$, the implicit step must be carried out during the inversion from conservative to primitive variables by `MIR`. With this scheme, we can register only the total RHS $\boldsymbol{\mathcal{L}}$, allowing us to use the existing structure of the `MoL` thorn without requiring significant modifications.

Appendix B

Upper limit for the conserved momentum

Equations (4.53) and (4.55) represent, respectively, the maximum values that the total conserved momentum ($\mathbf{S}$) and the fluid conserved momentum ($\mathbf{M} = DhW\mathbf{v}$) can attain in the most general case possible, namely the resistive magnetized case. In this appendix, we will derive these upper limits.

B.1 Maximum for M

Recall that the total momentum is defined as

$$\mathbf{S} = \mathbf{M} + \mathbf{E} \times \mathbf{B} \tag{B.1}$$

From this equation we have

$$S^2 = M^2 + \|\mathbf{E} \times \mathbf{B}\|^2 + 2\mathbf{M} \cdot (\mathbf{E} \times \mathbf{B}) \tag{B.2}$$

therefore

$$S^2 \geq M^2 + 2\mathbf{M} \cdot (\mathbf{E} \times \mathbf{B}) \tag{B.3}$$

Now consider Equation (4.70). By taking the cross product with $\mathbf{B}$ and then the dot product with $\mathbf{M}$, we obtain

$$\mathbf{M} \cdot (\mathbf{E} \times \mathbf{B}) = A_0 \mathbf{M} \cdot (\mathbf{E}_* \times \mathbf{B}) + A_1 DhW \|\mathbf{v} \times \mathbf{B}\|^2 \geq A_0 \mathbf{M} \cdot (\mathbf{E}_* \times \mathbf{B}) \tag{B.4}$$

where we recall that the coefficients $A_0 > 0$ and $A_1 > 0$ are given by Equations (4.46) and (4.47), respectively. Given that

$$\mathbf{M} \cdot (\mathbf{E}_* \times \mathbf{B}) \geq -E_* BM \tag{B.5}$$

the previous inequality becomes

$$\mathbf{M} \cdot (\mathbf{E} \times \mathbf{B}) \geq -A_0 E_* BM \tag{B.6}$$

Furthermore, given that $A_0 \leq A_{0,\max}$ - which implies $-A_0 \geq -A_{0,\max}$, with $A_{0,\max}$ given by Equation (4.56) - it follows that

$$\mathbf{M} \cdot (\mathbf{E} \times \mathbf{B}) \geq -A_{0,\max} E_* B M \tag{B.7}$$

The inequality (B.3) thus becomes

$$M^2 - 2A_{0,\max} B E_* M - S^2 \leq 0 \tag{B.8}$$

Solving it for M, we obtain Equation (4.55).

B.2 Maximum for S

If the dominant energy condition holds - i.e. if $p^2 \leq \rho^2(1+\epsilon)^2$ - one has (Etienne et al. 2012)

$$M^2 \leq \mathcal{E}_F^2 \tag{B.9}$$

where we recall that

$$\mathcal{E}_F = \mathcal{E} - U_{em} \geq 0 \tag{B.10}$$

is the conserved fluid energy, with $\mathcal{E} \geq 0$ the total conserved energy and $U_{em} \geq 0$ the electromagnetic energy density. From this relation follows that

$$\mathcal{E}_F \leq \mathcal{E} \Longrightarrow \mathcal{E}_F^2 \leq \mathcal{E}^2 \tag{B.11}$$

therefore

$$M^2 \leq \mathcal{E}^2 \tag{B.12}$$

As a result, inequality (B.2) can be rewritten as

$$S^2 \leq \mathcal{E}^2 + \|\mathbf{E} \times \mathbf{B}\|^2 + 2\mathbf{M} \cdot (\mathbf{E} \times \mathbf{B}) \tag{B.13}$$

Since

$$\|\mathbf{E} \times \mathbf{B}\|^2 \leq E^2 B^2 \tag{B.14}$$

and

$$\mathbf{M} \cdot (\mathbf{E} \times \mathbf{B}) \leq M \|\mathbf{E} \times \mathbf{B}\| \leq MEB \leq \mathcal{E}EB \tag{B.15}$$

the previous inequality becomes

$$S^2 \leq \mathcal{E}^2 + E^2 B^2 + 2\mathcal{E}EB \tag{B.16}$$

From the definition of the electromagnetic energy density we have

$$E^2 = 2U_{em} - B^2 \leq 2U_{em} \tag{B.17}$$

But

$$U_{em} = \mathcal{E} - \mathcal{E}_F \leq \mathcal{E} \tag{B.18}$$

therefore

$$E^2 \leq 2\mathcal{E} \tag{B.19}$$

As a result, we have

$$S^2 \leq \mathcal{E}^2 + 2\mathcal{E}B\sqrt{2\mathcal{E}} + 2\mathcal{E}B^2 = \left(\mathcal{E} + B\sqrt{2\mathcal{E}}\right)^2 \tag{B.20}$$

that is Equation (4.53).

Appendix C

Computing the electric charge using a Riemann solver

As discussed in Chapter 4, computing divergences necessitates the use of a Riemann solver. To accomplish this, it is essential to reconstruct both the flux terms and the corresponding conserved variables at both sides of the cell interfaces. However, the Maxwell equation for electric charge

$$q = \boldsymbol{\nabla} \cdot \mathbf{E} \tag{C.1}$$

does not involve any time derivatives of conserved variables. Consequently, electric charge is typically computed using finite difference methods. "In this appendix, we prove that it is possible to use a Riemann solver for electric charge, with the conserved variable set to zero.

In the 3+1 formalism, Equation (3.7) becomes

$$\nabla_\mu F^{\mu\nu} = -qn^\nu - J^\nu \tag{C.2}$$

The time projection gives

$$\gamma^{-1/2}\partial_\mu(\sqrt{\gamma}\, E^\mu) = q \tag{C.3}$$

that is

$$\partial_t\big(\sqrt{\gamma}\, E^0\big) + \partial_i\big(\sqrt{\gamma}\, E^i\big) = \sqrt{\gamma}\, q \tag{C.4}$$

Since $E^0 = 0$, we have

$$\partial_t 0 + \partial_i\big(\sqrt{\gamma}\, E^i\big) = \sqrt{\gamma}\, q \tag{C.5}$$

Since $\partial_t 0 = 0$ we obtain Equation (C.1). However, Equation (C.5) can be interpreted as the equation governing the evolution of the conserved variable $\boldsymbol{\mathcal{U}} = \mathbf{0}$. Consequently, we can compute the spatial derivative ∂_i using a Riemann solver with $\boldsymbol{\mathcal{U}}^i_{R,j} = \boldsymbol{\mathcal{U}}^i_{L,j} = 0$.

The same argument can be made for the computation of the divergence of the magnetic field.

Bibliography

[Aasi et al. 2015] Aasi J. et al. "Advanced LIGO". *Classical and Quantum Gravity* 32.7, (2015), p. 074001. DOI: 10.1088/0264-9381/32/7/074001. URL: https://dx.doi.org/10.1088/0264-9381/32/7/074001.

[Abbott et al. 2016] Abbott B. P. et al. "Observation of Gravitational Waves from a Binary Black Hole Merger". *Phys. Rev. Lett.* 116, (6 2016), p. 061102. DOI: 10.1103/PhysRevLett.116.061102. URL: https://link.aps.org/doi/10.1103/PhysRevLett.116.061102.

[Abbott et al. 2017a] Abbott B. P. et al. "GW170814: A Three-Detector Observation of Gravitational Waves from a Binary Black Hole Coalescence". *Phys. Rev. Lett.* 119, (14 2017), p. 141101. DOI: 10.1103/PhysRevLett.119.141101. URL: https://link.aps.org/doi/10.1103/PhysRevLett.119.141101.

[Abbott et al. 2017b] Abbott B. P. et al. "GW170817: Observation of Gravitational Waves from a Binary Neutron Star Inspiral". *Phys. Rev. Lett.* 119, (16 2017), p. 161101. DOI: 10.1103/PhysRevLett.119.161101. URL: https://link.aps.org/doi/10.1103/PhysRevLett.119.161101.

[Abbott et al. 2017c] Abbott B. P. et al. "Multi-messenger Observations of a Binary Neutron Star Merger". *The Astrophysical Journal Letters* 848.2, (2017), p. L12. DOI: 10.3847/2041-8213/aa91c9. URL: https://dx.doi.org/10.3847/2041-8213/aa91c9.

[Acernese et al. 2015] Acernese F. et al. "Advanced Virgo: a second-generation interferometric gravitational wave detector". *Classical and Quantum Gravity* 32.2, (2015), p. 024001. DOI: 10.1088/0264-9381/32/2/024001. URL: https://dx.doi.org/10.1088/0264-9381/32/2/024001.

[Acheson and Hide 1973] Acheson D. J. and Hide R. "Hydromagnetics of rotating fluids". *Reports on Progress in Physics* 36.2, (1973), p. 159. DOI: 10.1088/0034-4885/36/2/002. URL: https://dx.doi.org/10.1088/0034-4885/36/2/002.

[Akiyama et al. 2019] Akiyama K. et al. "First M87 Event Horizon Telescope Results. IV. Imaging the Central Supermassive Black Hole". *ApJL* 875.1, (2019), p. L1. DOI: 10.3847/2041-8213/ab0e85. URL: https://doi.org/10.3847/2041-8213/ab0e85.

[Alcubierre 2008] Alcubierre Miguel. *Introduction to 3+1 Numerical Relativity*. Oxford University Press, 2008. DOI: 10.1093/acprof:oso/9780199205677.001.0001. URL: https://doi.org/10.1093/acprof:oso/9780199205677.001.0001.

[Armitage 2022] Armitage Philip. *Lecture notes on accretion disk physics*. 2022. DOI: 10.48550/arXiv.2201.07262.

[Baade and Zwicky 1934] Baade W. and Zwicky F. "Remarks on Super-Novae and Cosmic Rays". *Phys. Rev.* 46, (1 1934), pp. 76–77. DOI: 10.1103/PhysRev.46.76.2. URL: https://link.aps.org/doi/10.1103/PhysRev.46.76.2.

[Bailes et al. 2021] Bailes M. et al. "Gravitational-wave physics and astronomy in the 2020s and 2030s". *Nat Rev Phys* 3, (2021). DOI: 10.1038/s42254-021-00303-8.

[Baiotti and Rezzolla 2017] Baiotti Luca and Rezzolla Luciano. "Binary neutron star mergers: a review of Einstein's richest laboratory". *Rept. Prog. Phys.* 80.9, (2017), p. 096901. DOI: 10.1088/1361-6633/aa67bb. arXiv: 1607.03540 [gr-qc].

[Baiotti et al. 2007] Baiotti Luca et al. "Accurate simulations of the dynamical bar-mode instability in full general relativity". *Phys. Rev. D* 75, (4 Feb. 2007), p. 044023. DOI: 10.1103/PhysRevD.75.044023. URL: https://link.aps.org/doi/10.1103/PhysRevD.75.044023.

[Balbus and Hawley 1991] Balbus Steven A. and Hawley John F. "A Powerful Local Shear Instability in Weakly Magnetized Disks. I. Linear Analysis". *ApJ* 376, (1991), p. 214. DOI: 10.1086/170270.

[Baumgarte and Shapiro 2010] Baumgarte Thomas W. and Shapiro Stuart L. *Numerical Relativity: Solving Einstein's Equations on the Computer*. Cambridge University Press, 2010. DOI: 10.1017/CBO9781139193344.

[Bekenstein and Oron 1978] Bekenstein Jacob D. and Oron Eliezer. "New conservation laws in general-relativistic magnetohydrodynamics". *Phys. Rev. D* 18, (6 1978), pp. 1809–1819. DOI: 10.1103/PhysRevD.18.1809. URL: https://link.aps.org/doi/10.1103/PhysRevD.18.1809.

[Biskamp 1997] Biskamp Dieter. *Nonlinear Magnetohydrodynamics*. Cambridge University Press, 1997.

[Bonanno et al. 2003] Bonanno A. et al. "Mean-field dynamo action in protoneutron stars". *A&A* 410.3, (2003), pp. L33–L36. DOI: 10.1051/0004-6361:20031459. URL: https://doi.org/10.1051/0004-6361:20031459.

[Borges et al. 2008] Borges Rafael et al. "An improved weighted essentially non-oscillatory scheme for hyperbolic conservation laws". *Journal of Computational Physics* 227.6, (2008), pp. 3191–3211. ISSN: 0021-9991. DOI: https://doi.org/10.1016/j.jcp.2007.11.038. URL: https://www.sciencedirect.com/science/article/pii/S0021999107005232.

[Brandenburg and Subramanian 2005] Brandenburg Axel and Subramanian Kandaswamy. "Astrophysical magnetic fields and nonlinear dynamo theory". *Physics Reports* 417.1, (2005), pp. 1–209. ISSN: 0370-1573. DOI: https://doi.org/10.1016/j.physrep.2005.06.005. URL: https://www.sciencedirect.com/science/article/pii/S037015730500267X.

[Bucciantini and Del Zanna 2011] Bucciantini N. and Del Zanna L. "General relativistic magnetohydrodynamics in axisymmetric dynamical spacetimes: the X-ECHO code". *A&A* 528, (2011), A101. DOI: 10.1051/0004-6361/201015945. URL: https://doi.org/10.1051/0004-6361/201015945.

[Bucciantini and Del Zanna 2012] Bucciantini N. and Del Zanna L. "A fully covariant mean-field dynamo closure for numerical 3 + 1 resistive GRMHD". *Monthly Notices of the Royal Astronomical Society* 428.1, (2012), pp. 71–85. ISSN: 0035-8711. DOI: 10.1093/mnras/sts005. eprint: https://academic.oup.com/mnras/article-pdf/428/1/71/3626764/71.pdf. URL: https://doi.org/10.1093/mnras/sts005.

[Bugli et al. 2014] Bugli M. et al. "Dynamo action in thick discs around Kerr black holes: high-order resistive GRMHD simulations". *Monthly Notices of the Royal Astronomical Society: Letters* 440.1, (2014), pp. L41–L45. ISSN: 1745-3925. DOI: 10.1093/mnrasl/slu017. eprint: https://academic.oup.com/mnrasl/article-

pdf/440/1/L41/4197947/slu017.pdf. URL: https://doi.org/10.1093/mnrasl/slu017.

[Butcher 1987] Butcher W. *The numerical analysis of Ordinary differential equations. Runge-Kutta and general linear methods*. John Wiley and Sons, 1987.

[Camenzind 2007] Camenzind Max. *Compact Objects in Astrophysics: White Dwarfs, Neutron Stars and Black Holes*. Springer-Verlag Berlin Heidelberg, 2007. DOI: 10.1007/978-3-540-49912-1.

[Carroll and Ostlie 2017] Carroll Bradley W. and Ostlie Dale A. *An Introduction to Modern Astrophysics*. 2nd ed. Cambridge University Press, 2017.

[Cassak and Drake 2013] Cassak P. A. and Drake J. F. "On phase diagrams of magnetic reconnection". *Phys. Plasmas* 20, (2013), p. 061207.

[Cerdá-Durán et al. 2007] Cerdá-Durán Pablo et al. "AMR simulations of the low T/|W| bar-mode instability of neutron stars". *Computer Physics Communications* 177.3, (2007), pp. 288–297. ISSN: 0010-4655. DOI: https://doi.org/10.1016/j.cpc.2007.04.001. URL: https://www.sciencedirect.com/science/article/pii/S0010465507002068.

[Chadwick 1932] Chadwick James. "The existence of a neutron". *The Astrophysical Journal* 136, (1932), pp. 692–708. DOI: 10.1098/rspa.1932.0112.

[Chae and Litvinenko 2021] Chae Jongchul and Litvinenko Yuri E. "Electric resistivity of partially ionized plasma in the lower solar atmosphere". *Res. Astron. Astrophys* 21.9, (2021). DOI: 10.1088/1674-4527/21/9/232.

[Chandrasekhar 1931] Chandrasekhar S. "The Maximum Mass of Ideal White Dwarfs". *The Astrophysical Journal* 74, (1931), p. 81.

[Chandrasekhar 1960] Chandrasekhar S. "The stability of non-dissipative Couette flow in hydromagnetics". *Proceedings of the National Academy of Sciences* 46.2, (1960), pp. 253–257. DOI: 10.1073/pnas.46.2.253. eprint: https://www.pnas.org/doi/pdf/10.1073/pnas.46.2.253. URL: https://www.pnas.org/doi/abs/10.1073/pnas.46.2.253.

[Ciolfi 2020] Ciolfi Riccardo. "Collimated outflows from long-lived binary neutron star merger remnants". *Monthly Notices of the Royal Astronomical Society: Letters* 495.1, (Apr. 2020), pp. L66–L70. ISSN: 1745-3925. DOI: 10.1093/mnrasl/slaa062.

eprint: https://academic.oup.com/mnrasl/article-pdf/495/1/L66/56979155/mnrasl_495_1_l66.pdf. URL: https://doi.org/10.1093/mnrasl/slaa062.

[Ciolfi et al. 2017] Ciolfi Riccardo et al. "General relativistic magnetohydrodynamic simulations of binary neutron star mergers forming a long-lived neutron star". *Phys. Rev. D* 95, (6 2017), p. 063016. DOI: 10.1103/PhysRevD.95.063016. URL: https://link.aps.org/doi/10.1103/PhysRevD.95.063016.

[Ciolfi et al. 2019] Ciolfi Riccardo et al. "First 100 ms of a long-lived magnetized neutron star formed in a binary neutron star merger". *Phys. Rev. D* 100, (2 2019), p. 023005. DOI: 10.1103/PhysRevD.100.023005. URL: https://link.aps.org/doi/10.1103/PhysRevD.100.023005.

[Cipolletta et al. 2020] Cipolletta F. et al. "Spritz: a new fully general-relativistic magnetohydrodynamic code". *Classical and Quantum Gravity* 37.13, (2020), p. 135010. DOI: 10.1088/1361-6382/ab8be8. URL: https://dx.doi.org/10.1088/1361-6382/ab8be8.

[Collinson et al. 2016] Collinson James S. et al. "Reaching the peak of the quasar spectral energy distribution – II. Exploring the accretion disc, dusty torus and host galaxy". *Monthly Notices of the Royal Astronomical Society* 465.1, (2016), pp. 358–382. DOI: 10.1093/mnras/stw2666. eprint: https://academic.oup.com/mnras/article-pdf/465/1/358/8593036/stw2666.pdf. URL: https://doi.org/10.1093/mnras/stw2666.

[Cook et al. 2023] Cook William et al. *GR-Athena++: General-relativistic magnetohydrodynamics simulations of neutron star spacetimes*. 2023. arXiv: 2311.04989 [gr-qc]. URL: https://arxiv.org/abs/2311.04989.

[Cordero-Carrión et al. 2009] Cordero-Carrión Isabel et al. "Improved constrained scheme for the Einstein equations: An approach to the uniqueness issue". *Phys. Rev. D* 79, (2 2009), p. 024017. DOI: 10.1103/PhysRevD.79.024017. URL: https://link.aps.org/doi/10.1103/PhysRevD.79.024017.

[Corvino et al. 2010] Corvino Giovanni et al. "On the Shear Instability in Relativistic Neutron Stars". *Class. Quant. Grav.* 27.11, (2010). Ed. by Ott Christian D. et al., p. 114104. DOI: 10.1088/0264-9381/27/11/114104. arXiv: 1001.5281 [gr-qc].

[Dall'Osso et al. 2009] Dall'Osso S. et al. "Early evolution of newly born magnetars with a strong toroidal field". *Monthly Notices of the Royal Astronomical Society* 398, (2009). DOI: 10.1111/j.1365-2966.2008.14054.x.

[De Pietri et al. 2014] De Pietri Roberto et al. "Neutron Star instabilities in full General Relativity using a $\Gamma = 2.75$ ideal fluid". *Phys. Rev. D* 90.2, (2014), p. 024034. DOI: 10.1103/PhysRevD.90.024034. arXiv: 1403.8066 [gr-qc].

[De Pietri et al. 2020] De Pietri Roberto et al. "Numerical-relativity simulations of long-lived remnants of binary neutron star mergers". *Phys. Rev. D* 101, (6 Mar. 2020), p. 064052. DOI: 10.1103/PhysRevD.101.064052. URL: https://link.aps.org/doi/10.1103/PhysRevD.101.064052.

[Del Zanna and Bucciantini 2002] Del Zanna L. and Bucciantini N. "An efficient shock-capturing central-type scheme for multidimensional relativistic flows. I. Hydrodynamics". *A&A* 390, (2002). DOI: 10.1051/0004-6361:20020776.

[Del Zanna and Bucciantini 2018] Del Zanna L. and Bucciantini N. "Covariant and 3 + 1 equations for dynamo-chiral general relativistic magnetohydrodynamics". *Monthly Notices of the Royal Astronomical Society* 479.1, (2018), pp. 657–666. ISSN: 0035-8711. DOI: 10.1093/mnras/sty1633. eprint: https://academic.oup.com/mnras/article-pdf/479/1/657/25126643/sty1633.pdf. URL: https://doi.org/10.1093/mnras/sty1633.

[Del Zanna et al. 2003] Del Zanna L. et al. "An efficient shock-capturing central-type scheme for multidimensional relativistic flows - II. Magnetohydrodynamics". *A&A* 400.2, (2003), pp. 397–413. DOI: 10.1051/0004-6361:20021641. URL: https://doi.org/10.1051/0004-6361:20021641.

[Del Zanna et al. 2007] Del Zanna L. et al. "ECHO: a Eulerian conservative high-order scheme for general relativistic magnetohydrodynamics and magnetodynamics". *A&A* 473.1, (2007), pp. 11–30. DOI: 10.1051/0004-6361:20077093. URL: https://doi.org/10.1051/0004-6361:20077093.

[Del Zanna et al. 2022] Del Zanna L. et al. "General Relativistic Magnetohydrodynamics Mean-Field Dynamos". *Fluids* 7.2, (2022). ISSN: 2311-5521. DOI: 10.3390/fluids7020087. URL: https://www.mdpi.com/2311-5521/7/2/87.

[Dimmelmeier et al. 2006] Dimmelmeier Harald et al. "Non-linear axisymmetric pulsations of rotating relativistic stars in the conformal flatness approximation". *Monthly Notices of the Royal Astronomical Society* 368.4, (Apr. 2006), pp. 1609–1630. ISSN: 0035-8711. DOI: 10.1111/j.1365-2966.2006.10274.x. eprint: https://academic.oup.com/mnras/article-pdf/368/4/1609/3964395/mnras0368-1609.pdf. URL: https://doi.org/10.1111/j.1365-2966.2006.10274.x.

[Dionysopoulou et al. 2013] Dionysopoulou Kyriaki et al. "General-relativistic resistive magnetohydrodynamics in three dimensions: Formulation and tests". *Phys. Rev. D* 88, (4 2013), p. 044020. DOI: 10.1103/PhysRevD.88.044020. URL: https://link.aps.org/doi/10.1103/PhysRevD.88.044020.

[Dionysopoulou et al. 2015] Dionysopoulou Kyriaki et al. "General-relativistic resistive-magnetohydrodynamic simulations of binary neutron stars". *Phys. Rev. D* 92, (8 2015), p. 084064. DOI: 10.1103/PhysRevD.92.084064. URL: https://link.aps.org/doi/10.1103/PhysRevD.92.084064.

[Douchin and Haensel 2001] Douchin F. and Haensel P. "A unified equation of state of dense matter and neutron star structure". *A&A* 380.1, (2001), pp. 151–167. DOI: 10.1051/0004-6361:20011402. URL: https://doi.org/10.1051/0004-6361:20011402.

[Drenkhahn and Spruit 2002] Drenkhahn G. and Spruit H. C. "Efficient acceleration and radiation in Poynting flux powered GRB outflows". *A&A* 391.3, (2002), pp. 1141–1153. DOI: 10.1051/0004-6361:20020839. URL: https://doi.org/10.1051/0004-6361:20020839.

[Duez et al. 2005] Duez Matthew D. et al. "Relativistic magnetohydrodynamics in dynamical spacetimes: Numerical methods and tests". *Phys. Rev. D* 72, (2 2005), p. 024028. DOI: 10.1103/PhysRevD.72.024028. URL: https://link.aps.org/doi/10.1103/PhysRevD.72.024028.

[Dumbser and Zanotti 2009] Dumbser Michael and Zanotti Olindo. "Very high order PNPM schemes on unstructured meshes for the resistive relativistic MHD equations". *Journal of Computational Physics* 228.18, (2009), pp. 6991–7006. ISSN: 0021-9991. DOI: https://doi.org/10.1016/j.jcp.2009.06.009. URL: https://www.sciencedirect.com/science/article/pii/S0021999109003350.

[Eckart 1940] Eckart Carl. "The Thermodynamics of Irreversible Processes. III. Relativistic Theory of the Simple Fluid". *Phys. Rev.* 58, (10 1940), pp. 919–924. DOI: 10.1103/PhysRev.58.919. URL: https://link.aps.org/doi/10.1103/PhysRev.58.919.

[Endrizzi et al. 2016] Endrizzi A. et al. "General relativistic magnetohydrodynamic simulations of binary neutron star mergers with the APR4 equation of state". *Classical and Quantum Gravity* 33.16, (2016), p. 164001. DOI: 10.1088/0264-9381/33/16/164001. URL: https://dx.doi.org/10.1088/0264-9381/33/16/164001.

[Etienne et al. 2012] Etienne Z. B. et al. "General relativistic simulations of black-hole–neutron-star mergers: Effects of magnetic fields". *Phys. Rev. D* 85, (6 2012), p. 064029. DOI: 10.1103/PhysRevD.85.064029. URL: https://link.aps.org/doi/10.1103/PhysRevD.85.064029.

[Etienne et al. 2015] Etienne Z. B. et al. "IllinoisGRMHD: an open-source, user-friendly GRMHD code for dynamical spacetimes". *Classical and Quantum Gravity* 32.17, (2015), p. 175009. DOI: 10.1088/0264-9381/32/17/175009. URL: https://dx.doi.org/10.1088/0264-9381/32/17/175009.

[Font et al. 2000] Font José A. et al. "Non-linear hydrodynamical evolution of rotating relativistic stars: numerical methods and code tests". *Monthly Notices of the Royal Astronomical Society* 313.4, (2000), pp. 678–688. ISSN: 0035-8711. DOI: 10.1046/j.1365-8711.2000.03254.x. eprint: https://academic.oup.com/mnras/article-pdf/313/4/678/3788071/313-4-678.pdf. URL: https://doi.org/10.1046/j.1365-8711.2000.03254.x.

[Franceschetti and Del Zanna 2020] Franceschetti K. and Del Zanna L. "General Relativistic Mean-Field Dynamo Model for Proto-Neutron Stars". *Universe* 6.6, (2020), p. 83. ISSN: 2218-1997. DOI: 10.3390/universe6060083.

[Franceschetti and De Pietri 2024a] Franceschetti Kevin and De Pietri Roberto. *MIR: a general-relativistic resistive-magneto-hydrodynamic code to study the effect of resistivity in Neutron Star dynamics*. in preparation. 2024.

[Franceschetti and De Pietri 2024b] Franceschetti Kevin and De Pietri Roberto. *The MIR code*. Version 1.0.0. 2024. DOI: 10.5281/zenodo.13986384. URL: https://doi.org/10.5281/zenodo.13986384.

[Franci et al. 2013] Franci Luca et al. "Dynamical bar-mode instability in rotating and magnetized relativistic stars". *Phys. Rev. D* 88, (10 2013), p. 104028. DOI: 10.1103/PhysRevD.88.104028. URL: https://link.aps.org/doi/10.1103/PhysRevD.88.104028.

[Frank et al. 2002] Frank Juhan et al. *Accretion Power in Astrophysics*. 3rd ed. Cambridge University Press, 2002.

[Friedman and Stergioulas 2013] Friedman John L. and Stergioulas Nikolaos. *Rotating Relativistic Stars*. Cambridge Monographs on Mathematical Physics. Cambridge University Press, 2013.

[Galeazzi et al. 2013] Galeazzi Filippo et al. "Implementation of a simplified approach to radiative transfer in general relativity". *Phys. Rev. D* 88, (6 2013), p. 064009. DOI: 10.1103/PhysRevD.88.064009. URL: https://link.aps.org/doi/10.1103/PhysRevD.88.064009.

[Gammie et al. 2003] Gammie Charles F. et al. "HARM: A Numerical Scheme for General Relativistic Magnetohydrodynamics". *The Astrophysical Journal* 589.1, (2003), p. 444. DOI: 10.1086/374594. URL: https://dx.doi.org/10.1086/374594.

[Ghosh 2007] Ghosh P. *Rotation and Accretion Powered Pulsars*. World Scientific, 2007. DOI: 10.1142/4806.

[Giacomazzo et al. 2011a] Giacomazzo Bruno et al. "Accurate evolutions of inspiralling and magnetized neutron stars: Equal-mass binaries". *Phys. Rev. D* 83, (4 Feb. 2011), p. 044014. DOI: 10.1103/PhysRevD.83.044014. URL: https://link.aps.org/doi/10.1103/PhysRevD.83.044014.

[Giacomazzo et al. 2011b] Giacomazzo Bruno et al. "Collapse of differentially rotating neutron stars and cosmic censorship". *Phys. Rev. D* 84, (2 2011), p. 024022. DOI: 10.1103/PhysRevD.84.024022. URL: https://link.aps.org/doi/10.1103/PhysRevD.84.024022.

[Ginzburg and Kirzhnits 1964] Ginzburg VL and Kirzhnits DA. "On the superfluidity of neutron stars". *Zh. Eksperim. i Teor. Fiz.* 47, (1964).

[Glendenning 1997] Glendenning Norman K. *Compact Stars: Nuclear Physics, Particle Physics and General Relativity*. Springer-Verlag Berlin Heidelberg, 1997. DOI: 10.1007/978-1-4684-0491-3.

[Gourgoulhon 2012] Gourgoulhon Eric. *3+1 Formalism in General Relativity*. Springer-Verlag Berlin Heidelberg, 2012. URL: http://www.springer.com/us/book/9783642245244.

[Harten 1983] Harten Ami. "High resolution schemes for hyperbolic conservation laws". *Journal of Computational Physics* 49.3, (1983), pp. 357–393. ISSN: 0021-9991. DOI: https://doi.org/10.1016/0021-9991(83)90136-5. URL: https://www.sciencedirect.com/science/article/pii/0021999183901365.

[Harten et al. 1983] Harten Amiram et al. "On Upstream Differencing and Godunov-Type Schemes for Hyperbolic Conservation Laws". *SIAM Review* 25.1, (1983), pp. 35–

61. ISSN: 00361445. URL: http://www.jstor.org/stable/2030019 (visited on 10/03/2023).

[Heisenberg and Euler 1936] Heisenberg W. and Euler H. "Folgerungen aus der Diracschen Theorie des Positrons". *Z. Phys.* 98, (1936), p. 714.

[Holberg 2009] Holberg J. B. "The Maximum Mass of Ideal White Dwarfs". *J. Phys.: Conf. Ser.* 172, (2009), p. 012022. DOI: 10.1088/1742-6596/172/1/012022.

[Iosif and Stergioulas 2021] Iosif Panagiotis and Stergioulas Nikolaos. "Equilibrium sequences of differentially rotating stars with post-merger-like rotational profiles". *Monthly Notices of the Royal Astronomical Society* 503.1, (2021), pp. 850–866. DOI: 10.1093/mnras/stab392. eprint: https://academic.oup.com/mnras/article-pdf/503/1/850/36616616/stab392.pdf. URL: https://doi.org/10.1093/mnras/stab392.

[Kalinani et al. 2024] Kalinani Jay V. et al. *AsterX: a new open-source GPU-accelerated GRMHD code for dynamical spacetimes*. 2024. arXiv: 2406.11669 [astro-ph.HE]. URL: https://arxiv.org/abs/2406.11669.

[Kastaun et al. 2021] Kastaun Wolfgang et al. "Robust recovery of primitive variables in relativistic ideal magnetohydrodynamics". *Phys. Rev. D* 103, (2 2021), p. 023018. DOI: 10.1103/PhysRevD.103.023018. URL: https://link.aps.org/doi/10.1103/PhysRevD.103.023018.

[Kiuchi et al. 2015] Kiuchi Kenta et al. "Efficient magnetic-field amplification due to the Kelvin-Helmholtz instability in binary neutron star mergers". *Phys. Rev. D* 92, (12 2015), p. 124034. DOI: 10.1103/PhysRevD.92.124034. URL: https://link.aps.org/doi/10.1103/PhysRevD.92.124034.

[Kiuchi et al. 2022] Kiuchi Kenta et al. "Implementation of advanced Riemann solvers in a neutrino-radiation magnetohydrodynamics code in numerical relativity and its application to a binary neutron star merger". *Phys. Rev. D* 106, (12 2022), p. 124041. DOI: 10.1103/PhysRevD.106.124041. URL: https://link.aps.org/doi/10.1103/PhysRevD.106.124041.

[Komatsu et al. 1989] Komatsu Hidemi et al. "Rapidly rotating general relativistic stars – I. Numerical method and its application to uniformly rotating polytropes". *Monthly Notices of the Royal Astronomical Society* 237.2, (1989), pp. 355–379. ISSN: 0035-8711. DOI: 10.1093/mnras/237.2.355. eprint: https://academic.oup.com/

mnras/article-pdf/237/2/355/2983266/mnras237-0355.pdf. URL: https://doi.org/10.1093/mnras/237.2.355.

[Komissarov 2007] Komissarov Serguei S. "Multidimensional numerical scheme for resistive relativistic magnetohydrodynamics". *Monthly Notices of the Royal Astronomical Society* 382.3, (2007), pp. 995–1004. DOI: 10.1111/j.1365-2966.2007.12448.x.

[Kreiss and Oliger 1973] Kreiss H. and Oliger J. *Methods for the approximate solution of time dependent problems*. GARP publications series, no. 10, 1973.

[Landau and Lifshitz 1987] Landau L. D. and Lifshitz E. M. *Fluid Mechanics*. 2nd Ed. Pergamon Press, 1987.

[Lazarian and Vishniac 1999] Lazarian A. and Vishniac Ethan T. "Reconnection in a Weakly Stochastic Field". *The Astrophysical Journal* 517.2, (1999), p. 700. DOI: 10.1086/307233. URL: https://dx.doi.org/10.1086/307233.

[Lipunov 1992] Lipunov V. M. *Astrophysics of Neutron Stars*. Springer-Verlag Berlin Heidelberg, 1992.

[Löffler et al. 2012] Löffler Frank et al. "The Einstein Toolkit: a community computational infrastructure for relativistic astrophysics". *Classical and Quantum Gravity* 29.11, (2012), p. 115001. DOI: 10.1088/0264-9381/29/11/115001. URL: https://dx.doi.org/10.1088/0264-9381/29/11/115001.

[Löffler et al. 2015] Löffler Frank et al. "Stiffness effects on the dynamics of the bar-mode instability of Neutron Stars in full General Relativity". *Phys. Rev. D* 91, (2015), p. 064057. DOI: 10.1103/PhysRevD.91.064057. arXiv: 1411.1963 [gr-qc].

[Londrillo and Del Zanna 2000] Londrillo P. and Del Zanna L. "High-Order Upwind Schemes for Multidimensional Magnetohydrodynamics". *The Astrophysical Journal* 530.1, (2000), p. 508. DOI: 10.1086/308344. URL: https://dx.doi.org/10.1086/308344.

[Lorimer and Kramer 2005] Lorimer Duncan Ross and Kramer Michael. *Handbook of pulsar astronomy*. Vol. 4. Cambridge university press, 2005.

[Maggiore 2007] Maggiore Michele. *Gravitational Waves: Volume 1: Theory and Experiments*. Oxford University Press, 2007. ISBN: 9780198570745. DOI: 10.1093/

acprof:oso/9780198570745.001.0001. URL: https://doi.org/10.1093/acprof:oso/9780198570745.001.0001.

[Maggiore 2018] Maggiore Michele. *Gravitational Waves: Volume 2: Astrophysics and Cosmology*. Oxford University Press, 2018. ISBN: 9780198570899. DOI: 10.1093/oso/9780198570899.001.0001. URL: https://doi.org/10.1093/oso/9780198570899.001.0001.

[Maldacena 1998] Maldacena Juan. "The large N limit of superconformal field theories and supergravity". *Advances in Theoretical and Mathematical Physics* 2.2, (1998), pp. 231–252. DOI: 10.4310/ATMP.1998.v2.n2.a1.

[Mallick and Schramm 2014] Mallick Ritam and Schramm Stefan. "Deformation of a magnetized neutron star". *Phys. Rev. C* 89, (4 2014), p. 045805. DOI: 10.1103/PhysRevC.89.045805. URL: https://link.aps.org/doi/10.1103/PhysRevC.89.045805.

[Manca et al. 2007] Manca Gian Mario et al. "Dynamical non-axisymmetric instabilities in rotating relativistic stars". *Class. Quant. Grav.* 24, (2007). Ed. by Campanelli Manuela and Rezzolla Luciano, S171–S186. DOI: 10.1088/0264-9381/24/12/S12. arXiv: 0705.1826 [astro-ph].

[Margalit and Metzger 2017] Margalit B. and Metzger B.D. "Constraining the Maximum Mass of Neutron Stars from Multi-messenger Observations of GW170817". *ApJL* 850, (2017), p. L19. DOI: 10.3847/2041-8213/aa991c.

[Mastrano et al. 2013] Mastrano A. et al. "Neutron star deformation due to multipolar magnetic fields". *Monthly Notices of the Royal Astronomical Society* 434.2, (2013), pp. 1658–1667. DOI: 10.1093/mnras/stt1131. eprint: https://academic.oup.com/mnras/article-pdf/434/2/1658/18498797/stt1131.pdf. URL: https://doi.org/10.1093/mnras/stt1131.

[Mastrano et al. 2015] Mastrano A. et al. "Neutron star deformation due to poloidal–toroidal magnetic fields of arbitrary multipole order: a new analytic approach". *Monthly Notices of the Royal Astronomical Society* 447.4, (2015), pp. 3475–3485. ISSN: 0035-8711. DOI: 10.1093/mnras/stu2671. eprint: https://academic.oup.com/mnras/article-pdf/447/4/3475/5701660/stu2671.pdf. URL: https://doi.org/10.1093/mnras/stu2671.

[Mattia et al. 2023] Mattia G. et al. "Resistive relativistic MHD simulations of astrophysical jets". *A&A* 679, (2023), A49. DOI: 10.1051/0004-6361/202347126. URL: https://doi.org/10.1051/0004-6361/202347126.

[Meissner and Ochsenfeld 1933] Meissner W. and Ochsenfeld R. "Ein neuer Effekt bei Eintritt der Supraleitf". *Naturwissenschaften* 21, (1933), pp. 787–788. DOI: 10.1007/BF01504252.

[Meszaros 1992] Meszaros P. *High-energy radiation from magnetized neutron stars*. The Chicago Univerity Press, 1992.

[Migdal 1959] Migdal A.B. "Superfluidity and the moments of inertia of nuclei". *Nuclear Physics* 13.5, (1959), pp. 655–674. DOI: https://doi.org/10.1016/0029-5582(59)90264-0. URL: https://www.sciencedirect.com/science/article/pii/0029558259902640.

[Mignani et al. 2016] Mignani R. P. et al. "Evidence for vacuum birefringence from the first optical-polarimetry measurement of the isolated neutron star RX J1856.53754". *Monthly Notices of the Royal Astronomical Society* 465.1, (2016), pp. 492–500. DOI: 10.1093/mnras/stw2798. eprint: https://academic.oup.com/mnras/article-pdf/465/1/492/8593962/stw2798.pdf. URL: https://doi.org/10.1093/mnras/stw2798.

[Mignone and McKinney 2007] Mignone A. and McKinney Jonathan C. "Equation of state in relativistic magnetohydrodynamics: variable versus constant adiabatic index". *Monthly Notices of the Royal Astronomical Society* 378.3, (2007), pp. 1118–1130. ISSN: 0035-8711. DOI: 10.1111/j.1365-2966.2007.11849.x. eprint: https://academic.oup.com/mnras/article-pdf/378/3/1118/18672055/mnras0378-1118.pdf. URL: https://doi.org/10.1111/j.1365-2966.2007.11849.x.

[Moffatt 1983] Moffatt H. K. *Magnetic field generation in electrically conducting fluids*. Cambridge University Press, 1983.

[Mösta et al. 2013] Mösta Philipp et al. "GRHydro: a new open-source general-relativistic magnetohydrodynamics code for the Einstein toolkit". *Classical and Quantum Gravity* 31.1, (2013), p. 015005. DOI: 10.1088/0264-9381/31/1/015005. URL: https://dx.doi.org/10.1088/0264-9381/31/1/015005.

[NASA 2019] NASA. *Stellar Evolution: A Journey with Chandra*. Poster, available online. Accessed: 2024-10-01. Produced at the Smithsonian Astrophysical Observa-

tory (SAO) under contract NAS8-03060. 2019. URL: https://chandra.harvard.edu/edu/formal/stellar_ev/.

[Naso et al. 2008] Naso L. et al. "Magnetic field amplification in proto-neutron stars - The role of the neutron-finger instability for dynamo excitation". *A&A* 479.1, (2008), pp. 167–176. DOI: 10.1051/0004-6361:20078360. URL: https://doi.org/10.1051/0004-6361:20078360.

[Obergaulinger et al. 2010] Obergaulinger M. et al. "Local simulations of the magnetized Kelvin-Helmholtz instability in neutron-star mergers". *A&A* 515, (2010), A30. DOI: 10.1051/0004-6361/200913386. URL: https://doi.org/10.1051/0004-6361/200913386.

[Palenzuela et al. 2009] Palenzuela Carlos et al. "Beyond ideal MHD: towards a more realistic modelling of relativistic astrophysical plasmas". *Monthly Notices of the Royal Astronomical Society* 394.4, (2009), pp. 1727–1740. ISSN: 0035-8711. DOI: 10.1111/j.1365-2966.2009.14454.x. eprint: https://academic.oup.com/mnras/article-pdf/394/4/1727/4031080/mnras0394-1727.pdf. URL: https://doi.org/10.1111/j.1365-2966.2009.14454.x.

[Pareschi and Russo 2005] Pareschi L. and Russo G. "Implicit–Explicit Runge–Kutta Schemes and Applications to Hyperbolic Systems with Relaxation". *Journal of Scientific Computing* 25, (2005), pp. 129–155. DOI: 10.1007/s10915-004-4636-4.

[Paschalidis and Shapiro 2013] Paschalidis Vasileios and Shapiro Stuart L. "A new scheme for matching general relativistic ideal magnetohydrodynamics to its force-free limit". *Phys. Rev. D* 88, (10 2013), p. 104031. DOI: 10.1103/PhysRevD.88.104031. URL: https://link.aps.org/doi/10.1103/PhysRevD.88.104031.

[Passamonti and Andersson 2020] Passamonti A. and Andersson N. "Merger-inspired rotation laws and the low-T/W instability in neutron stars". *Monthly Notices of the Royal Astronomical Society* 498.4, (2020), pp. 5904–5915. DOI: 10.1093/mnras/staa2725. eprint: https://academic.oup.com/mnras/article-pdf/498/4/5904/33838626/staa2725.pdf. URL: https://doi.org/10.1093/mnras/staa2725.

[Pili et al. 2014] Pili A. G. et al. "Axisymmetric equilibrium models for magnetized neutron stars in General Relativity under the Conformally Flat Condition". *Monthly Notices of the Royal Astronomical Society* 439.4, (2014), pp. 3541–3563. ISSN: 0035-8711. DOI: 10.1093/mnras/stu215. eprint: https://academic.oup.com/mnras/

article-pdf/439/4/3541/3981452/stu215.pdf. URL: https://doi.org/10.1093/mnras/stu215.

[Press et al. 2007] Press William H. et al. *Numerical Recipes 3rd Edition: The Art of Scientific Computing*. 3rd ed. Cambridge University Press, 2007. ISBN: 0521880688.

[Prix 2009] Prix Reinhard. "Gravitational Waves from Spinning Neutron Stars". In: *Neutron Stars and Pulsars*. Ed. by Becker Werner. Berlin, Heidelberg: Springer Berlin Heidelberg, 2009, pp. 651–685. ISBN: 978-3-540-76965-1. DOI: 10.1007/978-3-540-76965-1_24. URL: https://doi.org/10.1007/978-3-540-76965-1_24.

[Read et al. 2009] Read Jocelyn S. et al. "Constraints on a phenomenologically parametrized neutron-star equation of state". *Phys. Rev. D* 79, (12 2009), p. 124032. DOI: 10.1103/PhysRevD.79.124032. URL: https://link.aps.org/doi/10.1103/PhysRevD.79.124032.

[Reboul-Salze et al. 2021] Reboul-Salze A. et al. "A global model of the magnetorotational instability in protoneutron stars". *A&A* 645, (2021), A109. DOI: 10.1051/0004-6361/202038369. URL: https://doi.org/10.1051/0004-6361/202038369.

[Rezzolla and Zanotti 2013] Rezzolla L. and Zanotti O. *Relativistic Hydrodynamics*. Oxford University Press, 2013. DOI: 10.1093/acprof:oso/9780198528906.001.0001. URL: https://doi.org/10.1093/acprof:oso/9780198528906.001.0001.

[Rezzolla et al. 2011] Rezzolla Luciano et al. "THE MISSING LINK: MERGING NEUTRON STARS NATURALLY PRODUCE JET-LIKE STRUCTURES AND CAN POWER SHORT GAMMA-RAY BURSTS". *The Astrophysical Journal Letters* 732.1, (2011), p. L6. DOI: 10.1088/2041-8205/732/1/L6. URL: https://dx.doi.org/10.1088/2041-8205/732/1/L6.

[Saijo et al. 2001] Saijo Motoyuki et al. "Dynamical Bar Instability in Rotating Stars: Effect of General Relativity". *The Astrophysical Journal* 548.2, (Feb. 2001), p. 919. DOI: 10.1086/319016. URL: https://dx.doi.org/10.1086/319016.

[Shankar et al. 2023] Shankar Swapnil et al. "GRaM-X: a new GPU-accelerated dynamical spacetime GRMHD code for Exascale computing with the Einstein Toolkit". *Classical and Quantum Gravity* 40.20, (Sept. 2023), p. 205009. DOI: 10.1088/1361-6382/acf2d9. URL: https://dx.doi.org/10.1088/1361-6382/acf2d9.

[Shapiro and Teukolsky 1983] Shapiro S. L. and Teukolsky S. A. *Black holes, white dwarfs, and neutron stars: The physics of compact objects*. Wiley-VCH, 1983. DOI: 10.1002/9783527617661.

[Shibata and Sekiguchi 2005] Shibata Masaru and Sekiguchi Yu-ichirou. "Magnetohydrodynamics in full general relativity: Formulation and tests". *Phys. Rev. D* 72, (4 2005), p. 044014. DOI: 10.1103/PhysRevD.72.044014. URL: https://link.aps.org/doi/10.1103/PhysRevD.72.044014.

[Shibata et al. 2000] Shibata Masaru et al. "The Bar-Mode Instability in Differentially Rotating Neutron Stars: Simulations in Full General Relativity". *The Astrophysical Journal* 542.1, (2000), p. 453. DOI: 10.1086/309525. URL: https://dx.doi.org/10.1086/309525.

[Shibata et al. 2021] Shibata Masaru et al. "Long-term evolution of neutron-star merger remnants in general relativistic resistive magnetohydrodynamics with a mean-field dynamo term". *Phys. Rev. D* 104, (6 2021), p. 063026. DOI: 10.1103/PhysRevD.104.063026. URL: https://link.aps.org/doi/10.1103/PhysRevD.104.063026.

[Stergioulas et al. 2004] Stergioulas Nikolaos et al. "Non-linear pulsations in differentially rotating neutron stars: mass-shedding-induced damping and splitting of the fundamental mode". *Monthly Notices of the Royal Astronomical Society* 352.4, (Aug. 2004), pp. 1089–1101. ISSN: 0035-8711. DOI: 10.1111/j.1365-2966.2004.07973.x. eprint: https://academic.oup.com/mnras/article-pdf/352/4/1089/18652469/352-4-1089.pdf. URL: https://doi.org/10.1111/j.1365-2966.2004.07973.x.

[Sur et al. 2022] Sur Ankan et al. "Long-term general relativistic magnetohydrodynamics simulations of magnetic field in isolated neutron stars". *Monthly Notices of the Royal Astronomical Society* 511.3, (Feb. 2022), pp. 3983–3993. ISSN: 0035-8711. DOI: 10.1093/mnras/stac353. eprint: https://academic.oup.com/mnras/article-pdf/511/3/3983/42579025/stac353.pdf. URL: https://doi.org/10.1093/mnras/stac353.

[Taub 1948] Taub A. H. "Relativistic Rankine-Hugoniot Equations". *Phys. Rev.* 74, (3 1948), pp. 328–334. DOI: 10.1103/PhysRev.74.328. URL: https://link.aps.org/doi/10.1103/PhysRev.74.328.

[Thompson and Duncan 1995] Thompson Christopher and Duncan Robert C. "The soft gamma repeaters as very strongly magnetized neutron stars - I. Radiative mechanism for outbursts". *Monthly Notices of the Royal Astronomical Society* 275.2, (1995), pp. 255–300. ISSN: 0035-8711. DOI: 10.1093/mnras/275.2.255. eprint:

https://academic.oup.com/mnras/article-pdf/275/2/255/18539652/mnras275-0255.pdf. URL: https://doi.org/10.1093/mnras/275.2.255.

[Tomei et al. 2019] Tomei N. et al. "General relativistic magnetohydrodynamic dynamo in thick accretion discs: fully non-linear simulations". *Monthly Notices of the Royal Astronomical Society* 491.2, (2019), pp. 2346–2359. ISSN: 0035-8711. DOI: 10.1093/mnras/stz3146. eprint: https://academic.oup.com/mnras/article-pdf/491/2/2346/31194788/stz3146.pdf. URL: https://doi.org/10.1093/mnras/stz3146.

[Toonen et al. 2017] Toonen S. et al. "The binarity of the local white dwarf population". *A&A* 602, (2017), A16. DOI: 10.1051/0004-6361/201629978. URL: https://doi.org/10.1051/0004-6361/201629978.

[Toro 2009] Toro E. F. *Riemann Solvers and Numerical Methods for Fluid Dynamics: A Practical Introduction*. Springer Berlin, Heidelberg, 2009.

[Tremblay et al. 2019] Tremblay PE. et al. "Core crystallization and pil-up in the cooling sequence of evolving white dwarfs". *Nature* 565, (2019), pp. 202–205. DOI: 10.1038/s41586-018-0791-x.

[Typel et al. 2015] Typel S. et al. "CompOSE CompStar online supernova equations of state harmonising the concert of nuclear physics and astrophysics compose.obspm.fr". *Phys. Part. Nuclei* 46, (2015), pp. 633–664. DOI: https://doi.org/10.1134/S1063779615040061.

[Velikhov 1959] Velikhov Evgeny Pavlovich. "Stability of an Ideally Conducting Liquid Flowing between Cylinders Rotating in a Magnetic Field". *Soviet Journal of Experimental and Theoretical Physics* 9.5, (1959), pp. 995–998.

[Weber et al. 2009] Weber Fridolin et al. "Neutron Star Interiors and the Equation of State of Superdense Matter". In: *Neutron Stars and Pulsars*. Ed. by Becker Werner. Berlin, Heidelberg: Springer Berlin Heidelberg, 2009, pp. 213–245. ISBN: 978-3-540-76965-1. DOI: 10.1007/978-3-540-76965-1_0. URL: https://doi.org/10.1007/978-3-540-76965-1_0.

[Woltjer 1964] Woltjer L. "X-Rays and Type I Supernova Remnants." *ApJ* 140, (1964), pp. 1309–1313. DOI: 10.1086/148028.

[Zanotti and Dumbser 2011] Zanotti O. and Dumbser M. "Numerical simulations of high Lundquist number relativistic magnetic reconnection". *Monthly Notices of*

the Royal Astronomical Society 418.2, (2011), pp. 1004–1011. ISSN: 0035-8711. DOI: 10.1111/j.1365-2966.2011.19551.x. eprint: https://academic.oup.com/mnras/article-pdf/418/2/1004/3696835/mnras0418-1004.pdf. URL: https://doi.org/10.1111/j.1365-2966.2011.19551.x.

[Zhang and Yan 2011] Zhang Bing and Yan Huirong. "The internal-collision-induced magnetic reconnection and turbulence (ICMART) model of gamma-ray bursts". *The Astrophysical Journal* 726.2, (2011), p. 90. DOI: 10.1088/0004-637X/726/2/90. URL: https://dx.doi.org/10.1088/0004-637X/726/2/90.